Trends in Mathematics
Research Perspectives CRM Barcelona Vol. 2

Álvaro Corral · Anna Deluca
Francesc Font-Clos · Pilar Guerrero
Andrei Korobeinikov
Francesco Massucci Editors

Extended Abstracts Spring 2013

Complex Systems
Control of Infectious Diseases

CRM CENTRE DE RECERCA MATEMÀTICA

Birkhäuser

Trends in Mathematics

Research Perspectives CRM Barcelona

Series Editors

Enric Ventura
Antoni Guillamon

Since 1984 the Centre de Recerca Matemàtica (CRM) has been organizing scientific events such as conferences or workshops which span a wide range of cutting-edge topics in mathematics and present outstanding new results. In the fall of 2012, the CRM decided to publish extended conference abstracts originating from scientific events hosted at the center. The aim of this initiative is to quickly communicate new achievements, contribute to a fluent update of the state of the art, and enhance the scientific benefit of the CRM meetings. The extended abstracts are published in the subseries Research Perspectives CRM Barcelona within the Trends in Mathematics series. Volumes in the subseries will include a collection of revised written versions of the communications, grouped by events.

More information about this series at
http://www.springer.com/series/4961

Extended Abstracts Spring 2013

Complex Systems

Álvaro Corral
Anna Deluca
Francesc Font-Clos
Pilar Guerrero
Francesco Massucci
Editors

Control of Infectious Diseases

Andrei Korobeinikov
Editor

Birkhäuser

Editors
Álvaro Corral
Centre de Recerca Matemàtica
Barcelona
Catalonia
Spain

Anna Deluca
MPI Physics of Complex Systems
Dresden
Germany

Francesc Font-Clos
Centre de Recerca Matemàtica
Barcelona
Catalonia
Spain

Pilar Guerrero
Department of Mathematics
University College London
London
United Kingdom

Andrei Korobeinikov
Centre de Recerca Matemàtica
Barcelona
Catalonia
Spain

Francesco Massucci
Departament d'Enginyeria Química
Universitat Rovira i Virgili
Tarragona
Catalonia
Spain

ISBN 978-3-319-08137-3 ISBN 978-3-319-08138-0 (eBook)
DOI 10.1007/978-3-319-08138-0
Springer Cham Heidelberg New York Dordrecht London

Library of Congress Control Number: 2014952790

2010 Mathematics Subject Classification: 37Fxx, 92Dxx

Printed on acid-free paper

Springer is part of Springer Science+Business Media (www.birkhauser-science.com)

Contents

Part I
Joint CRM-Imperial College Workshop in Complex Systems

Editors

Álvaro Corral
Anna Deluca
Francesc Font-Clos
Pilar Guerrero
Francesco A. Massucci

Preface

In April 2013, during six intensive days, the Centre de Recerca Matemàtica hosted the organization of the *Joint CRM-Imperial College School and Workshop in Complex Systems*, which involved more than 100 participants from all over the world, coming from disciplines as diverse as biology, computer science, or social science (in addition, of course, to physics and mathematics).

Kim Christensen, Henrik Jensen, and Gunnar Pruessner, all three from Imperial College, London, presented highly motivating lectures on percolation theory, dynamics of complex systems, and stochastic processes. Marián Boguñá and Mariángeles Serrano, both from the University of Barcelona, talked enthusiastically about the structure of complex networks, and Antonio Turiel, from the Consejo Superior de Investigaciones Científicas, gave deep coverage of multifractals and their applications. Stefan Thurner, from the Medical University of Vienna, was the keynote speaker of an evening session addressed to the general public, which took place at the Institut d'Estudis Catalans, dealing with subtle extensions of the concept of entropy for non-equilibrium systems.

After the school, a workshop allowed not only participants of the school but also external attendants to present their research topics. We had more than 30 talks and lectures, including topics such as non-linear dynamics, chemical reactions, metabolic networks, climatology, economics, linguistics, statistics of music, cancer

evolution, game theory, earthquakes, neuroscience, Bayesian inference, etc. It is a sample from these communications what constitutes our contribution to the present volume of the subseries Research Perspectives CRM Barcelona, included in Birkhäuser's series Trends in Mathematics. These seventeen Extended Abstracts present, in an agile way, some new results not yet available through the standard publication channels.

The atmosphere of the school and the workshop was very pleasant, and the participants enjoyed not only the lectures but also the discussions during the coffee breaks and lunches (food itself was a subject of debate), as well as the social activities. A consensus emerged that the event should be repeated in the next future, and the organizers will do their best to make that possible. That could be an occasion to improve upon some mistakes that participants generously forgave in this first edition.

No doubt that without the altruistic participation of the lecturers no school would have been possible. A key role was played by the co-organizer Tomás Alarcón. The CRM administration, where Nuria Hernández found herself over-saturated by the success of applications in the last days before the beginning of the school, gave also an important support. Finally, we appreciate the encouragement of Joaquim Bruna as well as the financial contribution from AGAUR.

Barcelona, Catalonia, Spain — Álvaro Corral
Dresden, Germany — Anna Deluca
Barcelona, Catalonia, Spain — Francesc Font-Clos
London, UK — Pilar Guerrero
Tarragona, Catalonia, Spain — Francesco A. Massucci

Mesoscopic Models for the Overstretching Transition of DNA

Ana Elisa Bergues Pupo, Alessandro Fiasconaro, and Fernando Falo

1 Introduction

One of the most intriguing and only partially clear phenomenon concerning the mechanical properties of DNA is the so-called overstretching transition [2, 7]. It consists in a sudden elongation of the DNA chain of about 70 % more than the native length (B-DNA), when a force around 70 pN is applied. Three main mechanisms have been proposed to explain this transition. Two of them involve breaking of the bonds that hold the two strands together: peeling from nicks or free ends of the chain; and inside-strand separation (M-DNA) [10–12]. In the third mechanism, the base pairs remain bonded (S-DNA), and the overstretching appears from a cooperative chain unwinding [2, 3, 6–8]. In this work we present two mesoscopic descriptions of the DNA overstretching transition. The first one, is a model based in a discrete version of a worm-like chain (WLC) model with a modification of the elastic interaction. This model does not enter into the microscopic details of

A.E.B. Pupo (✉)
Departamento de Física de la Materia Condensada, Universidad de Zaragoza, Zaragoza, Spain

Departamento de Física, Universidad de Oriente, Santiago de Cuba, Cuba
e-mail: berguesana@yahoo.es

A. Fiasconaro
Departamento de Física de la Materia Condensada, Universidad de Zaragoza, Zaragoza, Spain

Instituto de Ciencia de Materiales de Aragón, CSIC, Zaragoza, Spain
e-mail: afiascon@unizar.es

F. Falo
Departamento de Física de la Materia Condensada, Universidad de Zaragoza, Zaragoza, Spain

Instituto de Biocomputación y Física de Sistemas Complejos (BIFI), Universidad de Zaragoza, Zaragoza, Spain
e-mail: fff@unizar.es

Á. Corral et al. (eds.), *Extended Abstracts Spring 2013*, Trends in Mathematics 2,
DOI 10.1007/978-3-319-08138-0_1

the mechanisms responsible of the transition (Model 1). In the second one, we extend the above approach to describe the mechanism of force induced melting in the framework of the Peyrard–Bishop–Dauxois (PBD) model [4] (Model 2).

2 Model and Methods

2.1 Model 1: Double Well Potential

DNA molecule is modeled by a three-dimensional polymeric chain of N monomers connected by springs [5]. The potential energy V associated to the model is

$$V = V_{\text{el}}(l_i) + V_{\text{bend}}(\theta_i).$$

Here, $V_{\text{el}}(l_i) = \frac{1}{2}k_e \sum_{i=1}^{N}(l_i - l_0)^2(l_i - l_1)^2 + k_l l_i$ is a non-harmonic elastic potential energy, where k_e is the elastic parameter, $\mathbf{r}_i$ is the position of the i-th particle, $l_i = |\mathbf{r}_{i+1} - \mathbf{r}_i|$ is the distance between the monomers $i+1$ and i, and l_0 and l_1 are the minima of the potential representing approximately the equilibrium distance between adjacent monomers, in the B-DNA and the overstretched state, respectively. And $V_{\text{bend}}(\theta_i) = \frac{1}{2}k_b \sum_{i=1}^{N}[1 - \cos(\theta_i - \theta_0)]$ is the bending energy, where k_b is the bending elastic constant, and θ_i is the angle between the link $\mathbf{l}_{i+1}$ and the link $\mathbf{l}_i$. Then the overdamped equations of motion are

$$\dot{\mathbf{r}}_i = -\nabla_i V_{\text{el}}(l_i) - \nabla_i V_{\text{ben}}(\theta_i) - \sqrt{2k_B T}\,\xi(t), \tag{1}$$

where γ is the damping, T is the temperature and $\xi(t)$ represents a Gaussian uncorrelated noise. Two forces, F and $-F$, are added on the first and last monomer respectively in order to stretch the chain.

2.2 Model 2: Melting Mechanism – PBD

The same description of the previous model is kept but the energy potential is taken harmonic: $V_{\text{el}}(l_i) = \frac{1}{2}k_e \sum_{i=1}^{N}(l_i - l_0)^2$. We add an additional variable d_i that describes the strand separation at each monomer site [1]. In order to couple the melting and the stretching, the equilibrium separation between monomers has been modeled as dependent on d_i, i.e., $l_0 = l_0(d_i, d_{i+1})$: if $d_i < \tilde{d}_1$, the equilibrium distance $l_0 = \tilde{l}_1$ (B-DNA state), while for $d_i > \tilde{d}_2$, $l_0 = \tilde{l}_2$ (overstretched DNA). Between these two values, a linear dependence is used:

$$l_0(d_i, d_{i+1}) = \tilde{l}_1 + \frac{1}{2}\frac{\tilde{l}_2 - \tilde{l}_1}{\tilde{d}_2 - \tilde{d}_1}[(d_{i+1} - \tilde{d}_1) + (d_i - \tilde{d}_1)].$$

The dynamics of d_i is modeled in the framework of the standard PBD (see [4] and a modified version in [9]). The potential energy associated to this variable is composed of two terms: the on-site potential $V(d_i)$ and the staking interaction $W(d_i, d_{i-1})$. They are given by

$$V(d_i) = D(\mathrm{e}^{-\alpha d_i} - 1)^2 + G\mathrm{e}^{-(d_i - y_0)^2/b}, \tag{2}$$

$$W(d_i, d_{i-1}) = \frac{1}{2} k_W (1 + \rho e^{-\delta(d_i + d_{i-1})})(d_i - d_{i-1})^2. \tag{3}$$

The first term in the sum of (2) is the Morse potential, where the D is the energy needed to dissociate the strands at each monomer site, and α is the width of the well. The second term is a Gaussian barrier, whose height, width and position are given by G, b and y_0 respectively [9]. The non linear term of (3) changes the effective coupling constant from $k_w(1 + \rho)$ to k_w when one of the bps is displaced far away from its equilibrium position. The parameter δ sets the scale length for this behavior. To induce melting in the system, we assume that D decreases when increasing the stretching force as shown in the inset of Fig. 1.

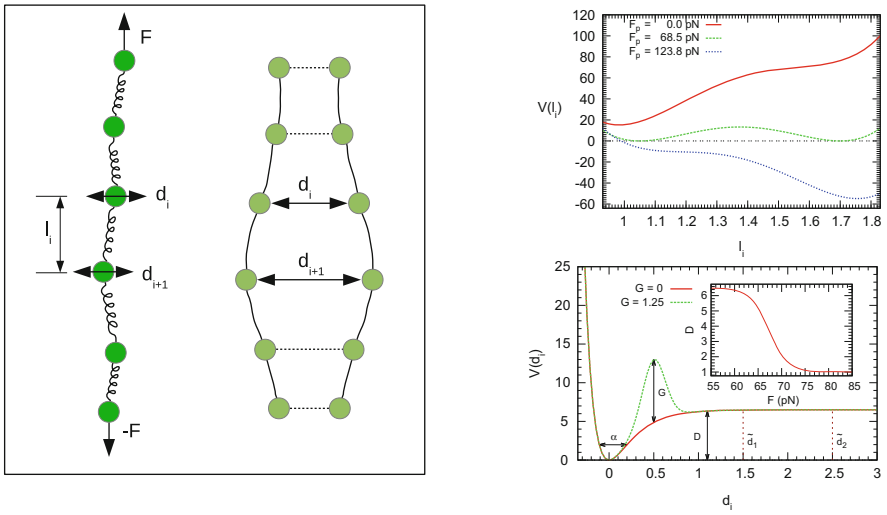

Fig. 1 *Left panel*: Scheme of the model (variable d_i is only valid for model 2). *Upper right panel*: A harmonic elastic interaction at different forces for model 1. *Lower right panel*: Morse potential used in model 2. *Inset*: dependence of D on F

3 Results and Discussion

3.1 Model 1: Double Well Potential

The left panel of Fig. 2 shows the dependence of the length on the stretching force. There is a good agreement between experimental data and simulation. The full line represents the prediction of the WLC model. A good correspondence is also observed at low force values. When the simulation time is decreased, a symmetric hysteresis is obtained, due to the slow convergence to equilibrium states (right panel of Fig. 2). This behavior has been observed in out equilibrium experiments on overstretching transition. Different stretching curves are obtained when changing parameter k_l (not shown). This parameter can be related to those whose magnitudes affect the transition as the salt concentration, pH or temperature.

3.2 Model 2: Melting Mechanism (PBD)

The dependence of the length on stretching force when melting mechanism is included is shown in the left panel of Fig. 3 for $G = 0$ and $\rho = 0$. The experimental data is also well reproduced with this model. The results for different simulation times are shown in the right panel of Fig. 3. Different to the previous description, an asymmetric hysteresis is obtained with the inclusion of the melting. This happens because during the backward experiment the closing kinetics of the bases is much slower than that one of the opening. A more realistic description is obtained by including the solvent interaction barrier in the Morse potential ($G \neq 0$).

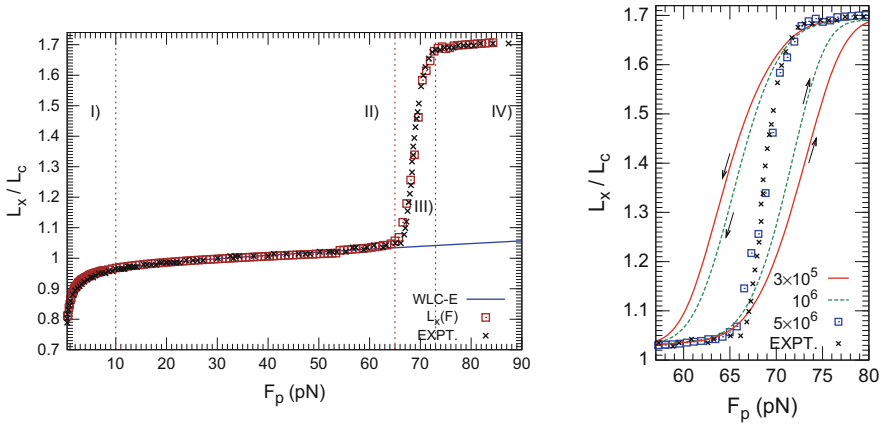

Fig. 2 *Left panel*: DNA length vs force for model 1. *Right panel*: Hysteresis in the forward and backward curves when decreasing the simulation time

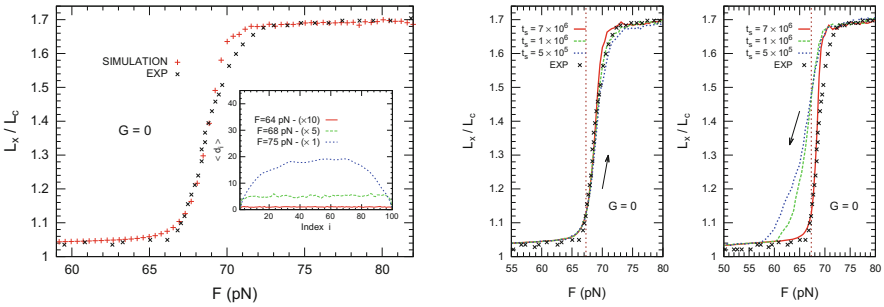

Fig. 3 *Left panel*: DNA length vs applied force F for model 2 with $G = 0$ and $\rho = 0$. *Inset*: the mean displacement $\bar{d}_i$ as a function of the monomer index i for three selected values of the force. *Right panel*: Hysteresis in the forward and backward curves when decreasing the simulation time

We have presented two mesoscopic descriptions that allow to study the overstretching transition. Although the model oversimplifies the DNA structure, it still contains the main ingredients of the molecule dynamics, especially the phenomena related to non-equilibrium properties. For instance, an important feature of the model is its ability to reproduce the hysteric behavior of the transition. The model can be extended to include other mechanisms as the stretch-twist coupling.

References

1. A.E. Bergues Pupo, F. Falo, A. Fiasconaro, J. Chem. Phys. (2013, submitted)
2. P. Cluzel, A. Lebrun, C. Heller, R. Lavery, J.L. Viovy, D. Chatenay, F. Caron, Science **271**, 792 (1996)
3. S. Cocco, J. Yan, J.F. Leger, D. Chatenay, J.F. Marko, Phys. Rev. E **70**, 011910 (2004)
4. T. Dauxois, M. Peyrard, A.R. Bishop, Phys. Rev. E **47**, 684 (1993)
5. A. Fiasconaro, F. Falo, Phys. Rev. E **86**, 032902 (2012)
6. J.F. Léger, G. Romano, A. Sarkar, J. Robert, L. Bourdieu, D. Chatenay, J.F. Marko, Phys. Rev. Lett. **83**, 1066 (1999)
7. S.B. Smith, Y. Cui, C. Bustamante, Science **271**, 795 (1996)
8. C. Storm, P. Nelson, Europhys. Lett. **62**, 760 (2003)
9. R. Tapia-Rojo, J.J. Mazo, F. Falo, Phys. Rev. E **82**, 031916 (2010)
10. J. van Mameren et al., Proc. Natl. Acad. Sci. U.S.A. **106**, 18231 (2009)
11. J.R. Wenner, M.C. Williams, I. Rouzina, V.A. Bloomfield, Biophys. J. **82**, 3160 (2002)
12. M.C. Williams, J.R. Wenner, I. Rouzina, V.A. Bloomfield, Biophys. J. **80**, 874 (2001)

Criticality on Rainfall: Statistical Observational Constraints for the Onset of Strong Convection Modelling

Anna Deluca, Álvaro Corral, and Nicholas R. Moloney

1 Introduction

A better understanding of convection is crucial for reducing the intrinsic errors present in climate models [4]. Many atmospheric processes related to precipitation have large scale correlations in time and space, which are the result of the coupling between several non-linear mechanisms with different temporal and spatial characteristic scales. Despite the diversity of individual rain events, a recent array of statistical measures presents surprising statistical regularities giving support to the hypothesis that atmospheric convection and precipitation may be a real-world example of Self-Organised Criticality (SOC) [2, 16]. The usual approach consists of looking at the occurrence of rain by days or months. For "episodic" rain events, similar to avalanches in cellular-automaton models, scale-free rain event distributions are found [13]. However, a power-law distribution (i.e., scale-free) of the observable is not sufficient evidence for SOC dynamics, as there are many alternative mechanisms that give rise to such behaviour (see for example [7, 11]).

Further support for the SOC hypothesis was given by Peters and Neelin [14], who found a relation between satellite estimates of rain rate and water vapour over the tropical oceans compatible with a phase transition, in which large parts

A. Deluca (✉)
Departament de Matemàtiques, Universitat Autònoma de Barcelona, Barcelona, Catalonia, Spain

Centre de Recerca Matemàtica, Barcelona, Catalonia, Spain
e-mail: adeluca@crm.cat

Á. Corral
Centre de Recerca Matemàtica, Barcelona, Catalonia, Spain
e-mail: acorral@crm.cat

N.R. Moloney
London Mathematical Laboratory, London, UK
e-mail: n.moloney@lml.org.uk

Á. Corral et al. (eds.), *Extended Abstracts Spring 2013*, Trends in Mathematics 2,
DOI 10.1007/978-3-319-08138-0_2

of the troposphere would be in a convectively active phase. In addition, it was shown that the system was close to the transition point. They also related it to the concept of atmospheric quasi-equilibrium [1], which argues that, since driven processes are generally slow compared to convection, the system should typically be in a far-from equilibrium statistically stationary state, where driving and dissipation are in balance. In addition, recent works have shown that local event size distributions present signs of universality in the system, as was expected in the SOC framework [5, 6, 12]. The resulting rain event size distributions were found to be well approximated by power laws of similar exponents over broad ranges, with differences in the large-scale cutoffs of the distributions. The possible consequences of this framework for the prediction of atmospheric phenomena still remain unclear.

2 Data and Methods

In this contribution we use very high-resolution (1 min) local rain intensities across different climates described in [12], stochastic convective models [15] and SOC models such as the BTW model and the Manna model, for investigating how predictable the time series of rain activity and rain event sizes are [2, 10].

We use the hazard function H_q as a decision variable, which is sensitive to clustering or repulsion between events in the time series. The conventional precursor pattern technique requires a large amount of data, does not capture long memory and has been found to perform worse than the hazard function in similar analysis [3]. The function H_q is defined as the probability that a threshold-crossing event will occur in the next Δt, conditional on no previous event within the past t_w, i.e.,

$$H_q(t_w; \Delta t) = \frac{\int_{t_w}^{t_w+\Delta t} P_q(\tau)\, \mathrm{d}\tau}{\int_{t_w}^{\infty} P_q(\tau)\, \mathrm{d}\tau}, \tag{1}$$

where q corresponds to the different thresholds on sizes and Δt is set to 1 min for the rain data and one parallel update for the SOC models. The various quantities are illustrated in Fig. 1.

Note that the hazard function gives us a probabilistic forecast and in order to perform a deterministic prediction we will need to consider a discrimination threshold.

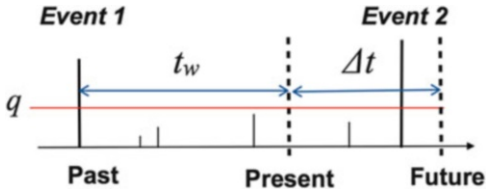

Fig. 1 Sketch of the hazard function variables

We also evaluate the quality of the prediction with the receiver operating characteristics method (ROC) [8]. For any binary prediction (occurrence or non-occurrence of an event) four possible outcomes can occur: true positive (TP), false positive (FP), true negative (TN) and false negative (FN); see Fig. 2.

ROC curves compare *sensitivity* and *specificity*. The *sensitivity* is defined as the number of correctly predicted occurrences divided by the total number of actual occurrences, and the *specificity* as the number of correctly predicted non-occurrences divided by the total number of actual non-occurrences:

$$sensitivity = \frac{\mathrm{TP}}{\mathrm{TP} + \mathrm{FN}}, \qquad specificity = \frac{\mathrm{TN}}{\mathrm{FP} + \mathrm{TN}}. \tag{2}$$

Each threshold on the decision variable will give a different point on the ROC curve. If we consider the minimum possible threshold we will always predict the occurrence of an event, for which the *sensitivity* is one and the *specificity* zero. The diagonal in Fig. 3 corresponds to random prediction. Points above the diagonal represent good predictions (better than random) and points below poor predictions.

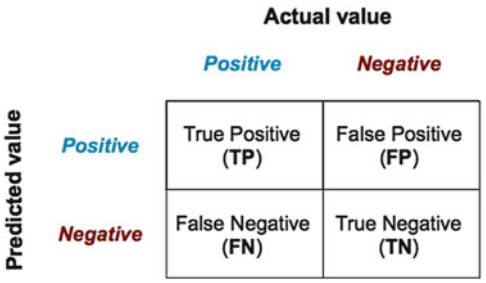

Fig. 2 Four possible outcomes of a binary prediction in a contingency table

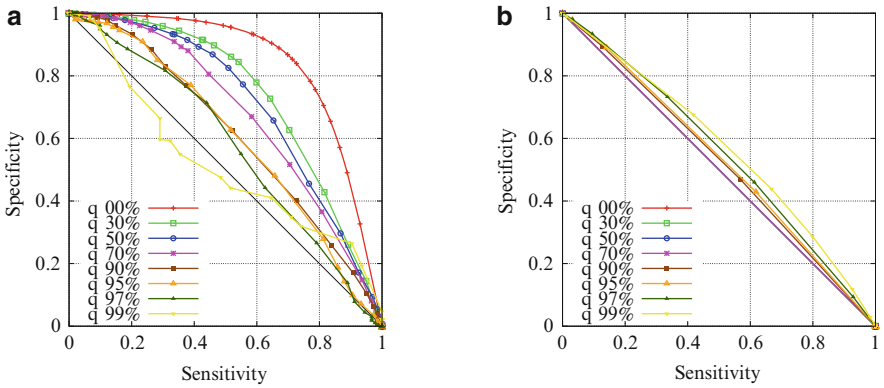

Fig. 3 Example of ROC curves data on the slow time scale for rainfall data (**a**) and for the 2D BTW SOC model simulated data (**b**)

3 Results

We find that on the events scale (slow time scale), rain data renormalise to a trivial Poisson point process for large thresholds, while for small thresholds events cluster. This is in contrast to the anti-clustering of high-threshold events in the 2D BTW model as a result of finite-size effects and the building up of correlations, seen previously by Garber et al. [9]; see Fig. 3a, b.

However, rain data has an unavoidable threshold on intensity due to the device resolution that blurs the interpretation of the results on the event scale. At the level of intensities (slow time scale), we find that prediction is insensitive to all but very high thresholds.

References

1. A. Arakawa, W.H. Schubert, Interaction of a cumulus cloud ensemble with the large-scale environment, Part I. J. Atmos. Sci. **31**(3), 674–701 (1974)
2. P. Bak, C. Tang, K. Wiesenfeld, Self-organized criticality: An Explanation of 1/f noise. Phys. Rev. Lett. **59**(4), 381–384 (1987)
3. M.I. Bogachev, I.S. Kireenkov, E.M. Nifontov, A. Bunde, Statistics of return intervals between long heartbeat intervals and their usability for online prediction of disorders. New J. Phys. **11**, 1–19 (2009)
4. Core Writing Team, R.K. Pachauri, A. Reisinger (eds.), *Fourth Assessment Report of the Intergovernmental Panel on Climate Change* (IPCC, Geneva), p. 104 (2007)
5. A. Deluca, A. Corral, Scale invariant events and dry spells for medium resolution local rain data (submitted)
6. A. Deluca, P. Puig, A. Corral, Testing universality in critical exponents: the case of rainfall (in preparation)
7. R. Dickman, Rain, power laws, and advection. Phys. Rev. Lett. **90**(10), 1–4 (2003)
8. J.P. Egan, *Signal Detection Theory and ROC Analysis* (Academic, New York, 1975)
9. A. Garber, S. Hallerberg, H. Kantz, Predicting extreme avalanches in self-organized critical sandpiles. Phys. Rev. E **80**, 1–5 (2009)
10. S.S. Manna, Two-state model of self-organized criticality. J. Phys. A: Math. Gen. **24**(8), 363–369 (1991)
11. M. Mitzenmacher, A brief history of generative models for power law and lognormal distributions. Internet Math. **1**(2), 226–251 (2004)
12. O. Peters, A. Deluca, A. Corral, J.D. Neelin, C.E. Holloway, Universality of rain event size distributions. J. Stat. Mech. P11030 (2010). http://iopscience.iop.org/1742-5468/2010/11/P11030/fulltext/
13. O. Peters, C. Hertlein, K. Christensen, A complexity view of rainfall. Phys. Rev. Lett. **88**(1), 1–4 (2002)
14. O. Peters, J.D. Neelin, Critical phenomena in atmospheric precipitation. Nat. Phys. **2**(6), 393–396 (2006)
15. S.N. Stechmann, J.D. Neelin, A stochastic model for the transition to strong convection. J. Atmos. Sci. **68**, 2955–2970
16. C. Tang, P. Bak, Critical exponents and scaling relations for self-organized critical phenomena. Phys. Rev. Lett. **60**(23), 2347–2350 (1988)

Testing Universality and Goodness-of-Fit Test of Power-Law Distributions

Anna Deluca, Pere Puig, and Álvaro Corral

Power-law distributions contain precious information about a large variety of physical processes [10]. Although there are sound theoretical grounds for these distributions, the empirical evidence giving support to power laws has been traditionally weak.

Here we present an alternative procedure, valid for truncated as well as for non-truncated power-law distributions, based on maximum likelihood estimation of the exponent, the Kolmogorov–Smirnov goodness-of-fit test, and Monte Carlo simulations [5, 7, 11]. In addition, we also present procedures for testing the existence of a single universal exponent in a collection of different data sets, based on the definition of a statistic that contains the weighted sum of the differences of the values of the exponents for all pairs of data sets.

1 Power-Law Fitting

A continuous variable x, where $a \leq x \leq b$ with b finite or infinite and $a > 0$, is power-law distributed if its probability density is given by

A. Deluca (✉)
Departament de Matemàtiques, Universitat Autònoma de Barcelona, Barcelona, Catalonia, Spain

Centre de Recerca Matemàtica, Barcelona, Catalonia, Spain
e-mail: adeluca@crm.cat

P. Puig
Departament de Matemàtiques, Universitat Autònoma de Barcelona, Barcelona, Catalonia, Spain
e-mail: ppuig@mat.uab.cat

Á. Corral
Centre de Recerca Matemàtica, Barcelona, Catalonia, Spain
e-mail: acorral@crm.cat

Á. Corral et al. (eds.), *Extended Abstracts Spring 2013*, Trends in Mathematics 2,
DOI 10.1007/978-3-319-08138-0_3

$$f(x) = \frac{\alpha - 1}{a^{1-\alpha} - b^{1-\alpha}} \left(\frac{1}{x}\right)^{\alpha}. \tag{1}$$

If $b \to \infty$ and $\alpha > 1$, the distribution is called a non-truncated power-law distribution, while for finite b the distribution is called a truncated power law, for which no restriction exists on α.

The key to fit properly power-law distributions to real-world data is to have an objective criterion to decide at which point the power law starts (and, in the truncated case, at which point it ends); this is the fitting range.

1.1 The Method

Given a sample of the random variable x with N elements as $x_1, x_2, \ldots, x_N$, we want to estimate the parameter α and determine the interval defined by a and b where the power law holds.

In order to obtain a reliable estimate of the exponent α we use maximum likelihood estimation. For that, we assume a and b as known. We compute the log-likelihood function for our particular case,

$$\ell(\alpha) = \ln \frac{\alpha - 1}{1 - r^{\alpha-1}} - \alpha \ln \frac{g}{a} - \ln a, \text{ if } \alpha \neq 1, \tag{2}$$

where $r = a/b$ and g is the geometric mean. Holding a and b fixed, the value of α which maximizes $\ell(\alpha)$ is the maximum likelihood of the exponent.

Then, the quality of the fit is assessed by a Kolmogorov–Smirnov (KS) test [12]. The KS statistic, or KS distance, d_e, is defined as the maximum difference in absolute value between the theoretical cumulative distribution and the empirical cumulative distribution, which is estimated by $n_e(x)/N$, see [3].

The KS distance allows us to calculate the p-value, the probability that, under the null hypothesis, the KS statistic takes a value larger than the one obtained empirically. As the exponent α is obtained from the data, we need to determine the distribution of the KS distance using Monte Carlo simulations. Next, we apply the same procedure for all possible ranges $[a, b]$ and compare the results. We keep the fits, i.e., the triples $\{a, b, \alpha\}$ such that the corresponding p-values are larger than a certain p_c.

Finally, we need to select objectively one fitting range among all the listed triples. For a non-truncated power law ($b = \infty$) we select the largest interval, i.e., the smaller a. If the power law is truncated we consider two different criteria for choosing the range: selecting the interval that maximizes the number of data in it, or selecting the larger log-range b/a. In fact, many true truncated power laws can be contained in the data [4]. Maximizing N tends to select power laws in the initial range on values, while maximizing the log-range tends to select power laws nearer to the tail of the distribution.

1.2 Application for the Seismic Moment of Earthquakes

In Fig. 1 one can see an illustration of the method performance results for the seismic moment (M) of earthquakes worldwide and in Southern California. Starting with the non-truncated power-law distribution, we always obtain significant power-law fit, valid for several orders of magnitude. In both cases the exponent α is between 1.61 and 1.71, but for Southern California it is more stable. For the worldwide CMT catalog restricted to shallow earthquakes the largest value of a is 3×10^{18} Nm, corresponding to a magnitude $m = 6.25$. For Southern California, the largest a found (for $p_c = 0.5$) is 1.6×10^{15} Nm, giving $m = 4$. This value is somewhat higher in comparison with the completeness magnitude of the catalog; this can be attributed to this catalog specific characteristics [7]. When a truncated power law is fitted, using the method of maximizing the number of data leads to similar values of the exponents, although the range of the fit is in some cases moved to smaller values (smaller a, and b smaller than the maximum M on the data set). The method of maximizing b/a leads to results that are very close to the non-truncated power law.

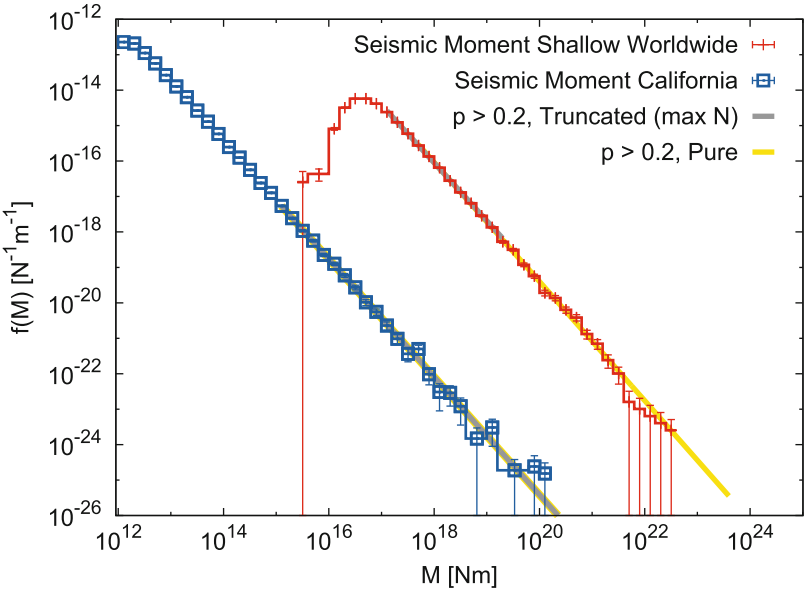

Fig. 1 Estimated probability densities and corresponding power-law fits of the seismic moment M of shallow earthquakes in the worldwide CMT catalog and of the estimated M in the Southern California catalog

2 Universality Verification

As we have just seen, the determination of the exponents of power-law distributions is not a straightforward task. However, determining the critical exponents as accurately and unbiasedly as possible, together with their associated uncertainties, is not enough for verifying universality. The exponents need to be properly compared, in order to test if they are statistically compatible.

2.1 Confidence Intervals for Exponent Differences

In the case in which one only has two different data sets with estimated exponents $\alpha_{e,1}$ and $\alpha_{e,2}$, the difference $\alpha_{e,1} - \alpha_{e,2}$ will have zero mean, under the null hypothesis. Also if data sets are independent, the standard deviation of the difference of the estimators will be $\sqrt{\sigma_{e,1}^2 + \sigma_{e,2}^2}$.

As, asymptotically, power-law MLE exponents are normally distributed [1], so will be their difference. Then, it is straightforward to obtain a confidence interval for the difference. If the interval includes the observed difference value, the null hypothesis cannot be rejected and the exponents can be considered to take the same value.

Nevertheless, the situation is not so simple when one needs to analyse three or more systems. In order to avoid the rejection of the null hypothesis by chance, corrections of the significance level, as the Bonferroni correction or the Šidák correction [2], need to be applied. However, these corrections are too generous in order to claim for universality.

2.2 The Permutation Test

For multiple testing we propose a permutation test [9]. We define a *test statistic* such that the larger its value, the stronger the evidence against the null hypothesis H_0. The null hypothesis will be that for the common range $a \leq x_j \leq b$ all exponents are the same, i.e., $\alpha_{e,i} = \alpha_{e,j}$, for all i and j.

We choose, for example,

$$\hat{\Theta} = \sum_{i=1}^{M-1} \sum_{j=i+1}^{M} (\alpha_{e,i} - \alpha_{e,j})^2, \tag{3}$$

where M is the number of data sets. More complex and powerful alternatives are considered in [8].

The scale for $\hat{\Theta}$ is provided by the *achieved significance level* or p-value of the test, which is defined as the probability that, under the null hypothesis H_0, the random variable $\hat{\Theta}$ is larger than the value we obtained for the observed data $\hat{\Theta}_{\text{data}}$, i.e.,

$$p = \text{Prob}\{\hat{\Theta} \geq \hat{\Theta}_{\text{data}} \mid H_0 \text{ is true}\}, \tag{4}$$

so the smaller the p-value, the stronger the evidence against H_0.

We will use a permutation test as a way to compute the p-value. It is based on the idea that, if the null hypothesis is correct, any data value could correspond to any data set and the data values (the size of the events in our case) are therefore interchangeable. First, we combine the $n_1 + n_2 + \cdots + n_M$ observations from all data sets into a single meta-data set (n_i is the number of data $a \leq x_j \leq b$ for each data set) and take M random samples of sizes $n_1, n_2, \ldots, n_M$ without replacement. This generates M new data sets with the same number of data than the initial ones. Next, we fit the power-law exponents (in the common fitting range) for each permuted or reshuffled data set and from their values we compute the new test statistic $\hat{\Theta}_{\text{sh}}$ (where sh stands for shuffled).

The distribution of the test statistic under the null hypothesis is obtained by repeating the process a large enough number of times. With that we can easily compute an approximation of the p-value by

$$p\text{-value} \approx \frac{\#\{\hat{\Theta}_{\text{sh}} \geq \hat{\Theta}_{\text{data}}\}}{N_{\text{sh}}}, \tag{5}$$

where $\#\{\hat{\Theta}_{\text{sh}} \geq \hat{\Theta}_{\text{data}}\}$ is the number of permutations for which $\hat{\Theta}_{\text{sh}} \geq \hat{\Theta}_{\text{data}}$.

2.3 Application for Rainfall Data

We apply the method to rain data from the Atmospheric Radiation Measurement (ARM) Program (www.arm.gov) used in [11], excluding the three sites that were found problematic there. For the rain event sizes, defined as in [11], we obtain $\hat{\Theta}_{\text{data}} = 0.051$, which leads to $p = 0.26$. So we cannot rule out the universality of the exponents.

3 Conclusions

For power-law distributions, the fitting and testing the goodness-of-fit is a difficult but very relevant problem in complex-systems science, in particular in geoscience. The most critical step is to select automatically (without introducing any subjective

bias) where the power-law regime starts and where it ends. We present a procedure that overcomes some problems found in the method introduced by Clauset et al. (2009); see [6].

We tested the performance of the method with synthetic power-law data sets and real-world data. The results for the power-law exponent of the distribution of seismic moments worldwide and in Southern California are in agreement with previous estimates, but in addition our method provides a reliable way of determining the minimum seismic-moment value for which the Gutenberg–Richter law holds.

Moreover, we present procedures for comparing the estimated critical exponents in order to test the existence of a single universal exponent [8]. The results for the rainfall data are consistent with theoretical expectations [11].

References

1. I.B. Aban, M.M. Meerschaert, A.K. Panorska, Parameter estimation for the truncated pareto distribution. J. Am. Stat. Assoc. **101**, 270–277 (2006)
2. J.M. Bland, D.G. Altman, Multiple significance tests: the Bonferroni method. Br. Med. J. **310**, 170–170 (1995)
3. R. Chicheportiche, J.P. Bouchaud, Weighted Kolmogorov–Smirnov test: accounting for the tails. Phys. Rev. E **86**, 041115 (2012)
4. A. Corral, Point-occurrence self-similarity in crackling-noise systems and in other complex systems. J. Stat. Mech. P01022 (2009)
5. A. Corral, A. Deluca, R. Ferrer i Cancho, A practical recipe to fit discrete power-law distributions (2012). ArXiv 1209:1270
6. A. Corral, F. Font, J. Camacho, Non-characteristic half-lives in radioactive decay. Phys. Rev. E **83**, 066103 (2011)
7. A. Deluca, Á. Corral, Fitting and goodness-of-fit test of non-truncated and truncated power-law distributions. Acta Geophys. **61**(6), 1351–1394 (2013)
8. A. Deluca, P. Puig, A. Corral, Testing universality of critical exponents: the case of rainfall. (2013, in preparation)
9. B. Efron, R.J. Tibshirani, *An Introduction to the Bootstrap*, 1st edn. (Chapman & Hall/CRC, New York, 1993)
10. B.D. Malamud, Tails of natural hazards. Phys. World **17**(8), 31 (2004)
11. O. Peters, A. Deluca, A. Corral, J.D. Neelin, C.E. Holloway, Universality of rain event size distributions. J. Stat. Mech. P11030 (2010)
12. W.H. Press, S.A. Teukolsky, W.T. Vetterling, B.P. Flannery, *Numerical Recipes in FORTRAN*, 2nd edn. (Cambridge University Press, Cambridge, 1992)

Stability of Strength and Weight Distributions for Time-Evolving Word Co-occurrence Networks

Francesc Font-Clos and Álvaro Corral

1 Introduction

The most intriguing and celebrated empirical law in quantitative linguistics is Zipf's law [6], which in one of its forms states that the distribution of word frequencies in a text follows a power law with exponent $\gamma \sim 2$. At least in a qualitative sense, the fulfillment of Zipf's law is astonishing, being valid no matter the author, style, or language [4–6]. An important problem of Zipf's law is the variation of the exponent γ among different samples. Although the dependence of γ with system size was firstly acknowledged by Zipf himself [6], and later on other authors have confirmed it [1, 2], few systematic studies on these dependence have been performed. This can be formulated within the framework of (directed) networks, where words (types) are nodes, and consecutive appearances of word tokens increase the weight w_{ij} of a link between the two nodes by an amount equal to one. In this way, the frequency of a word is equivalent to the strength $s_i = \sum_j w_{ij}$ of its corresponding node.

2 Results

We propose a novel and simple scaling form for the strength distribution $P_N(s)$, Eq. (1), which uncovers the robustness of this distribution as the network size N is

F. Font-Clos (✉)
Departament de Matemàtiques, Universitat Autònoma de Barcelona, Barcelona, Catalonia, Spain

Centre de Recerca Matemàtica, Barcelona, Catalonia, Spain
e-mail: fontclos@crm.cat

Á. Corral
Centre de Recerca Matemàtica, Barcelona, Catalonia, Spain
e-mail: acorral@crm.cat

Á. Corral et al. (eds.), *Extended Abstracts Spring 2013*, Trends in Mathematics 2,
DOI 10.1007/978-3-319-08138-0_4

varied [3]. In this way, the shape of the distribution is always the same and it is only a scale parameter what increases linearly with system size,

$$P_N(s) = \frac{g(s/S)}{NS}, \qquad S = \sum_{i=1}^{N} s_i \,. \tag{1}$$

By analyzing the google's n-gram data set we verify this scaling and show that the strength distribution of the English language network has been extremely stable over the past 200 years; see Fig. 1. We also study the distribution of individual weights $P_N(\omega_{ij})$, reaching an analogous scaling form,

$$P_N(w) = \frac{h(w/S)}{WS}, \qquad W = \sum_{i,j=1}^{N} \delta(w_{ij}). \tag{2}$$

In addition, the growth of $P_N(s)$ and $P_N(w)$ with system size N allow us to estimate the number of nodes N and links W as a function of the total strength S,

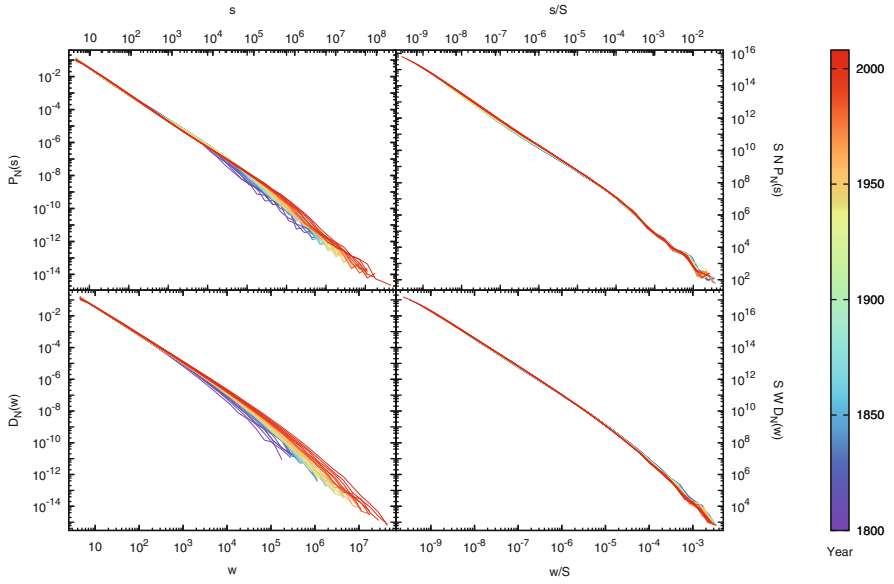

Fig. 1 $P_N(s)$ (*top*) and $D_N(w)$ (*bottom*) corresponding to the English language over the past 200 years before the rescaling process (*left*) and after it (*right*). The data collapse can be considered excellent, and the scaling functions $g(x)$ and $h(x)$ become apparent, uncovering the invariance over time of the English language network, both at the level of the strength distribution as well as at the level of the weight distribution

$$N(S) = \int_{1/S}^{\infty} g(x)\,dx, \tag{3}$$

$$W(S) = \int_{1/S}^{\infty} h(x)\,dx. \tag{4}$$

These equations provide a straightforward way to relate N and W, that is, the relation between the number of links and the number of nodes of language networks as time grows.

3 Discussion

Our findings suggest that the previous observation that the Zipf's exponent γ depends on system size [1, 2], might be an artifact of the increasing weight of a second regime in the strength distribution beyond a certain system size. The robustness of Zipf-like parameters under changes in system size opens the way to more practical applications of network science in linguistics. In particular, we provide a consistent way to compare statistical properties of language networks of different sizes.

References

1. H. Baayen, *Word Frequency Distributions* (Kluwer, Dordrecht, 2001)
2. S. Bernhardsson, L.E. Correa da Rocha, P. Minnhagen, The meta book and size-dependent properties of written language. New J. Phys. **11**, 123015 (2009)
3. F. Font-Clos, G. Boleda, A. Corral, A scaling law beyond Zipf's law and its relation with heaps' law. New J. Phys. **15**, 093033 (2013)
4. D. Zanette, Statistical patterns in written language (2012) http://fisica.cab.cnea.gov.ar/estadistica/zanette/papers/lang-patterns.pdf
5. D. Zanette, M. Montemurro, Dynamics of text generation with realistic zipf's distribution. J. Quant. Linguist. **12**(1), 29–40 (2005)
6. G.K. Zipf, *Human Behavior and the Principle of Least Effort* (Addison-Wesley, Cambridge, 1949)

Single Infection Epidemic Spreading Model

Wojciech Ganczarek

1 Introduction

It has been admitted, that the most appropriate models of epidemic spreading are those based on dynamical processes on particular graph models of networks, rather than those defined by phenomenological differential equations [1, 8]. Within this approach the nodes of a network are usually considered as individuals, who are connected with each other by vertices corresponding to social links. Although some authors use continuous time simulations (see e.g., [12]), the approach presented commonly (see [2] for a review) is based on the idea that at each discrete time step a particular node of the network can contaminate each of its neighbours with some finite probability p. The whole set of vertices is being divided into compartments, usually referred to susceptible (S), infected (I) and recovered (R) individuals, but the general mechanism stays more or less unchanged. There has been a broad range of methods developed in order to analyse such models. In the most basic approach people assume individuals to be identical and homogeneously mixed (homogeneous assumption [2]). In order to take into account heterogeneity of the system a kind of block approximation has been used [9], treating nodes with the same degree as statistically equivalent. This is not always enough, as some real networks manifest degree correlations [10]. The next step thus is to take into account those correlations [3]. Finally, one can employ whole adjacency matrix describing the graph we analyse [6]. The validity of all these approaches is still under investigation; see e.g., [5]. Note however, that all

W. Ganczarek (✉)
Institute of Mathematics and Institute of Physics, Jagiellonian University, Kraków, Poland
e-mail: w.ganczarek@gmail.com

Á. Corral et al. (eds.), *Extended Abstracts Spring 2013*, Trends in Mathematics 2,
DOI 10.1007/978-3-319-08138-0_5

these variations listed above work on equations describing relationships between probability vectors. The problem, however, is that there is not a single moment when a particular vertex is, say, 0.41 infected. A vertex can be either infected (1) or not (0). This problem has been already noticed by Petermann and De Los Ríos [11].

In our paper [4] we introduce another model of epidemic spreading and analyse it with completely different approach. For instance, in case of sexual transmitted diseases the assumption that a particular node is able to contaminate more then one of its neighbours during a time step seems not to be the most suitable one. Bearing this idea in mind we developed a single infection epidemic spreading model.

2 Model Description

Consider a connected, unweighted graph with n vertices enumerated by indices $i = 1, \ldots, n$, described by transition matrix $\{P_{ij}\}$, $\sum_{j=1}^{n} P_{ij} = 1$. The model is of SIS kind: all the individuals are at the beginning considered as susceptible (S). After contamination they become infected (I) but they still have a chance to recover and be susceptible again.

We start thus with the all but one nodes susceptible. The one which is infected is chosen at random. At each time step we choose randomly a node, say the i-th one, with identical probability $1/n$. Then we choose its neighbour according to the transition matrix $\{P_{ij}\}$, i.e., there is P_{ij} chance that we point j-th vertex. If one of these two individuals i, j is infected, it contaminates the second one with probability z. At the end of each time step we recover each infected node with probability r.

What could be a real-life realisation of such a model? In large, academic cities there are often big flats situated in old tenement houses, settled by quite large amounts of students, who live with 3–4 roommates per chamber. As there is no space for privacy in this way of living, they sometimes devote one room in the flat to be a so-called *sex-room*, so contamination by sexually transmitted diseases can take place at most once per time step (say: per night). This seems to be a good example of a system which can be described by our model.

3 Model Analysis

In order to mathematically describe the model we define $X_j(t)$ which takes the value 1 if the node j is being contaminated by one of its neighbours at the time step t, and 0 otherwise. Furthermore, we denote the set of all infected nodes at the

time step t by $I(t)$. The equation for $D(t)$ describing the evolution of the process reads

$$D(t) = \mathbb{E}(|I(t+1)| - |I(t)|^2) = \frac{z}{n}\Big(\sum_{k\in I(t),\, j\notin I(t)} P_{jk} + \sum_{k\in I(t),\, j\notin I(t)} P_{kj}\Big) - r|I(t)|. \tag{1}$$

The full reasoning can be found in [4].

3.1 Epidemic Threshold

Our first aim is to find out the epidemic threshold for the process described above. We are interested in a relation of model parameters n, z, r that defines a border between two situations: dropping and rising of the number of infected nodes in the beginning of the process. However, classical epidemic threshold is defined in the limit of large size of a network [2]. Here, as we focus on finite networks only and the impact of their size onto the process, we need a different definition of epidemic threshold. In order to construct it, we follow the method of computing thresholds for infinite networks. In continuous approximation one obtains the epidemic threshold using assumption of small number of infected nodes, which is true in the vicinity of $t = 0$. The smallest finite number of infected nodes we can take is 1, so we define epidemic threshold as follows:

Definition 1. Epidemic threshold for the single infection epidemic spreading model is the relation between parameters z, r and network size n such that $D(0) = 0$.

Theorem 2. *Epidemic threshold for the single infection epidemic spreading model is given by*

$$\frac{z}{r} = \frac{n}{2}.$$

Proof. By definition of the model $|I(0)| = 1$. Denote the only infected node by l, we have $\mathbb{P}(I(0) = \{l\}) = 1/n$. Then also $\sum_{k\in I(0),\, j\notin I(0)} p_{kj} = \sum_{j\neq l} p_{lj} = 1$ (as P-stochastic) and $\sum_{k\in I(0),\, j\notin I(0)} p_{jk} = \sum_{j\neq l} p_{jl}$, hence

$$D(0|\{l\}) = \frac{z}{n}\Big(1 + \sum_{j\neq l} p_{jl}\Big) - r.$$

Furthermore, using the fact that for all j there is $p_{jj} = 0$, we have

$$D(0) = \frac{1}{n}\sum_{l=1}^{n}\frac{z}{n}\Big(1+\sum_{j=1}^{n}p_{jl}\Big) - r = \frac{z}{r}\Big(1+\frac{1}{n}\sum_{j=1}^{n}\sum_{l=1}^{n}p_{jl}\Big) - r = \frac{2z}{n} - r.$$

Condition $D(0) = 0$ indicating the epidemic outbreak completes the proof. □

3.2 Stationary State

The stationary fraction of infected nodes (not specifying any particular shape of the graph) is not as easy reachable as the threshold calculated in the last section. We basically need to find the solution for the equation $D(t) = 0$ without the constraint $|I(t)| = 1$. The problem is to compute the sum $\sum_{k\in I(t),\, j\notin I(t)} P_{jk}$, which in general depends on $I(t)$. We will thus estimate only the stationary state in the general case (see [4]) by using the notion of graph conductance; see e.g., [13]. Here we focus on exact solutions for special cases of complete graph and uncorrelated homogenous graph.

Complete Graph

For complete graphs, i.e., graphs with all possible links present, we easily find the exact solution of stationary state problem. Note that, for this special case,

$$\sum_{k\in I(t),\, j\notin I(t)} P_{jk} = \sum_{k\in I(t),\, j\notin I(t)} P_{jk} = \frac{|I(t)|(n-|I(t)|)}{n-1} \tag{2}$$

as each of the $|I|$ infected nodes is linked to each of the $(n-|I|)$ susceptible nodes by an edge chosen with probability $1/(n-1)$ as each node has $n-1$ neighbours. We can thus find an explicit and exact condition for $D(t) = 0$. From (1) and (2) we get

$$i(t)_s = 1 - \frac{r(n-1)}{2z}. \tag{3}$$

Uncorrelated Homogeneous Graph

For uncorrelated and homogeneous sums in (1) also simplify in a sense, such that we obtain [4] the stationary infected nodes density of the form

$$i_s = 1 - \frac{r(n-1)}{2z\langle\frac{1}{k}\rangle\langle k\rangle}, \tag{4}$$

where we denote $\langle k \rangle = \mathbb{E}(k)$ and $\langle 1/k \rangle = \mathbb{E}(1/k)$. Specifically, for $G(n, p)$ random graph (with the well-known binomial degree distribution) the product $\langle 1/k \rangle \langle k \rangle$ goes to 1. In this case the latter result (4) recovers the solution for complete graphs (3). Moreover, $G(n, p)$ graphs are indeed uncorrelated in the limit of large n [7], so we expect $G(n, p)$ behaving like complete graphs for large n.

3.3 Mixing Time

In this section we will be interested in mixing time, i.e., the time needed by the process to reach the stationary state. Strictly speaking, this is some kind of metastable stationary state, as in simulations on finite networks the only absorbing, stable state is the situation when the number of infected nodes is zero. We prove [4] a theorem, that mixing time scales like $\log n$.

Theorem 3. *Let P be a stochastic transition matrix of a graph G of the size n. Mixing time, T, is linear with inverse of the distance, η, from the epidemics threshold and logarithm of size n of the network, i.e.,*

$$T(\eta, n, \epsilon) = O\Big(\frac{1}{\eta}(\log n + \log \epsilon^{-1})\Big).$$

This means that the probability that the time t needed to reach the stationary state is greater than some

$$t_c = O\Big(\frac{1}{\eta}(\log n + \log \epsilon^{-1})\Big)$$

is smaller than ϵ, i.e., $\mathbb{P}(t > t_c) \leq \epsilon$. Here, η stands for distance from epidemic threshold in units of critical value of the ratio z/nr; see [4] for more details.

3.4 Simulations

All of the theoretical results described above has been examined by computer simulations showing perfect agreement [4]. Here we present, as an example, dependence on contamination probability z of stationary fraction of infected nodes for complete graphs; see Fig. 1.

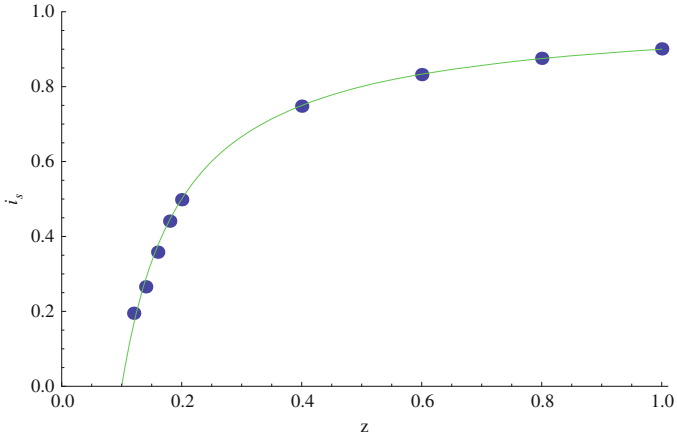

Fig. 1 Plot of stationary state value of infected nodes density i_s for complete graphs versus contamination probability z: simulation (*blue dots*) and theoretical result (3) (*green line*). We fix here n=100, r=0.002

Acknowledgements It is a pleasure to thank D. Kwietniak and P. de los Ríos for fruitful discussions.

References

1. R.M. Anderson, R.M. May, *Infectious Diseases of Humans. Dynamics and Control* (Oxford University Press, Oxford/New York, 1992)
2. A. Barrat, M. Barthlemy, A. Vespignani, *Dynamical Processes on Complex Networks* (Cambridge University Press, Cambridge/New York, 2008)
3. M. Boguñá, R. Pastor-Satorras, A. Vespignani, Phys. Rev. Lett. **90**, 028701 (2003)
4. W. Ganczarek, e-print arXiv:1304.1437 [physics.soc-ph] (2013)
5. A.V. Goltsev, S.N. Dorogovtsev, J.G. Oliveira, J.F.F. Mendes, Phys. Rev. Lett. **109**, 128702 (2012)
6. S. Gómez, A. Arenas, J. Borge-Holthoefer, S. Meloni, Y. Moreno, Europhys. Lett. **89**, 38009 (2010)
7. M.E.J. Newman, Phys. Rev. Lett. **89**, 208701 (2002)
8. M.E.J. Newman, SIAM Rev. **45**, 167 (2003)
9. R. Pastor-Satorras, A. Vespignani, Phys. Rev. Lett. **86**, 3200 (2001)
10. R. Pastor-Satorras, A. Vespignani, *Evolution and Structure of the Internet: A Statistical Physics Approach* (Cambridge University Press, Cambridge/New York, 2004)
11. T. Petermann, P. de los Ríos, J. Theor. Biol. **229**, 1 (2004)
12. A.S. Saumell-Mendiola, M. Ángeles Serrano, M. Boguñá, Phys. Rev. E **86**, 026106 (2012)
13. A. Sinclair, *Algorithms for Random Generation and Counting: A Markov Chain Approach* (Birkhäuser, Boston, 1993)

Niche Dimension as an Emergent Property of Food-Web Structure

Virginia D. Ganfornina, Samuel Johnson, and Miguel Ángel Muñoz

Ecosystems are often described as food webs: networks in which nodes are species and links stand for predation. The research in the field of these ecological networks is becoming more and more relevant given the increasing pressure the ecosystems are facing, which makes the study of their topology specially interesting due to its interconnection with the dynamical processes taking place in it. The concept of the ecological niche of a species has been discussed for a long time. The term was originally used to refer to a species habitat or ecological role. It was then re-defined by Hutchinson as a position in a multi-dimensional hyperspace—each dimension being some biologically relevant magnitude [2]. When Cohen first compiled a database of empirical food webs and studied them quantitatively, he discovered that many of the networks had the property he called *intervality*: the columns of the adjacency matrix representing the ecosystem could be ordered in such a way that the prey of any predator were all contiguous (they form an unbroken interval) [1]. This could be interpreted as meaning that a given species would eat every species within a particular compact hyper-volume of the niche space, and that this hyper-volume could be projected onto only one dimension, a single *niche-axis*. More recently the degree of intervality of food webs has been measured with several continuous magnitudes that are close to unity if most of the prey form unbroken intervals or

V.D. Ganfornina (✉) • M.Á. Muñoz
Departamento de Electromagnetismo y Física de la Materia, Universidad de Granada, Granada, Spain

Instituto Carlos I de Física Teórica y Computacional, Granada, Spain
e-mail: domgarvir@gmail.com; mamunoz@onsager.ugr.es

S. Johnson
Oxford Centre for Integrative Systems Biology, University of Oxford, Oxford, UK

Department of Physics, University of Oxford, Oxford, UK
e-mail: s.johnson1@physics.ox.ac.uk

Á. Corral et al. (eds.), *Extended Abstracts Spring 2013*, Trends in Mathematics 2,
DOI 10.1007/978-3-319-08138-0_6

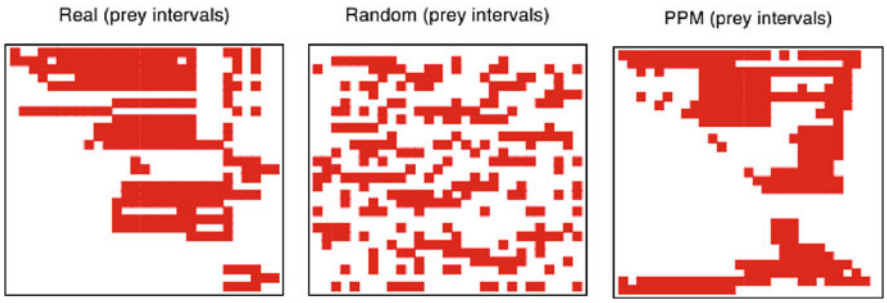

Fig. 1 *Left panel*: Adjacency matrix corresponding to the food web of Coachella Valley. A *red square* means that the predator (vertical axis) eats the prey species (horizontal axis) in question. An ordering of the species has been sought which maximises prey-intervality ξ: the prey of any predator tend to be contiguous ($\xi = 0.89$). *Central panel*: The same for a random null-model corresponding to the Coachella food web, in which links have been allocated randomly ($\xi = 0.51$). *Right panel*: Adjacency matrix for a network generated with the Preferential Preying Model (PPM), with the same parameters as the food web of Coachella Valley, ordering species to maximize intervality: $\xi = 0.91$

approach zero when very few do, with most ecosystems being nearly interval. This is a highly non trivial feature of real food webs, which are indeed significantly more interval than the random graph as can be seen in Fig. 1.

The fact that only one niche dimension could account for the intervality of food webs was the central idea behind many models that were put forward to show that the evident complexity of food webs could come about via simple rules. All these niche-based models make the same assumption implicit in the Niche Model—that some hidden niche dimension lies behind the formation of intervals, and so of the structure of food webs [3, 4]. That is, if the niche dimension corresponded to body size, then it would mean that a given species were capable of eating only prey within a particular range of body sizes. But neither body size, nor longevity, nor any other magnitude studied nor combinations thereof have been found to explain this ordering satisfactorily. Hence, the meaning of this dimension has remained a mystery.

We wondered if this dimension is needed to explain the network features for which it was originally invoked, and if the ordering that maximises intervality necessarily reflect some natural hierarchy among species.

We propose a model (Preferential Preying Model) in which species are added sequentially to the network and prey are selected according to a pure topological property—their trophic level—in order to study the intervality of ecosystems. Analyzing a set of 16 food webs from literature we show the empirical values of intervality for these food webs contrasted with those obtained with the PPM after adjusting its parameter to better simulate each ecosystem. In most of the cases the observed intervalities are significantly high when compared to the null-models and they can usually be reproduced by the PPM with the right choice of its parameter. Analysis of some structural features that are of particular ecological relevance (the distributions of degrees, the modularity, the mean chain length, and the distribution of trophic levels) are also performed.

The agreement is very good in all cases, indicating that this simple model generates networks which are remarkably similar to food webs. We show that a simple mechanism for network assembly that does not make use of a niche axis, but only of information in the emerging structure of the network itself, generates networks that are realistically interval. Intervality emerges naturally from structural features of food webs, features that can be easily generated in biologically plausible yet fairly simple ways. That the only parameter has been tuned so as to best approximate intervality, with no regard for these other features, suggests that preferential preying according to trophic distance may actually reflect some essential mechanism behind the formation of food webs.

If our model generates networks that resemble real food webs this is most likely because the trophic level of a species is a sufficiently good proxy of its characteristics. This does not mean that the best ordering is somehow encoded in the biological characteristics themselves. On the contrary, in our model and, we argue, probably also in nature this ordering is only determined once the links have been (stochastically) established. Thus, networks that are highly stratified (well defined trophic levels) will have higher values of intervality than those lacking this structure. This is illustrated in Fig. 2. In the network in the top panels (generated

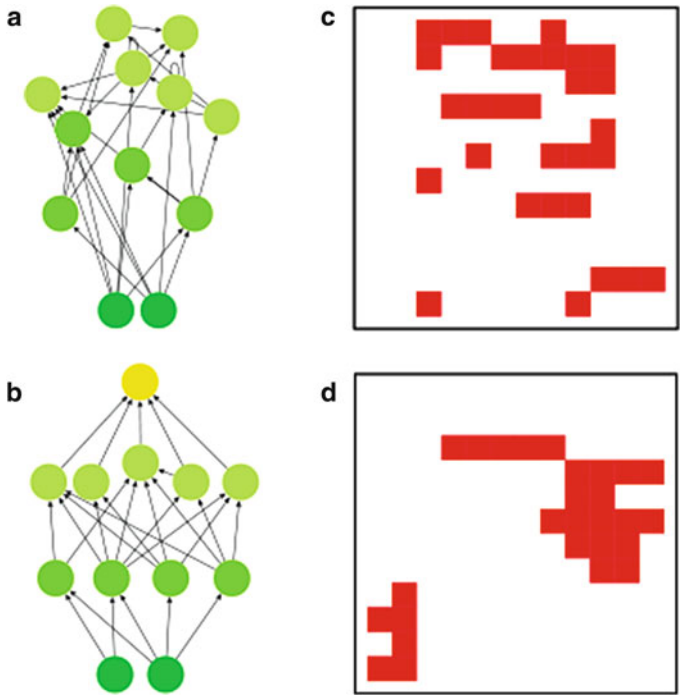

Fig. 2 (**a**) PPM network generated with 12 species and $T \to \infty$ (the height of each node is proportional to its trophic level). (**b**) As A but for $T = 0$. (**c**) Adjacency matrix corresponding to the network in (**a**), with rows and columns placed according to the ordering that maximises prey intervality: $\xi = 0.88$. (**d**) As (**c**) but for the network in (**b**), which has $\xi = 1$ ((**a**) and (**b**) generated with Pajek)

with $T \to \infty$, not well defined levels), an ordering must be sought for all 12 species simultaneously, whereas in the one underneath ($T = 0$, with a well defined stratified structure), the three blocks can be put in order almost independently. It follows that stratification is not the only structural feature to induce intervality. Any network characteristic that reduces the extent to which the ordering of one group of nodes constrains the orderings available to other groups will have this effect.

There is probably no reason to search for a hidden niche dimension as the cause behind the structure of food webs. This does not imply that the concept of niche space as a representation of ecosystems looses any of its utility but that the most interval ordering for a given food web does not necessarily reflect the niche in any way. However, the fact that all the non-trivial network features analysed are reproduced so well by a simple model, which only imposes on predators a measure of trophic-level specialization, suggests that much of the complexity of food webs might come about from mechanisms that are simpler than has so far been presumed. With this is mind we can conclude therefore that the niche dimension—in the sense used for modelling—is in fact an emergent property of food-web structure, which calls for a fundamental change in perspective as to how ecosystems arise and persist.

References

1. J.E. Cohen, Food webs and the dimensionality of trophic niche space. Proc. Natl. Acad. Sci. U.S.A. **74**, 4533–4563 (1977)
2. G.E. Hutchinson, Concluding remarks. Cold Springs Harb. Symp. Quant. Biol. **22**, 415–427 (1957)
3. D.B. Stouffer, E.L. Rezende, L.A.N. Amaral, The role of body mass in diet contiguity and food-web structure. J. Anim. Ecol. **80**, 632–639 (2011)
4. R.J. Williams, N.D. Martínez, Success and its limits among structural models of complex food webs. J. Anim. Ecol. **77**, 512–519 (2008)

Modelling the Population Dynamics in a Cell Culture at Two Different Scales

M. Gokhan Habiboglu and Yagmur Denizhan

1 Introduction

The main purpose of this study is to model the population dynamics in a eukaryotic cell culture. Besides providing an insight into the important aspects of modelling at different scales and the relation between these models, the study is supposed to allow the prediction of the time profile of the total population size within an admissible tolerance.

For this purpose the growth, proliferation and death dynamics of a cell culture is studied, where the cells are assumed to belong to a genetically modified eukaryotic mammalian cell line, as widely used in many cell culture experiments. As a result of genetic modification the behaviour of such cells is confined to two different modes:

1. Active Mode: A cell remains in active mode as long as its neighbourhood is not too crowded. In this mode the cell keeps on growing until it reaches a mature size and undergoes mitotic division.
2. Quiescent Mode: A cell enters the quiescent mode as a reaction to an over-crowded neighbourhood. In this mode growth and proliferation is halted.

Cells can switch between these modes depending on local population. Another cell activity which is independent of these modes is toxicity release. Without loss of generality cell deaths in a cell culture can be ascribed to the lethal effects of toxicity accumulated in the flask. It should be noted that death of some cells in a neighbourhood will reduce local population density and allow quiescent cells in the

M.G. Habiboglu (✉) • Y. Denizhan
Electrical and Electronics Engineering Department, Bogazici University, Istanbul, Turkey
e-mail: ghabiboglu@gmail.com; denizhan@boun.edu.tr

Á. Corral et al. (eds.), *Extended Abstracts Spring 2013*, Trends in Mathematics 2,
DOI 10.1007/978-3-319-08138-0_7

Table 1 Different scales at which population dynamics can be modelled

Scale	Focus	Modelling approach	Source of knowledge
Micro	Intracellular dynamics	Not modelled in this study	
Meso	Dynamics of individual cells	Agent-based	Biological knowledge and experimental observations
Macro	Global dynamics of the cell culture	Differential equation-based	Concepts derived from the meso-scale model

vicinity switch to the active mode. The population dynamics of such a cell culture can be modelled at different scales as summarised in Table 1.

In this study, an agent-based meso-scale model and a differential-equation based macro scale model have been developed.

2 Meso-scale Model

In the meso-scale model the flask is represented as a $n \times n$ grid. Each mesh in the grid is called a "locus" and it is assumed that it can accommodate only a single cell. The mesh size is chosen appropriately to make this assumption admissible. This discrete-time model ($\Delta k = 1$ is equivalent to 15 min in real life dynamics) represents the cell dynamics as follows: nutrition concentration in the flask remains constant and uniform; and growth, mitotic division, toxicity release, aging and death of a cell are related to and represented in terms of the cells energy:

- *Cell growth*, due to nutrient intake, is represented in terms of energy increase. Each cell can take in only a constant quantity of energy (A) at each time step.
- When a cell attains the level of "division energy" (E_{div}) it divides into two daughter cells, each receiving half of the division energy ($E_{\text{div}}/2$). Daughter cells are placed at any random 2 empty loci among the locus of the mother cell and its 8 nearest neighbourhood of the mother cell. (The random choice of the loci of daughter cells within this narrow neighbourhood constitutes the only non-deterministic element in the meso-scale model.)
- The *toxicity* is related to the cell dynamics via the damage it causes in the cells. Therefore; the amount of toxicity at a locus (i, j) is expressed as the amount of energy ($E_{\text{rem}}(x_{i,j})$) a cell would have to spend in order to remedy the damage caused by being exposed to such a toxicity ($x_{i,j}$). Each living cell releases a constant amount of toxicity per time step, which diffuses with some given diffusion constant. For the sake of convenience, the amount of toxicity released per time step is expressed as a fraction of the constant energy intake per time step.

- *Cell aging* is represented as loss of energy when the remediation expenditures due to local toxicity exceeds the constant energy intake.
- *Cell death* is represented as vanishing of the cell energy due to aging.

This model represents the state of the cell culture system in terms of the instantaneous local toxicity ($x_{i,j}(k)$) at locus (i, j) and the instantaneous energy ($E_{i,j}(k)$) of the cell at locus (i, j) for all $i, j = 1, \ldots, N$.

3 Macro-scale Model

Since the main modelling task is to predict the evolution of the population size, the total population is the most obvious state variable of the macro scale model. Furthermore, with the insight gained from the meso-scale model, total toxicity in the flask and the distribution of energy across the cell culture have been identified as the most important factors affecting the population dynamics. Although simulations of the meso-scale model reveal a non-uniform energy distribution across the population with time-varying statistical properties, as a first approximation the energy distribution has been modelled as uniform between time-variable lower and upper boundaries. Hence, the macro scale model is based on the following four state variables: $p(t)$, the total population; $\zeta(t)$, the total toxicity; and η_{low} and η_{high}, the lower and upper boundaries of the energy distribution, respectively.

Table 2 shows the assumptions and intermediate variables used in the derivation of the following set of differential equations (1)–(4), describing the macro scale cell culture dynamics:

$$\frac{dp}{dt} = [p(t) - q(t)]\,\Delta_{\text{high}} u(\Delta_{\text{high}}) - p(t)\Delta_{\text{low}} u(\Delta_{\text{high}}), \qquad p(0) = p_0, \tag{1}$$

Table 2 Assumptions and intermediate variables used in Eqs. (1)–(4)

Variable	Assumption
Total population $p(t)$	Uniformly distributed across the flask $\forall t \geq 0$
Total toxicity $\zeta(t)$	No initial toxicity uniformly distributed across the flask (high enough diffusion rate)
Total quiescent population $q(t)$	Define: average # of blank loci per living cell $= b(t) = \frac{n^2 - p(t)}{p(t)}$ $b(t) \geq 1 \Leftrightarrow \frac{n^2}{2} \leq p(t) \leq n^2 \Rightarrow q(t) \approx 0$ $0 \leq b(t) < 1 \Leftrightarrow 0 \leq p(t) < \frac{n^2}{2} \Rightarrow q(t) \approx 2p(t) - n^2$
Energy distribution $f_E(E_o)$	Initially uniformly distributed between $\hat{E}_{\text{div}}/2$ and $\hat{E}_{\text{div}}$ uniformly distributed between η_L and η_H $\forall t \geq 0$
Average rate of remediation energy $\bar{\epsilon}_{\text{rem}}$	Define: average toxicity per locus $= \xi(t) \approx \frac{\zeta(t)}{n^2}$ $\bar{\epsilon}_{\text{rem}} \approx \hat{c}\,\xi(t) \approx \frac{\hat{c}\,\zeta(t)}{n^2}$ (high enough diffusion rate)

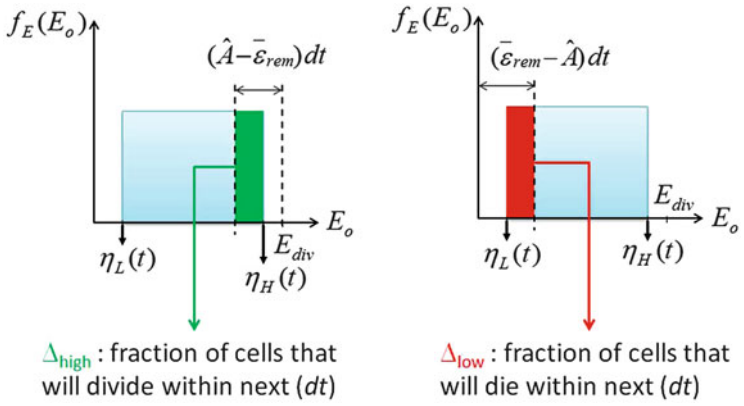

Fig. 1 Illustrations of Δ_{high} and Δ_{low} used in Eq. (1)

$$\frac{d\zeta}{dt} = \hat{\beta}\hat{A}p(t), \qquad \zeta(0) = 0, \tag{2}$$

$$\frac{d\eta_H}{dt} = \begin{cases} 0 & \text{if } \bar{\epsilon}_{\text{rem}}(t) \le \hat{A} \\ \left[\hat{A} - \bar{\epsilon}_{\text{rem}}(t)\right] u(\eta_H(t)) & \text{if } \bar{\epsilon}_{\text{rem}}(t) > \hat{A}, \end{cases} \qquad \eta_H(0) = \hat{E}_{\text{div}}, \tag{3}$$

$$\frac{d\eta_L}{dt} = \begin{cases} 0 & \text{if } \bar{\epsilon}_{\text{rem}}(t) \le \hat{A} \\ \left[\hat{A} - \bar{\epsilon}_{\text{rem}}(t)\right] u(\eta_L(t)) & \text{if } \bar{\epsilon}_{\text{rem}}(t) > \hat{A}, \end{cases} \qquad \eta_L(0) = \frac{\hat{E}_{\text{div}}}{2}. \tag{4}$$

Here, $\hat{A}$, $\hat{\beta}$, $\hat{c}$, $\hat{E}_{\text{div}}$ are the estimates of the macro-scale model parameters and obtained from observed population data under simplifying assumptions (Fig. 1).

4 An Emergent Oscillation

Simulations of the meso-scale model reveal that the energy distribution exhibits unexpected oscillatory characteristics during population growth (Fig. 2). These simulation results correspond to oscillatory characteristics in the cell size distribution across the cell culture.

Whether such emergent oscillations in cell size distribution are indeed observed in cultures with asynchronous cell division needs further investigation.

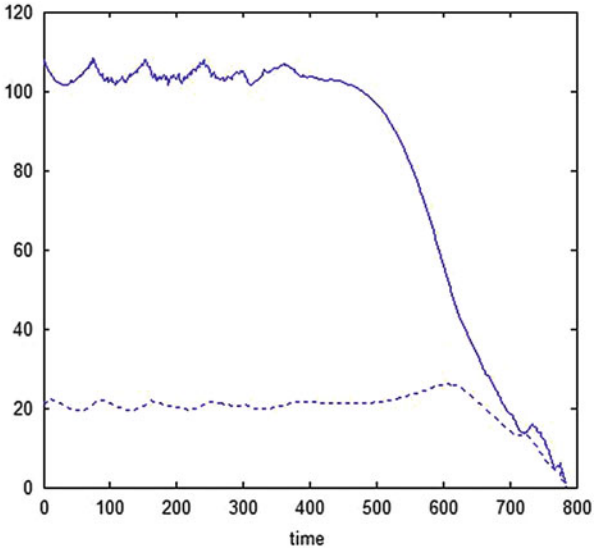

Fig. 2 The evolution of the mean (*solid line*) and standard deviation (*dashed line*) of the population-wide energy distribution

5 Results and Conclusion

An agent-based meso-scale model and a differential equation-based macro scale model have been developed for cell cultures containing genetically modified eukaryotic mammalian cell lines (no differentiation unless specially treated).

Under assumptions mentioned above, meso and macro scale models provide similar results for total population and total toxicity. Provided that the macro-scale parameters are properly estimated using some simple empirical measurements the macro-scale model allows the prediction of the population size as a function of time for a reasonable range of initial conditions.

During the simulation of the meso-scale model emergent oscillatory characteristics have been observed in the distribution of energy across the cell population. This behaviour has not been accounted for in the macro scale model because it is not relevant for the specific practical purpose of this study (Fig. 3).

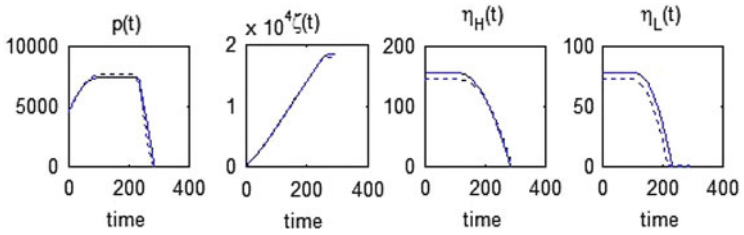

Fig. 3 Time evolution of the macro scale state variables (*solid*) and their counterparts obtained from the meso-scale model (*dashed*) for a uniformly distributed initial population filling the 44 % of the flask and a diffusion rate of $D = 0.2$

Assessing the Significance and Predicting the Effects of Knockout Cascades in Metabolic Networks

Oriol Güell, Francesc Sagués, and M. Ángeles Serrano

We explore the effects of different forms of structural stress on the robustness of metabolic networks and we use two different kinds of randomization methods [4,5]. We also explore the effects of single and multiple gene knockouts in the metabolic network of a genome-reduced bacterium.

1 Methods

The cascading failure algorithm is applied to spread the initial perturbation through the network and to compute the corresponding damage. Crucial to the algorithm is the concept of viability. A metabolite is considered viable if it has at least one incoming and one outgoing connection, so as to prevent depletion or accumulation. On the other hand, reactions are viable if and only if all of the participating metabolites are viable.

Benchmark cascades are computed by first randomizing the original network and then performing the cascade algorithm on the randomized version. Damage distributions are obtained for a hundred realizations, then averaged, and finally compared to the original damage distribution to assess the statistical significance and quantitative behavior of the observation.

O. Güell (✉) • F. Sagués
Departament de Química Física, Universitat de Barcelona, Barcelona, Catalonia, Spain
e-mail: oguell@ub.edu; f.sagues@ub.edu

M.Á. Serrano
Departament de Física Fonamental, Universitat de Barcelona, Barcelona, Catalonia, Spain
e-mail: marian.serrano@ub.edu

Á. Corral et al. (eds.), *Extended Abstracts Spring 2013*, Trends in Mathematics 2,
DOI 10.1007/978-3-319-08138-0_8

The degree preserving randomization (DP) method works by choosing a pair of links of the network at random and swapping their targets, unless this would lead to the repeated occurrence of a metabolite in a reaction [4].

Mass-balanced randomization (MB) generates randomized networks by rewiring the links corresponding to substrate-reaction or product-reaction relationships, while preserving atomic mass balance of the reactions [1]. As biological systems and their properties evolve under physical constraints and evolutionary pressure, a null model which satisfies physical principles but does not account for evolutionary pressure differs from a metabolic network only in the properties which are affected by evolutionary pressure. Thus, a property deemed statistically significant following mass-balanced randomization is beyond basic physical constraints and it is likely to be a result of evolutionary pressure [2].

2 Results

2.1 Failures of Single and Pairs of Reactions

We study cascades triggered by individual removal of reactions by removing each reaction of the network individually. We define the size of a cascade, d_r, or damage caused by the removal of a reaction r as the number of resulting non-viable reactions. We use the metabolic networks of *Mycoplasma pneumoniae*, *Escherichia coli* and *Staphylococcus aureus*.

The cumulative probability distributions $P(d'_r \geq d_r)$ give the probabilities that a damage is at least as large as d_r, and may be interpreted as a measure of the robustness of a network with respect to reaction removal. We determine the cumulative probability distributions of the damages in the three metabolic networks and compare them to the averaged distributions associated to their randomized variants from degree preserving randomization for *M. pneumoniae* and degree preserving and mass-balanced randomization for *E. coli* and *S. aureus*; see Fig. 1.

We observe that the distributions of the original networks lie in between the distributions of the two null models. Thus, the robustness of the analyzed networks cannot be explained by the distribution of degrees or by basic physical constraints. For the DP null model, this finding indicates that robustness is positively influenced by factors which are independent of the degrees. The results from the MB null model suggest that evolutionary pressure leads to larger cascades of non-viable reactions, and thus lower robustness.

To check whether or not the cumulative probability distributions significantly differ between the original networks and their randomized variants, we perform Kolmogorov–Smirnov tests; see Table 1. In this case, the compared distributions are considered significantly different.

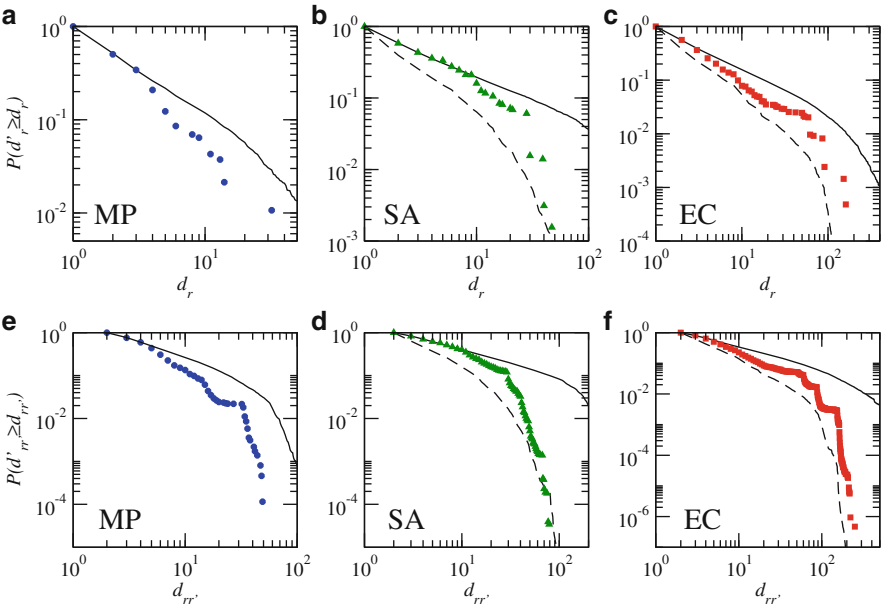

Fig. 1 Distributions of damage caused by removal of reactions. *M. pneumoniae* (*blue*), *S. aureus* (*green*) and *E. coli* (*red*). Averaged distributions are shown for DP (*continuous line*) and MB (*dashed line*). (**a**)–(**c**) Single reaction failures. (**d**)–(**f**) Pairs of reactions failures

Table 1 Kolmogorov–Smirnov tests for single reaction (SR) and pairs of reactions (PR) failure cascades. Values of the KS statistic/associated significance level are given

	SR		PR	
Organism	MB	DP	MB	DP
S. aureus	0.19/0	0.085/0.0002	0.27/0	0.15/0
E. coli	0.19/0	$0.082/2 \cdot 10^{-12}$	0.21/0	0.13/0

2.2 *Impact of Gene Knockouts in Metabolic Structure*

We coupled the metabolic network of *M. pneumoniae* to its gene co-expression network through the activity of enzymes and we considered knockouts of individual genes and clusters of co-expressed genes.

Genes with large associated damages in metabolism turn out to be essential or conditionally essential for *M. pneumoniae* (see Table 1), with a unique exception. We use a classification given in [6], where essentiality is defined according to the measured metabolic map and the definition of a minimal medium which allows *M. pneumoniae* to grow. Essential genes are those that are required for the survival

Table 2 Largest structural damages produced in metabolism by gene knockouts and correspondence with gene essentiality

Gene	Essentiality	Damage
mpn429	Yes	49
mpn606	Yes	32
mpn628	Yes	32
mpn017	Yes	25
mpn303	Yes	18
mpn062	*No*	17
mpn576	Cond	16

of the organism, while conditional means that essentiality depends on the media composition available (Table 2).

To detect functional clusters, we use three different strategies applied to a correlation matrix of dependencies between the expression level of pairs of genes in *M. pneumoniae*. We first consider clusters as defined in [3], where a technique of average distance hierarchical clustering (HC) is used and clusters are defined as groups of nodes which are close to each other. Alternatively, we apply a random walk based algorithm called Infomap (I), where groups comprise nodes among which information flows quickly and easily. And finally, we use the method of Recursive Percolation (RP), that identifies clusters as strongly interconnected groups of nodes.

We find that the three detection methods result in qualitatively similar power-law-like cluster size distributions, with most clusters having small size while some are relatively big. Interestingly, genes related to high damage spreading reactions are secluded into mono-component clusters. The fact that these genes appear isolated pinpoints them as potentially important metabolic regulator targets, since the alteration of only one gene may affect a large number of metabolic reactions.

Knockouts of co-expression clusters produce a damage on metabolic structure that increases with the number of affected metabolic and with the number of associated reactions (Fig. 2). We compare these results with those measured on randomized versions (DP) of the metabolic network of *M. pneumoniae*. As evidenced in Fig. 2, all cluster detection methods identify clusters that produce lower damages in the real metabolic network of *M. pneumoniae* as compared to the randomized network. This supports the idea that the regulatory machinery that controls the coupled-to-metabolism co-expression of genes has evolved towards robustness.

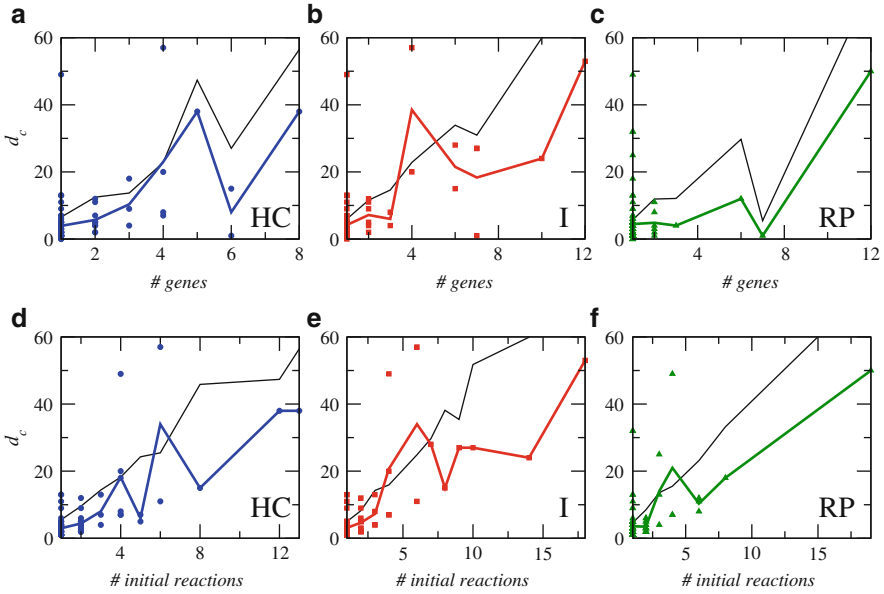

Fig. 2 Damages as a function of the number of metabolic genes and reaction failures in gene co-expression cluster knockouts (HC, I and RP). Results are compared with damages produced in randomized versions of the metabolic networks (DP)

3 Conclusions

Our results indicate that evolutionary pressure favors the ability of efficient metabolic regulation at the expense of robustness to reaction failures, pointing at the necessary integration of trade-offs from various cellular functions. On what respects to the analysis of gene knockouts, we observe that genes related to high-damage reactions are essential for the organism and that their expression tends to be isolated from that of other genes. This hints at the interplay between metabolism and genome, apparently evolved to favor the robustness of this organism by avoiding the potentially catastrophic effect of coupling the co-expression of structurally vulnerable metabolic genes.

References

1. G. Basler, O. Ebenhöh, J. Selbig, Z. Nikoloski, Mass-balanced randomization of metabolic networks. Bioinformatics **27**, 1397–1403 (2011)
2. G. Basler, S. Grimbs, O. Ebenhöh, J. Selbig, Z. Nikoloski, Evolutionary significance of metabolic network properties. J. R. Soc. Interface **9**, 1168–1176 (2012)

3. M. Güell et al., Transcriptome complexity in a genome-reduced bacterium. Science **326**, 1268–1271 (2009)
4. O. Güell, F. Sagués, G. Basler, Z. Nikoloski, M.A. Serrano, Assessing the significance of knockout cascades in metabolic networks. JCIS **3**, 45–53 (2012)
5. O. Güell, F. Sagués, M.A. Serrano, Predicting effects of structural stress in a genome-reduced model bacterial metabolism. Sci. Rep. **2**, 621 (2012)
6. E. Yus et al., Impact of genome reduction on bacterial metabolism and its regulation. Science **326**, 1263–1268 (2009)

Stochastic Amplification in Neural Networks

Jorge Hidalgo, Luís F. Seoane, Jesús M. Cortés, and Miguel A. Muñoz

The phenomenon of Stochastic Amplification comes out to describe the oscillations of a community of interacting individuals, as for example, the fluctuations of two species in a prey-predator system. It has been put forward in the context of Theoretical Ecology [7] and Epidemiology [1], giving a simple explanation to the temporal patterns found in nature. In a nutshell, the phenomenon operates as follow: when the system is poised nearby a stable fixed point of the dynamics, noise can amplify some specific frequencies and produce quasi-oscillations.

As in [4, 5], we examine the role of this phenomenon in brain dynamics. Deciphering the diverse patterns of global activity recorded in the brain and associating them with behavioural states are major challenges in Neuroscience [2]. High-frequency neural activity (10–100 Hz) has been related to a collection of cognitive tasks such as working memory [10] and selective attention [8]. On the other hand, slow waves (0.5–2 Hz) appear during the deepest stages of sleep, under anaesthesia or even during quiet wakefulness and might play an important role in neural plasticity and in the consolidation of new memories [9].

Specifically, we focus our study on the so-called up and down oscillations, in which a large fraction of neurons alternate between two different stable membrane-potential states: the down-state, with a very low activity, and the up-state, with high synaptic activity [12]. These waves appear in the low band ($\sim$1 Hz), and have been observed both in vivo and in vitro. Remarkably, recent experiments have analysed the fluctuations of the voltage in both up and down states, finding specific temporal patterns operating only in ups—in the form of a pronounced peak nearby 30 Hz in the power spectrum—but not in downs [3].

J. Hidalgo (✉) • L.F. Seoane • J.M. Cortés • M.A. Muñoz
Instituto de Física Teórica y Computacional Carlos I, Universidad de Granada, Granada, Spain
e-mail: jhidalgo@onsager.ugr.es; jcortes@decsai.ugr.es; mamunoz@onsager.ugr.es

Á. Corral et al. (eds.), *Extended Abstracts Spring 2013*, Trends in Mathematics 2,
DOI 10.1007/978-3-319-08138-0_9

Trying to give a qualitative and quantitative explanation to these findings, we employ minimalistic models able to generate up and down states. In this paper we restrict on the mean-field Tsodyks–Markram (TM) model of short-term synaptic plasticity (STSP) with two variables [6, 11]. A more realistic model based on the implementation of the TM model in a network of Integrate-and-Fire neurons is also studied in [4].

In the TM model, the mean voltage potential v evolves according to the amount of available resources u (neurotransmitters). The voltage grows owing to both external and internal inputs and decreases owing to leakage processes; synaptic resources are consumed in the process of generating internal outputs and spontaneously recover to a target maximum value, fixed here to $u = 1$,

$$\dot{u} = g_u(u, v) = \frac{1 - u}{\tau_R} - U_0 u f(v), \tag{1}$$

$$\dot{v} = g_v(u, v) = \frac{v_r - v}{\tau_L} + \mu u f(v) + I_0, \tag{2}$$

where τ_L and τ_R are the characteristic times of voltage-leakage and synaptic-recovery, respectively, v_r is the resting potential, μ takes account of the strength of the internal inputs, U_0 is the release probability of neurotransmitters, I_0 is the external input, and the firing rate function, $f(v)$, is assumed to be of the form $f(v) = \alpha(v - T)$ if $v \geq T$, where T is a threshold value, and $f(v) = 0$ otherwise.

For the chosen parameters (see Fig. 1), there are two stable fixed points. One of them corresponds to a sustained up-state, and the other to a down-state. This set of equations is deterministic. Then, following [6], we add noise to have into account some possible stochastic sources (such as irregular external inputs, finite size, or irregular and limited connectivity to name but a few). For simplicity, we add uncorrelated Gaussian white noises $\eta_u(t)$, $\eta_v(t)$ with respective variances σ_u, σ_v. However, our principal results do not depend crucially on this choice. When noise is switched on, the system becomes bistable and exhibits up and down oscillations.

To analyse the fluctuations around each of the stable fixed points, $\delta(u, v) = (u, v) - (u^*, v^*)$, we linearise Eqs. (1) and (2) to obtain

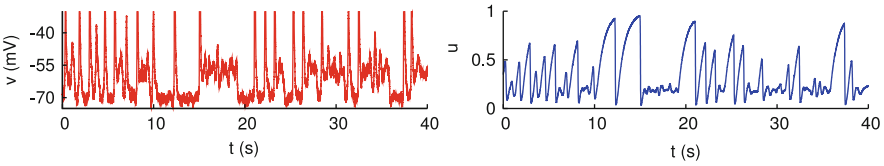

Fig. 1 Average potential (*left*) and synaptic utility (*right*) in computer simulations of the model of Markram and Tsodyks; the system exhibits up and down transitions in the presence of noise. Parameter values are: $\tau_L = 0.05\,\text{s}$, $\tau_R = 0.8\,\text{s}$, $v_r = -70\,\text{mV}$, $\omega = 12.6\,\text{mV/Hz}$, $u = 0.5$, $T = 2.0\,\text{mV}$, and $\alpha = 1.0\,\text{Hz/mV}$. Noise variance are $\sigma_v = 2.2\,\text{mV}/\sqrt{\tau}$, $\sigma_u = 0$. The time step is $10^{-4}\,\text{s}$

$$\dot{\delta u} = a_{uu}\delta u + a_{uv}\delta v, \tag{3}$$

$$\dot{\delta v} = a_{vu}\delta u + a_{vv}\delta v, \tag{4}$$

where $a_{zz'} = \frac{\partial g_z}{z'}(u^*, v^*)$ correspond to the elements of the Jacobian matrix evaluated at the fixed points, z and z' standing for either u and v. A standard lineal stability analysis for the used parameters reveals that the down-state has two real negative eigenvalues, while the up-state has two complex eigenvalues with negative real part.

Defining $\tilde{\delta} z(\omega) = \mathcal{F}[\delta z(t)]$ as the Fourier transform of the fluctuations of either u and v, it is straightforward to compute their power spectrum, $P_z(\omega) = \langle |z(\omega)|^2 \rangle$,

$$P_z(\omega) = \frac{\alpha_z + \sigma_z^2 \omega^2}{\left[\Omega^2 - \omega^2\right]^2 + \Gamma^2 \omega^2}, \tag{5}$$

where $\alpha_z = a_{zz'}^2 \sigma_{z'}^2 + a_{z'z'}^2 \sigma_z^2$ and $\sigma_z^2 = \langle \eta_z^2 \rangle$; while $\Omega^2 = \det(A)$ and $\Gamma = \mathrm{Tr}(A)$ do not depend on the noise amplitude. The resulting $P_v(\omega)$ is represented in Fig. 2.

In the limit of small noise amplitude, both spectra exhibit a maximum nearby the denominator minimum (assuming that the solution of the previous equation exists), specifically at

$$\omega_{\text{peak}} = \sqrt{\Omega^2 - \Gamma^2/2}. \tag{6}$$

Considering $\lambda_\pm$ the associate eigenvalues of the stability (Jacobian) matrix at a given stable fixed point, the condition for a non-trivial maximum to exist is

$$\mathrm{Im}(\lambda_\pm) > \mathrm{Re}(\lambda_\pm). \tag{7}$$

In other words, the stable fixed point has to be a *focus* with its respective complex eigenvalues. Having real eigenvalues or complex eigenvalues with a weak imaginary (oscillatory) part implies a negative argument of the square root of Eq. (6), and hence, no peaks appear.

The power spectrum of the fluctuations around each of the two (up and down) states is plotted in Fig. 2. Observe the presence of a non-trivial peak for the up-state spectrum, indicating the existence of noise-induced quasi-cycles. This is the so-called effect of *stochastic amplification of fluctuations*. The mechanism works as follows: the system tries to relax to the fixed point, but noise "kicks" it away, amplifying some frequencies which are closely related to that of the deterministic damped oscillations; the peak results to be slightly shifted from the damping frequency, which is $\omega_{\text{damping}} = \sqrt{\Omega^2 - \Gamma^2/4}$. On the other hand, if the system decays towards a deterministic node (i.e., with real eigenvalues), no frequencies are amplified whatsoever; see Fig. 2. This is what happens in the down-state, where the crossed coupling terms vanish when $f(v) = 0$, and then the stability matrix is already diagonalised after the linearization.

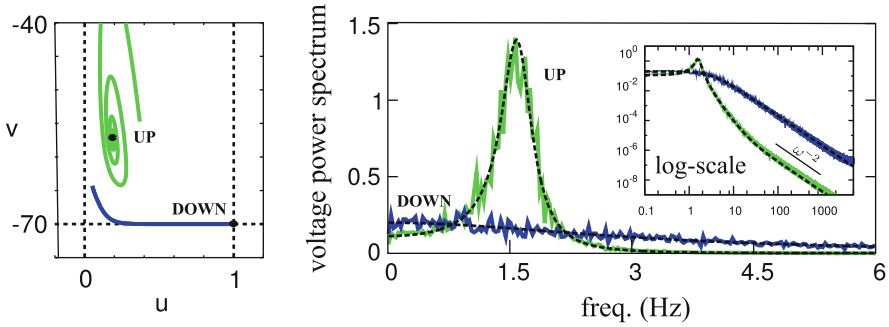

Fig. 2 *Right*: Power spectrum of fluctuations in up- and down-states for average membrane potential v. A marked peak appears for the up-state (*green curves*) near $\approx$1.5 Hz. Instead, there is no track of similar peaks for down states (*blue curves*). Observe the excellent agreement between simulation results (*noisy curves*) and analytical results (*black dashed lines*). The *inset* represents double-logarithmic plots of the same quantities as in the main plots. *Left*: deterministic trajectories for the model using different initial conditions. The up-state is a focus (complex eigenvalues), while the down-state is a node (real eigenvalues)

We have verified that the mechanism is robust against the incorporation of synaptic facilitation to the model [5]. Similarly, the same framework explains why (owing to the effective decoupling of equations) a similar resulting frequency cannot be observe in down states (in accordance with experiments).

These results agree qualitatively with experimental results (e.g., [3]). However, in order to improve the result for the characteristic frequency and obtain a result closer to the empirical values, more detailed models are required. This path has been followed in [4] where—by considering a simple network-version of the model above in which the role of individual neurons can be explicitly followed—we have shown that the peak frequency shifts towards empirically observed values.

Summing up, a simple deterministic model able to reproduce up and down states, does also include non-trivial oscillations within the up state but not in the down state when some noise source is switched on. The mechanism of stochastic amplification of fluctuations can explain the structure of the power spectra and other highly non-trivial features of cortical oscillations in a simple, elegant and parsimonious way.

References

1. D. Alonso, A.J. McKane, M. Pascual, Stochastic amplification in epidemics. J. R. Soc. Interface **4**, 575–582 (2007)
2. G. Buzsáki, *Rhythms of the Brain* (Oxford University Press, New York, 2006)
3. A. Compte et al., Spontaneous high-frequency (10–80 Hz) oscillations during up states in the cerebral cortex in vitro. J. Neurosci. **17**, 13828–13844 (2008)
4. J. Hidalgo, L.F. Seoane, J.M. Cortés, M.A. Muñoz, Stochastic amplification of fluctuations in cortical up-states. PloS one **7**, e40710 (2012)

5. J. Hidalgo, L. Seoane, J. Cortés, M. Muñoz, Does the phenomenon of stochastic amplification of fluctuations play a relevant role in cortical dynamics? in *AIP Conference Proceedings*, vol. 1510 (2013), p. 94
6. D. Holcman, M. Tsodyks, The emergence of up and down states in cortical networks. PLoS Comput. Biol. **2**, e23 (2006)
7. A.J. McKane, T.J. Newman, Predator-prey cycles from resonant amplification of demographic stochasticity. Phys. Rev. Lett. **94**, 218102 (2005)
8. P.N. Steinmetz et al., Attention modulates synchronized neuronal firing in primate somatosensory cortex. Nature **404**, 187–190 (2000)
9. R. Stickgold, Sleep-dependent memory consolidation. Nature **437**, 1272–1278 (2005)
10. C. Tallon-Baudry, O. Bertrand, F. Peronnet, J. Pernier, Induced gamma-band activity during the delay of a visual short-term memory task in humans. J. Neurosci. **18**, 4244–4254 (1998)
11. M.V. Tsodyks, H. Markram, The neural code between neocortical pyramidal neurons depends on neurotransmitter release probability. Proc. Natl. Acad. Sci. U.S.A. **94**, 719–723 (1997)
12. R. Yuste, J.N. MacLean, J. Smith, A. Lansner, The cortex as a central pattern generator. Nat. Rev. Neurosci. **6**, 477–483 (2005)

Evolutionary Dynamics of the Genotype-Phenotype Map

Esther Ibáñez-Marcelo and Tomás Alarcón

1 Introduction

Our aim is to study the evolutionary properties of a model of the genotype-phenotype. The relation between genotype and phenotype is very complicated. Such complexity is a consequence of the fact that the phenotype emerges from networks of interactions between genes and their products, which regulate gene expression and give rise to non-linear, high-dimensional dynamical systems. In addition, these gene regulatory networks (GRNs) are shaped by evolution by natural selection. As a consequence, the genotype-phenotype map exhibits a number of features: the map is not a one-to-one map (many genotypes produce the same phenotype), robustness, evolvability and convergence, among others [2, 3].

We focus here in the characterisation of the genotype-phenotype map as a bipartite graph. We define the phenotype as the attractors of the dynamics of the gene regulatory network. Moreover, a bipartite network has been introduced to study genotype-phenotype relation (genotype-phenotype space) and their structural relationship. We also define some emergent biological properties such as robustness, evolvability, canalisation and convergence in terms of network or graph-theoretical properties such as the clustering coefficient and resilience of the giant connected component (percolation).

E. Ibáñez-Marcelo (✉) • T. Alarcón
Centre de Recerca Matemàtica, Barcelona, Catalonia, Spain
e-mail: eibanez@crm.cat; talarcon@crm.cat

Á. Corral et al. (eds.), *Extended Abstracts Spring 2013*, Trends in Mathematics 2,
DOI 10.1007/978-3-319-08138-0_10

2 Network Representation of Properties of the Genotype-Phenotype Map

The four emergent properties of the genotype-phenotype map that we are going to focus on are: Robustness, evolvability, canalisation and convergence. For each one of these properties, we propose a metric in terms of properties of the (bipartite) genotype-phenotype network and analyse their evolutionary dynamics.

Robustness, which measures phenotypic resilience to gene mutations and evolvability, i.e., the ability of the system to innovate, can be considered to be opposites: whereas robustness is related to the ability of maintaining biological identity, *evolvability* measures the capability to change and adapt to varying conditions. The question arises as to whether these two concepts co-evolve. The quantitative analysis of these properties is associated with the a generalisation of the concept of neutral network which consists of a network where all genotypes (nodes) carrying the same phenotype connected by an edge if only if they differ by one gene mutation alone. We further add a second type of nodes, the phenotypes. Links are established between phenotypes and those genotypes that belong to the basin of attraction of the former.

We propose the clustering coefficient within the bipartite network to quantify phenotypic robustness, remember that the clustering coefficient for a (phenotype) node u is

$$c_u = \frac{2T(u)}{\deg(u)(\deg(u)-1)},$$

where $T(u)$ is the number of triangles through phenotype u and $\deg(u)$ is the degree of u, i.e., the number of genotypes belonging to the basin of attraction. c_u is a measure of robustness of u since it quantifies how many genotypes connected by single-mutation events exhibit the same phenotype.

Evolvability is measured in terms of metrics related to percolation, i.e., the existence of a giant connected component and its resilience against attacks (i.e., removal of nodes). Since evolvability is defined as the ability of an organism to adapt to changing conditions by modifying its phenotype, it is natural to define evolvability in terms of global connectivity and navigability of the genotype-phenotype space.

Canalisation is a term coined by Conrad Waddington and it can be defined as the tendency of phenotypes to increase robustness as time progresses or, as Waddington referred to it *buffering of the genotype* [5]. We will therefore quantify it in terms of the time evolution of the average clustering coefficient. *Convergence*, on the other hand, refers to the phenomenon whereby different species of disparate lineages evolve to acquire similar biological traits (phenotypes).

In order to analyse convergence in our model, we calculate the Hamming distance between genotypes linked to the same phenotype. The *Hamming distance* between genotypes (g_1, g_2) is measured as the number of mutations between two genotypes,

$d(g_1, g_2)$. Each phenotype has associated an average Hamming distance defined as the mean Hamming distance between every possible pair of genotypes connected to it.

3 The Model

In order to study the evolutionary dynamics of the genotype-phenotype map, we consider a multi-scale population dynamics model for a cell population where we consider two levels or scales:

Microscopic scale. It accounts for the intracellular dynamics of each cell, where we consider that each cell individual is characterised by a pair $(G, g(0))$, where G is a matrix accounting for the GRN (i.e., how a gene product affects the activation of all other genes), and $g(0)$ corresponds to the initial condition which can be interpreted as the heritable developmental program. The GRN defines a dynamical system such that, with $g(0)$ as an initial condition, and according to the rules (1), can either reach a fixed point or a periodic steady state,

$$I_i = \sum_{\langle j \rangle_i^{\text{in}}} G_{ji} g_j, \tag{1}$$

where $\langle j \rangle_i^{\text{in}}$ is the set of *in-neighbours* of i, and

$$\begin{cases} g_i(t+1) = 1, & \text{if } I_i(t) \geq 0 \\ g_i(t+1) = -1, & \text{if } I_i(t) < 0. \end{cases}$$

The corresponding steady state $g(\infty)$ is our representation of the phenotype. Viability conditions are introduced that deem as lethal genotypes that induce oscillations with long cycles [4]. Thus, the intracellular dynamics of each cell determines whether the cell survives and, if it does, what its phenotype is.

Macroscopic scale. In order to obtain our evolving bipartite genotypes-phenotypes graph, we prescribe a population dynamics consists of a multi-type Wright–Fisher model with mutation [1]. In our case, each type corresponds to a genotype: when proliferation is attempted a mutation (consisting in changing the sign of a randomly chosen non-zero entry of the matrix G, leading to G') occurs with probability p_{mut}. Then, we run the intracellular dynamics as per the microscopic scale. If the corresponding phenotype is viable, two descendants are added to the population with genotype $(G', g(0))$ and the corresponding phenotype. If the mutation leads to a non-viable phenotype on a previously viable individual, this is eliminated from the population and we go through another Wright–Fisher step. From this process the bipartite graph is constructed as the population dynamics proceeds. Every time a new genotype is generated by mutation a genotype node is added to the network, as well as the corresponding edges, and the same occurs

with the phenotypes. Finally, the pseudo-bipartite graph have two types of nodes: genotype nodes and phenotype nodes, and their corresponding two kinds of edges: edges between genotypes if the distance is 1, edges between genotype to the phenotype associated to it.

4 Results and Conclusions

After studying the properties described in the previous section, we have ran numerical simulations of our model and found the following results. When we analyse the phenotypic clustering coefficient, we observe that there is a strong inverse correlation between clustering coefficient and phenotype degrees, as shown in Fig. 1a. This implies the existence of, essentially, two kinds of phenotypes: (i) phenotypes with a big basin of attraction (high degree) but little robustness, and (ii) robust phenotypes (high clustering) but with low degree.

Also, we observe co-evolution of canalisation and evolvability: as time progresses, both the average clustering coefficient increases (see Fig. 1b), and a giant connected component emerges as shown in Fig. 2a.

Another, interesting result concerns the correlation between the average Hamming distance between genotypes associated with a phenotype and the clustering coefficient (robustness) of the latter. We observe that convergence occurs in non-robust phenotypes (see Fig. 3): Average Hamming distance is systematically bigger for phenotypes with low clustering coefficient (low robustness).

Finally, another result concerns the influence of the GRN parameters in the structure of the bipartite graph. For example, Fig. 2b shows how microscopic parameters such as the rewiring probability and the viability conditions affects the resilience of the giant connected component, and therefore, the evolvability of the system.

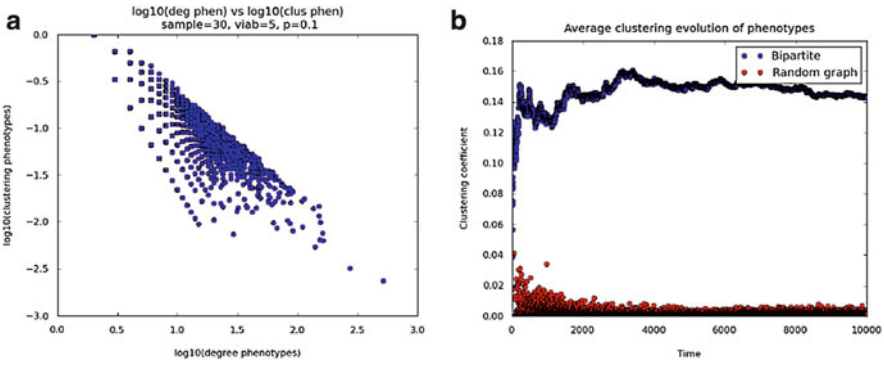

Fig. 1 (**a**) Strong inverse relation between phenotype clustering coefficients and phenotype degrees. (**b**) Time evolution of the average clustering

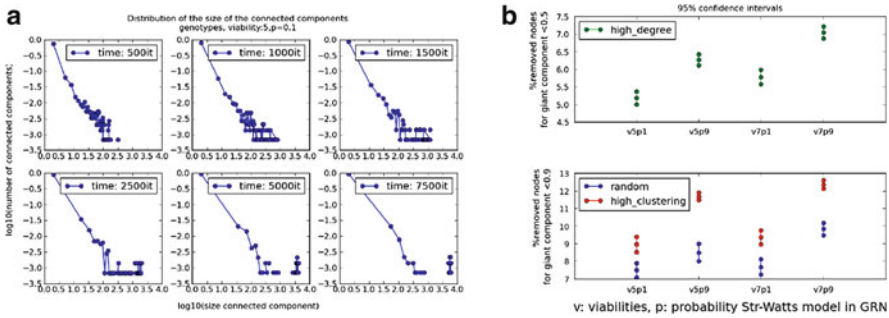

Fig. 2 (**a**) Simulation results for the size distribution of connected components as a function of time. We observe that, as time progresses, a macroscopic proportion of nodes accumulate in a few components which eventually leads to the formation of a giant connected component. (**b**) How the microscopic parameters, i.e., those related to determining the structure of the GRN and its viability, affect the resilience of the giant connected component and can be thus used to control evolvability of the system

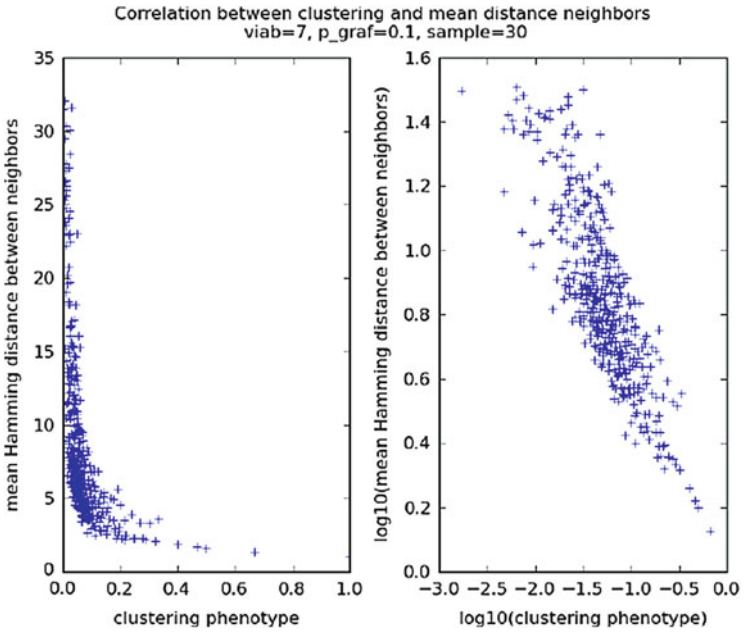

Fig. 3 Relation between Hamming distance and clustering coefficient. *Left*: clustering vs Hamming distance. *Right*: log(clustering) vs log(Hamming distance)

References

1. R.A. Blythe, A.J. McKane, Stochastic models of evolution in genetics, ecology and linguistics. J. Stat. Mech. Theory Exp. **2007**, 07018 (2007)
2. S. Ciliberti, O.C. Martin, A. Wagner, Robustness can evolve gradually in complex regulatory gene networks with varying topology. PLoS Comput. Biol. **3**, 164–173 (2007)
3. C. Espinosa-Soto, O. Martin, A. Wagner, Phenotypic robustness can increase phenotypic variability after non-genetic perturbations in gene regulatory circuits. J. Evol. Biol. **24**, 1284–1297 (2011)
4. M.L. Siegal, A. Bergman, Waddington's canalisation revisited: developmental stability and evolution. PNAS **99**, 10528–10532 (2002)
5. C.H. Waddington, Canalization of development and the inheritance of acquired characters. Nature **150**(3811), 563–565 (1942)

Spatio-Temporal Patterns in a Large-Scale Discrete-Time Neuron Network

Oleg V. Maslennikov* **and Vladimir I. Nekorkin***

1 Introduction

The formation of spatio-temporal patterns is one of the most important forms of collective electrical activity of neural networks. Such forms of activity have been detected experimentally in different neural structures, including the structures in visual [4] and somatosensory [11] cortex, in the temporal lobe [7], in the inferior olives [5], etc. Modeling of the network structure and dynamics can be a possible way of identifying mechanisms of the pattern appearance and disappearance in such large-scale systems. Here we show some results of modeling the olivo-cerebellar system (OCS), which is a special part of brain in vertebrates (for more details, see [8]). A large number of experimental data indicate the important role of this system in the control of motor systems, adaptation under varied external conditions, and motor learning [3, 10].

Neurons of the OCS are combined into highly ordered groups, each playing its own functional role in the formation and destruction of the motor patterns [6]. Our model consists of three layers (Fig. 1) of units each described by the same nonlinear map [1, 9] with different parameter values. The first one is the layer of inferior olive (IO) neurons, which we will call the main layer, since its dynamics is the output of our model. The second layer consists of Purkinje cells (PC). The third layer comprises the cerebellar nuclei (CN) neurons. The neighboring elements of the main layer are coupled with each other via electrical synapses with changeable strength. Each IO neuron with indexes i, j has an axon (climbing fiber) branching in two;

*This work was supported by MESRF (14.132.21.1354) and RFBR (12-02-31252).

O.V. Maslennikov (✉) • V.I. Nekorkin
Institute of Applied Physics of the Russian Academy of Sciences, Nizhny Novgorod, Russia
e-mail: olmaov@neuron.appl.sci-nnov.ru

Á. Corral et al. (eds.), *Extended Abstracts Spring 2013*, Trends in Mathematics 2,
DOI 10.1007/978-3-319-08138-0_11

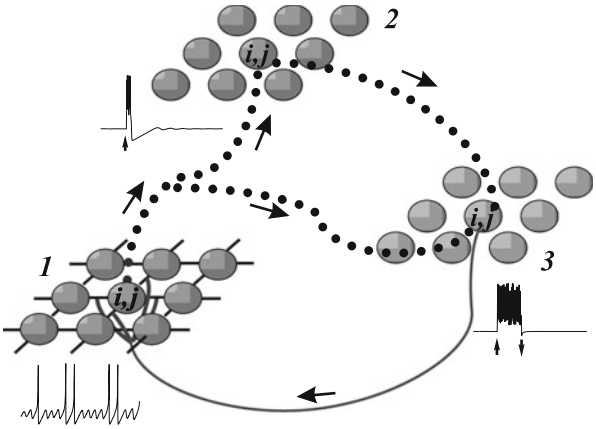

Fig. 1 Schematic structure of the OCS model. Examples for the individual element waveforms of corresponding layers are shown

see Fig. 1. Both axonal branches (collaterals) terminate with excitatory synapses, one on a PC with the number (i, j) and another on the CN neuron (i, j). Each PC (i, j) has an axon ending with an inhibitory synapse on the corresponding CN neuron with indexes (i, j). Thus, each CN neuron receives signals of different types via its synaptic inputs, namely, excitatory from the IO neurons and inhibitory from the PC. In turn, each CN neuron (i, j) has an axon with inhibitory synaptic terminals which suppress the electrical couplings of the corresponding IO neuron (i, j) with the neighboring elements of the main layer, i.e., with the neurons $(i - 1, j)$, $(i + 1, j)$, $(i, j - 1)$, and $(i, j + 1)$.

In what follows we briefly discuss some dynamical properties of the elements and their collective activity. We present the main results of numerical simulations of the proposed discrete-time model and associate them with the real prototype.

2 Individual Dynamics

IO. There are some exclusive dynamical properties of IO neurons important for the whole OCS functioning [2, 6]. Firstly, in a resting state these cells generate (subthreshold) quasi-sinusoidal oscillations with a small amplitude and frequency about 10 Hz. The action potential is generated at the peak of these oscillations once the membrane potential reaches some threshold value. Secondly, IO neurons interact with each other via electrical synapses (gap junctions), and their strength is controlled by the CN activity. One of the key IO properties reproduced in our model is its ability to switch from the subthreshold oscillation mode to the action potential generation mode on the oscillation peaks during the action of varying synaptic current; see Fig. 1, waveform for layer 1.

PC and CN. In accordance with our scheme of the OCS, PC and CN neurons are the elements of the second and third layers, respectively. When modeling these cells, we took into account their key properties which give the main contribution to the operation of the OCS. Elements of the second layer (PC) are excitable units, which generate bursts of spikes during the excitation. Elements of the third layer (CN) turn into the active spiking state during excitation via the synaptic terminal of the corresponding collaterals of the IO-axons and come back to the resting state during inhibition by the synaptic terminals of the PC-axon.

Axons. Axons (nerve fibers) are represented in our model by chains of elements coupled electrically with the nearest neighbors. Each element is excitable, i.e., generates an action potential during stimulation. Successive excitation of the neighboring elements of the chain models the propagation of a pulse along the nerve fiber.

Dynamic coupling between IO neurons. IO neurons interact via gap junctions, or electrical synapses, the strength of which is controlled by the synapses of the CN-axons. This control is inhibitory: in the absence of control pulses, the coupling strength is equal to some positive value, which results in synchronization of subthreshold oscillations of the interacting IO neurons. On the contrary, the coupling is suppressed and the electrical coupling between neurons breaks if the signal is fed.

3 Qualitative Description of the Model Dynamics

Let us assume the membrane potential of an IO neuron has reached a threshold value at some instant of time. This results in the action potential excitation in the neural axon. Propagating along both branches of the climbing fiber, this spike evokes the PC and CN activity. A burst is generated in the PC and a long sequence of action potentials is excited in the CN neuron. The PC burst causes the inhibitory action potential to propagate through the PC-axon to the CN neuron. A long spike series in the latter is interrupted due to the inhibition by the action potential coming from the PC. A burst of spikes transmitted through the CN-axon to synaptic couplings of the corresponding IO neuron leads to the suppression of the latter. Thus, synaptic couplings of the IO neuron with the neighboring elements of the main layer break for a time equal to the duration of the CN-burst.

4 Spontaneous Patterns in the OCS

The pattern formation in the IO layer is controlled primarily by the maximum strength of coupling between the IO neurons and by duration of the break of synaptic couplings between them. In our model, the latter is controlled by the length of the PC-axons. Figure 2a, c shows snapshots of the IO-activity for two

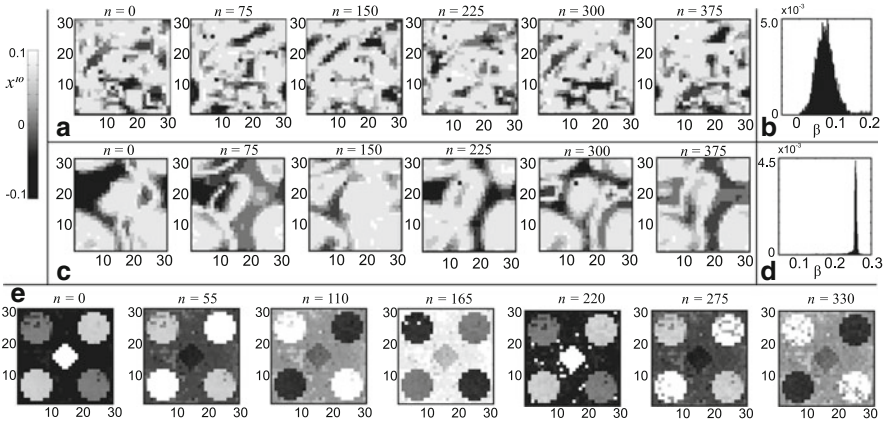

Fig. 2 Pattern dynamics of the 30 × 30 IO-layer for (**a**) small and (**c**) large coupling strength. (**b**, **d**) Histograms of the corresponding Markov parameter. (**e**) Stimulated pattern dynamics

different values of the maximum coupling strength. It is seen that for a small coupling value, the size of patterns is also small (see Fig. 2a), and the characteristic time for their spatial position to change is equal approximately to the oscillation period. In case with a larger value of the maximum coupling strength (Fig. 2c), the pattern size increases on the average, and their spatial position remains constant during several oscillation periods. These qualitative results are confirmed by the quantitative analysis of the Markov parameter β [5] for the IO-layer. The more the absolute value of β is different from zero, the higher the level of spatial order of the layer. This means that if the membrane potentials of IO-elements are randomly distributed, then β tends to zero. The case is opposite when the membrane potentials are the same for all elements, i.e., all the IO-elements form one single pattern. Then β takes its maximum value. The more β is different from zero, the larger the characteristic pattern size. Figure 2b, d shows β-histograms for two values of the coupling strength. It is seen that for a small strength, β varies over relatively wide limits, but its absolute values are close to zero; see Fig. 2b. For a larger strength, the mean value of β increases and its variance decreases; see Fig. 2d. This result is in good agreement with the experimental measurements of the Markov parameter for different levels of blocking the electrical coupling between the inferior olive neurons. For a weak coupling between neurons, the layer is divided into a set of small patterns, whose structure changes drastically with time. As the coupling is enhanced, the patterns increase in size and the spatial configuration is preserved in time.

5 Stimulated Patterns

For a motor control, the OCS generates and preserves in time the spatio-temporal patterns, and changes them depending on the input signals. According to these signals, sub-groups of inferior olive neurons with synchronous or phase-shifted oscillations are formed, and this spatial structure is maintained for several oscillation periods. When a new pattern comes, oscillations of the elements are rearranged in accordance with it. Such behavior of the system is the basis for control of the motor function of the body [6].

Figure 2e shows the pattern dynamics of the IO neurons in our model. Initially, variables of IO-units were randomly chosen. Then an external stimulus in the form of a spatial pattern is fed to the layer. As an example, this pattern is taken in the form of five circles. The stimuli acting on all the IO-elements have the same amplitude and duration. The difference is that the stimulation acts on the different circles in different instants of time, thereby creating a phase shift of oscillatory activity between different circles. Since the spikes are generated at the peaks of subthreshold oscillations, the phase shift of them corresponds one-to-one to the phase shift of the action potentials transmitted into the climbing fiber and then to the PC and CN neurons.

6 Conclusion

In conclusion, we developed a model of a very complex neural structure, the OCS, using the same map [9] as a basic unit. In our discrete-time model three layers of neurons interact with each other through axonal connections, and the propagation of nerve impulses along the axons is modeled by the chains of excitable elements. Dynamic properties of individual elements are examined, and the parameters are found corresponding to the dynamics adequate to the biological prototypes. A model of dynamic coupling between the IO neurons is proposed and the pattern formation processes in the layer they form are explored. The relation between the size of spatio-temporal patterns and the maximum coupling is established. It is shown that stimulated patterns of a certain configuration can be formed in the system and can be reset by an external stimulus. The latter property underlies the neuronal systems of the motor function control.

References

1. M. Courbage, V.I. Nekorkin, L.V. Vdovin, Chaos **17**, 043109 (2007)
2. G.A. Jacobson, I. Lev, Y. Yarom, D. Cohen, PNAS **106**(9), 3, 579 (2009)
3. E.R. Kandel, J.H. Schwartz, T.M. Jessel, *Principles of Neural Science* (McGraw-Hill, New York, 2000)

4. P. König, A.K. Engel, W. Singer, PNAS **92**(1), 290 (1995)
5. E. Leznik, V. Makarenko, R. Llinas, J. Neurosci. **22**(7), 2, 804 (2002)
6. R. Llinás, E.J. Lang, J.P. Welsh, The cerebellum, LTD, and memory: alternative views. Learn. Mem. **3**, 445–455 (1997)
7. J.-R. Manning, S.M. Polyn, G.H. Baltuch et al., PNAS **108**(31), 12893 (2011)
8. O.V. Maslennikov, V.I. Nekorkin, Radiophys. Quantum Electron. **55**(3), 198–214 (2012)
9. V.I. Nekorkin, L.V. Vdovin, Izvest. vys. ucheb. zaved. Prikladnaya nelineynaya dinamika (in Russian) **15**(5), 36–60 (2007)
10. J.G. Nicholls, R.A. Martin, P.A. Fuchs, J.W. Moore, A.E. Stuart, *From Neuron to Brain*, vol. 5 (Sinauer Associates, Sunderland, 2011)
11. J.-W. Yang, I.L. Hanganu-Opatz, J.-J. Sun, H.J. Luhmann, J. Neurosci. **29**(28), 9011 (2009)

A Cavity Method Approach to DNA Stretching

Francesco A. Massucci*, **Isaac Pérez Castillo***, **and Conrad Pérez Vicente***

1 Introduction

Single molecule manipulation experiments are becoming increasingly important, for they aim at understanding the mechanical properties of molecules such as nucleic acids and proteins. Here, in particular, we are interested in DNA stretching experiments [13]. We present a model that reproduces the main features observed when pulling DNA, namely the elastic elongation at small forces, the resistance to bending and the enthalpic response to strong stretching forces [1, 5]. We also study the overstretching transition of B–DNA (i.e., the DNA in its double helical configuration) into S–DNA[1] observed at around 65 pN, when the molecule reaches an extension of about 1.7 times its natural length [2, 12]. Our aim is to improve upon the phenomenological models in literature [1, 6, 7] by revisiting the Discrete

*The authors would like to thank Felix Ritort, Joan Camunas and Josep Maria Huguet for providing the experimental measurements carried out at the *Small Biosystems lab* in Barcelona and for discussions.

[1]Such transition, after years of debate [3, 8, 11, 15, 16], seem to have found recently a coherent explanation that links the formation of S–DNA to the experimental setup [4].

F.A. Massucci (✉)
Departament d'Enginyeria Química, Universitat Rovira i Virgili, Tarragona, Catalonia, Spain
e-mail: francesco.massucci@urv.cat

I.P. Castillo
Department of Mathematics, King's College, London, UK
e-mail: isaac.perez_castillo@kcl.ac.uk

C.P. Vicente
Departament de Física Fonamental, Universitat de Barcelona, Barcelona, Catalonia, Spain
e-mail: conrad@ffn.ub.es

Á. Corral et al. (eds.), *Extended Abstracts Spring 2013*, Trends in Mathematics 2,
DOI 10.1007/978-3-319-08138-0_12

Persistent Chain (DPC) [14], a model featuring both the coarse-grained nature of real molecules and the bending stiffness observed in the experiments. We solve the problem analytically with the cavity method and fit it to experimental measurement, without making any approximation.

2 The Model

In the DPC model [14, 17] the single stranded DNA is considered as a chain of N interacting monomers with Hamiltonian

$$-\beta H(\hat{\boldsymbol{t}}) = f b_B \sum_{i=1}^{N} \hat{t}_i \cdot \hat{z} + J_B \sum_{i=1}^{N-1} \hat{t}_i \cdot \hat{t}_{i+1}, \tag{1}$$

where $\hat{\boldsymbol{t}} = \left(\hat{t}_1, \ldots, \hat{t}_N\right)$, f is the stretching force, b_B the monomer length and J_B the interaction between the monomers, which modulates the bending stiffness of the chain. Vector $\hat{z}$ points to the direction of the stretching force, while each $\{\hat{t}_i\}_{i=1}^{N}$ points to the direction in space of monomer i. Both $\hat{z}$ and $\hat{t}_i$ are unitary vectors.

The preceding model can be extended so as to capture the behaviour of double stranded B-DNA and to reproduce its well known overstretching transition [2, 12]. We thus modify the Hamiltonian (1) and we allow the monomers to be into two possible states: native B-DNA and denatured S-DNA [14]. This yields the following Hamiltonian

$$-\beta H\left(\boldsymbol{t}, \boldsymbol{\sigma}\right) = f \sum_{i=1}^{N} b_{\sigma_i} \hat{t}_i \cdot \hat{z} + \gamma_B \sum_{i=1}^{N} \delta_{\sigma_i, B} + \sum_{i=1}^{N-1} \left(J_{\sigma_i, \sigma_{i+1}} \hat{t}_i \cdot \hat{t}_{i+1} + \epsilon_{\sigma_i, \sigma_{i+1}}\right), \tag{2}$$

where $\sigma_i \in \{B, S\}$ is the state of monomer i. Here b_σ is the monomer's length in state σ and $J_{\sigma,\sigma'} (= J_{\sigma',\sigma})$ the interaction between two neighbouring monomers in states σ and σ'. In what follows we assume $\epsilon_{\sigma\sigma} = 0$ and denote $J_\sigma = J_{\sigma\sigma}$. As the fundamental blocs of real DNA are extensible themselves, the stretched DNA is longer than its contour length. To consider this we introduce a *stretching modulus* and rewrite the native monomer length as $b_B = b_B^{(0)}\left(1 + f/Y\right)$, with Y the Young modulus. The elongation of the molecule reads for model (1) and (2), respectively,

$$L\left(f; \boldsymbol{\mu}\right) = \frac{c_B}{N} \sum_{i=1}^{N} \left\langle \hat{t}_i \cdot \hat{z} \right\rangle, \quad L\left(f; \boldsymbol{\mu}\right) = \frac{c_B}{N} \sum_{i=1}^{N} \delta_{\sigma_i, B} \left\langle \hat{t}_i \cdot \hat{z} \right\rangle + \frac{b_S}{N} \sum_{i=1}^{N} \delta_{\sigma_i, S} \left\langle \hat{t}_i \cdot \hat{z} \right\rangle. \tag{3}$$

Here $c_B = b_B^{(0)}\left(1 + 2f/Y\right)$, $\langle \cdots \rangle$ is the usual thermal average, and $\boldsymbol{\mu}$ are the parameters of model (1) and (2), respectively.

2.1 Fit Procedure

Both in the case of ss-DNA and ds-DNA one aims to fit the model to some experimental measurements. These consist in a set $\mathcal{S}^{\exp} := \{(f_a^{(\exp)}, L_a^{(\exp)})\}_{a=1}^{\mathcal{N}}$ of $\mathcal{N}$ points expressing force $f^{(\exp)}$ and polymer elongation $L^{(\exp)}$. Therefore given $\mathcal{S}^{\exp}$ one wants to find the best value of the model parameters by minimizing the square distance χ^2 between the model predictions and the measurements. Minimisation of χ^2 implies the calculation of L and of its derivatives with respect to the parameters, which, in turn, are simply correlation functions. For the ss-DNA model, for instance, one needs ultimately to compute the following correlation functions

$$\frac{\partial L}{\partial J_B} = \frac{c_B}{N} \sum_{i=1}^{N} \sum_{k=1}^{N-1} \left\langle \left(\hat{t}_i \cdot \hat{z}\right) \left(\hat{t}_k \cdot \hat{t}_{k+1}\right) \right\rangle_c , \qquad \frac{\partial L}{\partial b_B} = \frac{f c_B}{N} \sum_{i,k=1}^{N} \left\langle \left(\hat{t}_i \cdot \hat{z}\right) \left(\hat{t}_k \cdot \hat{z}\right) \right\rangle_c , \tag{4}$$

where $\langle \cdots \rangle_c$ denotes connected correlation in the thermal average. Thus, in order to minimise efficiently the function χ^2, we need to find a way to deal with the thermal average appearing in Eqs. (3) and (4). Luckily, a simple set of equations can be found to perform those thermal averages efficiently.

3 Analytical Solution with Cavity Method

We propose here to use the cavity method [9] to write exact solutions for the constrained local partition function, the molecular elongation and the correlations involved in the minimisation of χ^2. Let us explain the method briefly in the case of ss-DNA. We start by making the only basic assumption that the chain is very long, so that boundary effects are negligible. We then consider a monomer at site 0 in the bulk and observe that the Hamiltonian (1) can be written as $H(\hat{\boldsymbol{t}}) = H_0(\hat{\boldsymbol{t}}) + H^{(0)}(\hat{\boldsymbol{t}})$, where $H^{(0)}$ does not depend on site 0. We define $Q(\hat{\boldsymbol{t}}_{\partial 0})$ as the trace of the Boltzmann weight $e^{-\beta H^{(0)}(\hat{\boldsymbol{t}})}$ over all $\hat{\boldsymbol{t}}$ except 0 and its neighbourhood $\partial 0$, and build the constrained partition function

$$Z\left(\hat{t}_0\right) = e^{f b_B \hat{t}_0 \cdot \hat{z}} \int_{S^2} \mathrm{d}^2 \hat{\boldsymbol{t}}_{\partial 0} e^{J_B \hat{t}_0 \cdot \sum_{i \in \partial 0} \hat{t}_i} Q(\hat{\boldsymbol{t}}_{\partial 0}). \tag{5}$$

When variables $\hat{\boldsymbol{t}}_{\partial 0}$ are correlated only through site 0, i.e., for open chains, or for very long closed ones, one has $Q(\hat{\boldsymbol{t}}_{\partial 0}) = \prod_{i \in \partial 0} Q(\hat{t}_i)$. This allows us to write the following expressions for the partition function $Z\left(\hat{t}\right)$ in terms of its cavity counterpart $Q\left(\hat{t}\right)$, viz:

$$
\begin{aligned}
Q\left(\hat{t}\right) &= e^{fb_B\hat{t}\cdot\hat{z}} \int_{S^2} \mathrm{d}^2\hat{u}\; e^{J_B\hat{t}\cdot\hat{u}} Q\left(\hat{u}\right), \\
Z\left(\hat{t}\right) &= e^{fb_B\hat{t}\cdot\hat{z}} \left(\int_{S^2} \mathrm{d}^2\hat{u}\; e^{J_B\hat{t}\cdot\hat{u}} Q\left(\hat{u}\right) \right)^2 .
\end{aligned}
\tag{6}
$$

The expression (3) for the elongation $L(f)$ simply becomes

$$
L\left(f\right) = c_B \int_{S^2} \mathrm{d}^2\hat{t}\; P\left(\hat{t}\right)\left(\hat{t}\cdot\hat{z}\right), \tag{7}
$$

where $P\left(\hat{t}\right) = Z\left(\hat{t}\right)/Z$ and Z is a normalisation constant. A solution of $Q\left(\hat{t}\right)$ can be found iteratively, so that once $Q\left(\hat{t}\right)$ is known, we can calculate $Z\left(\hat{t}\right)$ and $L(f)$ by using Eqs. (6) and (7), respectively. At the same time we can compute the correlation functions (4) involved in the fit procedure by evaluating the derivatives $\partial_{J_B,b_B} Q\left(\hat{t}\right)$.

The model (2) for ds-DNA can be solved similarly by using the cavity method. Although the procedure is slightly more involved, as one has the continuous variables $\hat{\boldsymbol{t}}$ and discrete ones $\boldsymbol{\sigma}$, it is still possible to follow a similar path. Once again, the key quantity one needs to compute is the cavity constrained partition function

$$
Q_\sigma\left(\hat{t}\right) = e^{\gamma_B\delta_{\sigma,B} + fb_\sigma\hat{t}\cdot\hat{z}} \sum_{\tau\in\{B,S\}} e^{\varepsilon_{\sigma\tau}} \int_{S^2} \mathrm{d}^2\hat{u}\; e^{J_{\sigma\tau}\hat{t}\cdot\hat{u}} Q_\tau\left(\hat{u}\right) \tag{8}
$$

and its derivatives with respect to the parameters. This allows in turn to estimate $L\left(f\right)$ and its gradient so as to minimize the function χ^2.

3.1 Fit to Experimental Measurements

We first fit model (1) to experimental measurements of ss-DNA stretching. Since forces are below 40 pN, the monomers remain rigid and we keep $Y^{-1} \equiv 0$, reducing the number of fitting parameters. The fit, shown in Fig. 1a with Monte Carlo simulations [10], closely agrees with the experiments. The values of the parameters are reported in the caption of Fig. 1. We interestingly find that the model's monomer length corresponds to the actual DNA base distance measured by X-Ray diffraction. We are therefore able to capture the real scaling of the molecule's monomers by solving the problem analytically.

We then proceed to fit model (2) to ds-DNA stretching measurements. Figure 1b shows the very good agreement between the measurements and the fitted model. The value of the parameters returned by the fit is reported in the caption of Fig. 1. We find in this case a native monomer length which is of the order of 10 bases, which curiously corresponds to the DNA helix period. The length b_S is 1.75 times bigger

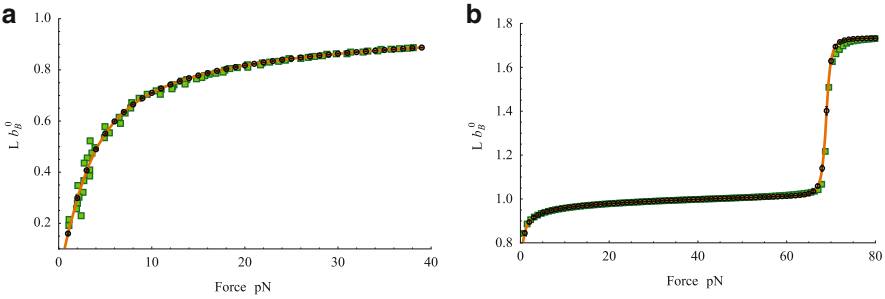

Fig. 1 Fits of the model (*solid line*) to experimental measurements (*full squares*) together with Monte Carlo simulations (*open circles*). *Left*: Fit of ss-DNA stretching measurements. Experimental data is reported in *full squares*, theoretical solution in straight line while *open circles* are Monte Carlo simulations. Values of the fit: $b_B^{(0)} = 0.63\,\text{nm}$, $J_B = 7.68\,\text{pN nm}$, $\chi^2 = 1.3 \times 10^{-4}$. *Right*: Fit of ds-DNA stretching measurements.The data shows the typical behavior of ds-DNA stretched by high forces, the double plateau and the jump around 65 pN are easily recognizable. Values of the fit: $b_B^{(0)} = 3.22\,\text{nm}$, $b_S = 5.63\,\text{nm}$, $Y = 4570.38\,\text{pN}$, $J_B = 56.26\,\text{pN nm}$, $J_{BS} = 26.35\,\text{pN nm}$, $J_S = 0.81\,\text{pN nm}$, $\gamma_B = 106.61\,\text{pN nm}$, $\epsilon_{BS} = 2.75\,\text{pN nm}$, $\chi^2 = 9 \times 10^{-5}$. In both fits we assume room temperature $k_B T = 4.04738\,\text{pN nm}$

than the native one, giving back the known ratio between S-DNA and B-DNA. We finally get that the native strand is much stiffer than the denatured portion of the molecule.

4 Conclusions

In this work we applied the cavity method to solve and fit to experimental data a phenomenological model of DNA stretching. The approach adopted ease the calculation of the elongation and the fit by allowing to understand changes of the fitting parameters as perturbations of the cavity equations. We believe that the results obtained here can be naturally extended to study heterogeneous polymers, block copolymers and protein helix-coil transitions in general.

References

1. C. Bustamante et al., Science **265**, 1599–1600 (1994)
2. P. Cluzel et al., Science **271**, 792–794 (1996)
3. S. Cocco et al., Phys. Rev. E **70**, 011910 (2004)
4. H. Fu et al., Nucl. Acids Res. **38**, 5594–5600 (2010)
5. P.J. Hagerman, Annu. Rev. Biophys. Biophys. Chem. **17**, 265–286 (1988)
6. M. Hegner et al., Proc. Natl. Acad. Sci. **96**, 10109–10114 (1999)
7. O. Kratky, G. Porod, Recueil des Travaux Chimiques des Pays–Bas **68**, 1106–1122 (1949)

8. A. Lebrun, R. Lavery, Nucl. Acids Res. **24**, 2260–2267 (1996)
9. M. Mezard, G. Parisi, Eur. Phys. J. B **20**, 217–233 (2001)
10. Y. Miyatake et al., J. Phys. C: Solid State Phys. **19**, 2539 (1986)
11. I. Rouzina, V.A. Bloomfield, Biophys. J. **80**, 882–893 (2001)
12. S.B. Smith, Y. Cui, C. Bustamante, Science, **271**, 795–799 (1996)
13. S. Smith, L. Finzi, C. Bustamante, Science **258**, 1122–1126 (1992)
14. C. Storm, P.C. Nelson, Theory of high-force dna stretching and overstretching. Phys. Rev. E **67**(5), 051–906 (2003)
15. J. van Mameren et al., Proc. Natl. Acad. Sci. **106**, 18231–18236 (2009)
16. S. Whitelam, P.L. Geissler, S. Pronk, Phys. Rev. E **82**, 021907 (2010)
17. J. Yan, J.F. Marko, Phys. Rev. E **68**, 011905 (2003)

Idiosyncrasy as an Explanation for Power Laws in Nature

Salvador Pueyo

1 Idiosyncrasy in Nature

One central theme of complex systems theory is the identification of the mechanisms behind power laws in nature. Most attention has focused on simple mechanisms. Here I show that, in broad conditions, power laws with exponent close to $\tau = 1$ also arise from complex combinations of mechanisms that, in isolation, would not necessarily produce scale invariance. This contribution is a synthesis of papers by the author in journals of ecology and of climatology (the main ones being [12, 13]), which have, however, implications beyond these fields.

A fundamental difference between empirical research and simulations is the role of noise. Typically, empirical data result from the combination of the studied phenomenon with a myriad of other factors, whose joint effect is effectively random because of its high dimensionality. A major challenge of empirical research is separating these two components. In contrast, computers are unable to produce noise, with pseudo-random number generators being used to reproduce it imperfectly. In this aspect, simulation models give a biased view of nature.

In some empirical observations there might be no fundamental difference between *signal* and *noise*, if no single factor dominantes in the ocean of mechanisms contributing to each datum. This could well be the case e.g., for the *species abundance distribution* (SAD), i.e., the frequency distribution $P(n)$ of the number n of individuals belonging to each of the species in an ecological community or in a sample. Many simple mechanisms have been proposed to explain the shape of SADs [9], but naturalists are often skeptical about them. A huge number of elements affect the abundance of one given species (among them, its life cycle,

S. Pueyo (✉)
Institut Català de Ciències del Clima (IC3), Barcelona, Catalonia, Spain
e-mail: spueyo@ic3.cat

Á. Corral et al. (eds.), *Extended Abstracts Spring 2013*, Trends in Mathematics 2,
DOI 10.1007/978-3-319-08138-0_13

its potential longevity and reproduction rate, the kinds of resources it consumes and the proportions in which they are needed, the types of places used e.g., for refuge or for laying eggs, its physiological response to a variety of environmental factors, the types of predators, parasites and infectious agents that can affect it and how they respond to its abundance, its capacity and patterns of movement, its propensity or not to form colonies or flocks or to more complex forms of cooperation, the peculiarities of its sexual reproduction if any, etc.).

The variety of factors acting differently on different species suggests that each species could be ecologically *idiosyncratic*, i.e., different from the rest in ways that cannot be described with a few words or a few parameter values. In fact, groups of related species will often share some features, but will differ in others. While biological species are not 100 % idiosyncratic, they appear to be so to a large extent. This is the basis of the *idiosyncratic theory of biodiversity* by Pueyo et al. [12]. There could be many more instances of idiosyncrasy in other contexts.

This leads us to the need of identifying probability distributions that represent noise alone, with no signal. This could make us think of the normal or the log-normal, because of the central limit theorem. However, this theorem presumes a specific way of combining the causative factors (either additive or multiplicative) and these factors have some requirements in terms of mean and variance. We are interested in distributions that are even freer of information.

2 Non-informative Probability Distributions

Non-informative distributions have been an object of controversy for more than one century, and caused statistics to split into several schools [8]. While they interest us for other reasons, this controversy is motivated by their role in statistical inference. In Bayesian statistics, a variable or a parameter is assigned a probability distribution over a range of values even when only one can be correct (e.g., we can assign a distribution to a physical constant), expressing the plausibility of each possible value when the real one is unknown. For some data D, the PDF of a parameter θ is

$$f(\theta|D) \propto f(\theta) f(D|\theta), \tag{1}$$

where $f(\theta)$ is the *prior distribution*, meaning the distribution of probability (plausibility) that we would assign to θ if we did not know the data D. Equation (1) can be applied recursively, taking $f(\theta|D_1)$ as the prior probability density when introducing a second data set D_2. Ideally, before introducing any data at all, the prior distribution should be *non-informative*. In fact, in this (and in our) context, this adjective is attributed to distributions that may not be completely free from information, but give no information that is not contained in the enunciate of the problem. Many statisticians do not think that such a distribution exists, which is the reason why mainstream or *frequentist* statistics avoids Eq. (1) by not assigning

probabilities to parameters. Also among Bayesian statisticians there are a variety of positions about this issue [8].

Edwin T. Jaynes (best known for the maximum entropy principle [4]) introduced a criterion known as *group invariance* to determine non-informative distributions [5]. It is especially appealing because it consists of a simple requirement of logical coherence. Its logic has similarities to that of relativity theory.

Consider e.g., the case in which we only know that the variable x expresses a position. Let us introduce a new variable $y = x + c$ (where c is a constant), differing from x only in a change of coordinates. Again, the only thing we know about y is that it expresses a position, so we are forced to assign to it the same distribution as to x. The relation between the PDFs of reparameterized variables is well known, namely

$$f(y) = f(x) \left| \frac{dx}{dy} \right|. \tag{2}$$

The only distribution that leaves the PDF unchanged when introducing $y = x + c$ into (2) is the uniform one, in agreement with intuition.

In contrast to the case of positions, for other variables and parameters there is no ambiguity in the origin of coordinates, because *zero* has a well-defined meaning. However, in some of these cases a change of scale $y = cx$ (e.g., a change of units [1]) leaves the enunciate of the problem unchanged. Then, the distribution that remains invariant under Eq. (2) is a power law with exponent $\tau = 1$,

$$f(x) \propto x^{-1}. \tag{3}$$

For example, the author proposed to apply this criterion in the inference of climate sensitivity S [13], which quantifies the roughly linear relation between climate forcing ΔF (e.g., due to emitted CO_2) and global warming ΔT after reaching a steady state,

$$\Delta T = S \Delta F. \tag{4}$$

Note that, if our distribution is to encode only the form of Eq. (4), it should not change when inverting it, because it follows from (4) that

$$\Delta F = \lambda \Delta T,$$

where λ is the climate feedback parameter $\lambda = S^{-1}$. This is true whenever the PDF of $z = \ln(S)$ (i.e., $z = -\ln(\lambda)$) is symmetric about $z = 0$, but $z = 0$ corresponds to $S = 1$, whose physical meaning depends on the units. As units are arbitrary (and do not alter the form of Eq. (4)), the PDF of z should be symmetric not only about $z = 0$ but also about any other value of z, i.e., the distribution of z should be

uniform, which translates to the power law in Eq. (3) when expressed in terms of S (or of λ) [13],

$$f(S) \propto S^{-1}. \tag{5}$$

3 Frequency Distributions with Little Information

The two previous sections give us the two key ingredients for the theoretical framework presented in this paper: idiosyncrasy (Sect. 1) and Jaynes' group invariance criterion (Sect. 2). Besides using the distributions obtained with this criterion as a tool for inference, Jaynes [6] noted that they could have a translation to frequency distributions in some cases, but he does not seem to have developed the notion of idiosyncrasy as a condition for this correspondence.

We obtain the prior in Eq. (3) as an intermediate step to estimate a parameter with a single value, S. However, the parameters of other equations with the same shape as (4) can take more than one value. Consider e.g., Fourier's equation of thermal conductivity

$$\mathbf{q} = -k\nabla T.$$

Different materials have different k, so, unlike S, we can obtain an empirical frequency distribution for k. While it is highly plausible that the abundances of different biological species can be considered idiosyncratic because of the variety and complexity of factors determining them, this is not so clear for the case of the thermal conductivities of different materials. However, starting from this hypothesis, the empirical PDF of k in 189 solid materials was analyzed by the author ([13], § 4.3) and did result into a distribution very close to (3) in a broad range. Note that this is an instance of empirical power law that can be hardly interpreted as the result of any process of self-organization. Grandison and Morris [3] also found a figure close to Eq. (3) for the frequency distribution of biochemical pathway kinetic rate parameters.

In the case of SADs, if species are fully idiosyncratic, knowing n for an unidentified species should give us no information about anything else. Since an SAD contains no reference to e.g., location, whichever distribution we choose will remain invariant when changing location. However, for most types of distribution, the value of n would give us some clue whether it refers to a whole continent or to the researcher's backyard. There is only one distribution for which the SAD does not change when changing spatial scale. Even though n is a discrete variable, Pueyo et al. [12] proved that this distribution is the direct analogue of Eq. (3),

$$P(n) \propto n^{-1}. \tag{6}$$

However, if, as usual, we are dealing with sets of species with a characteristic size (e.g., insects), Eq. (6) cannot be our final answer, because the total number of individuals of all the species in the community is limited for physical reasons, while Eq. (6) would imply that some species would exceed this number of individuals, whichever it is.

There is a well-known method to obtain a distribution with the least possible information subject to some specified constraints: the maximum entropy formalism (MaxEnt), also due to Jaynes [4]. Even though Jaynes [7] was clear about this point, there is little awareness that the non-informative distribution is a needed input for MaxEnt.

In the case of SADs, starting from Eq. (6) and applying MaxEnt to constrain the mean $\overline{n}$, we obtain a power law with $\tau = 1$ and an exponential bending function

$$P(n) \propto n^{-1} \exp^{-\phi n}; \tag{7}$$

see [12]. This equation corresponds to the log-series distribution, which was one of the first ever used to fit an empirical SAD [2] and is still widely applied. While some empirical SADs are well fitted by Eq. (7), others display small departures, which is not surprising because species are not fully idiosyncratic. The author showed that sharing resources or predators among species does not, in principle, alter Eq. (7), but similarities in the shape of the equations describing their population dynamics can have an effect [12]. However, using Taylor series, Pueyo [11] also found that most empirical SADs can be explained from small perturbations around Eq. (7). The simplest deviation consists of a truncated power law with an exponent close to $\tau = 1$.

4 Conclusions

Probably, there are many instances in which an empirical power law results from some specific mechanism that can be reproduced by simple models, e.g., self-organized criticality [10]. However, some hyper-complex systems can produce observables that are effectively *noise*, and, in many cases, noise implies a distribution close to a power law with exponent $\tau = 1$. It is essential to take this option into account when studying complex systems in the real world.

References

1. R. Baker, G. Christakos, Stoch. Environ. Res. Ris. Assess. **21**, 427–434 (2007)
2. R.A. Fisher, A.S. Corbet, C.B. Williams, J. Anim. Ecol. **12**, 42–58 (1943)
3. S. Grandison, R.J. Morris, Bioinformatics **24**, 741–743 (2008)
4. E.T. Jaynes, Phys. Rev. **106**, 620–630 (1957)

5. E.T. Jaynes, IEEE Trans. Syst. Sci. Cybern. SSC-**4**, 227–241 (1968)
6. E.T. Jaynes, Found. Phys. **3**, 477–493 (1973)
7. E.T. Jaynes, *Probability Theory: The Logic of Science* (Cambridge University Press, Cambridge, 2003)
8. R.E. Kass, L. Wasserman, J. Am. Stat. Assoc. **91**, 1343–1370 (1996)
9. B.J. McGill et al., Ecol. Lett. **10**, 995–1015 (2007)
10. G. Pruessner, *Self-Organised Criticality* (Cambridge University Press, Cambridge, 2012)
11. S. Pueyo, Oikos **112**, 392–405 (2006)
12. S. Pueyo, F. He, T. Zillio. Ecol. Lett. **10**, 1017–1028 (2007)
13. S. Pueyo. Clim. Chang. **113**, 163–179 (2012)

Symmetric Division Model of Cell Differentiation Systems

Daniel Sánchez-Taltavull and Tomás Alarcón

1 Introduction

Tissues in higher multi-cellular organisms, have a hierarchical structure where we find different types of cells. These different types are structured from non-specialised cells which only proliferate to specialise, fully-differentiated cells which have a specific function but have completely lost the ability to proliferate. A special type of cell, the so-called *stem cells*, is the only one that have the ability for self-renewal, i.e., the ability of, upon proliferation, producing cells of its own type (more stem cells). In addition, stem cells have also the ability of differentiating into more specialised cells which have lost the ability to self-renew and therefore when they proliferate they produce cells that have moved one step further down the differentiation cascade. This cascade culminates with fully differentiated cells which have lost the ability to proliferate: They perform a specific function within the organism during their life-time and then they die. The intermediate stages between stem cells and fully differentiated cells are sometimes referred to as *transient amplifying cells*.

This work is mainly motivated by the role stem cells play in cancer since the ability of normal stem cells for self-renewal can be subverted and used by the tumour to proliferate and invade the normal tissue. There is also the possibility that the so-called *cancer stem cells*, i.e., cells that after undergoing a number of gene mutations acquire the ability for self-renewal, exist. Since invasion of a healthy tissue by a growing tumour can be understood in terms of the competition between two populations where one or the other may go extinct the study of the stability of

D. Sánchez-Taltavull (✉) • T. Alarcón
Centre de Recerca Matemàtica, Barcelona, Catalonia, Spain
e-mail: dsanchez@crm.cat; talarcon@crm.cat

Á. Corral et al. (eds.), *Extended Abstracts Spring 2013*, Trends in Mathematics 2,
DOI 10.1007/978-3-319-08138-0_14

the corresponding populations is an appropriate starting point for the mathematical modelling of this process.

One particular issue we would like to analyse is the effect of regulation by the fully differentiated cells on the proliferation of the stem cells. The purpose of the aforementioned differentiation cascade is to replenish the fully differentiated cell compartment as they die. Since fully differentiated cells are carrying a particular function within the tissue they belong to, their numbers are usually tightly regulated and thus must be the proliferation of stem cells. In addition, since stem cells are self-renewing dis-regulation of such mechanisms can lead to uncontrolled growth and therefore to cancer.

Regarding the effects of dis-regulation of stem cell proliferation on cancer, we study the effect of *symmetric division* on the evolution of the cell population. It is commonly believed that stem cells normally divide asymmetrically so that their pool stays roughly constant in size. This means that when a stem cell divides one of the daughter cells remains a stem cell whereas the other differentiates. However, many stem cells can divide symmetrically, i.e., producing two stem-cell descendants, specially in conditions such as injuries which involve the need for high cell turn over. The mechanisms controlling the transition between these two modes of division must be under strict controls since its dis-regulation may induce abnormal growth of the stem cell population and therefore lead to cancer.

Related to this issue of symmetric and asymmetric division, another aspect of the problem that we would like to address is the effect of the length of the differentiation cascade on the stability of the population. For most tissues the differentiation cascade is not characterised so the number of TAC stages remains unknown.

2 Hierarchical Model

The variables that our model will take into account are x_0, which represents the number of stem cells, x_i for $i = 1, \ldots, n-1$ representing the number of differentiated cells at the stage i of the differentiation cascade, x_n which represents the number of mature cells, and x_{n+1} representing the amount of signal generated by the mature cells, which controls the size of the stem cells compartment. The possible reactions are described in the following table:

Rate	$(x_0, x_1, \ldots, x_n)$	Description
$W_1 = x_0 p$	$(1, 0, \ldots, 0)$	Duplication
$W_2 = x_0 d_0$	$(-1, 2, 0, \ldots, 0)$	Differentiation
$W_3 = x_0 x_{n+1} \lambda_0$	$(-1, 0, \ldots, 0, -1)$	Death of stem cell
$W_{2+2i} = x_i \lambda_i$	$(0, \ldots, -1, \ldots, 0)$	Death of x_i
$W_{3+2i} = x_i d_i$	$(0, \ldots, -1, 2, 0, \ldots, 0)$	Differentiation x_i
$W_{2+2n} = x_n \lambda_n$	$(0, 0, \ldots, -1, 0)$	Death of mature cell
$W_{3+2n} = x_n s$	$(0, 0, \ldots, 0, 1)$	Mature cell produces signal
$W_{4+2n} = x_{n+1} \lambda_{n+1}$	$(0, 0, \ldots, 0, -1)$	Clearance of signal

Then, the behaviour of our model is described by the following master equation

$$\frac{\partial P_X}{\partial t}(t) = \sum_r W(X-r,r,t)P(X-r,t) - W(X,r,t)P(X,t).$$

The mean-field behaviour of this system is described by the following system of ordinary differential equations:

$$\begin{cases} \dot{x}_0 = px_0 - x_0 d_0 - x_0 x_{n+1}\lambda_0 \\ \dot{x}_i = 2x_{i-1}d_{i-1} - x_i\lambda_i - x_i d_i \qquad i = 1,\ldots,n-1 \\ \dot{x}_n = 2x_{n-1}d_{n-1} - x_n\lambda_n \\ \dot{x}_{n+1} = x_n s - x_{n+1}\lambda_{n+1} - x_{n+1}x_0\lambda_0. \end{cases}$$

There are two fixed points namely $(0,0,\ldots,0)$, which corresponds to the extinction of the system, and a positive fixed point of the form $x_{n+1} = (p-d_0)/\lambda_0$, for some realistic parameters.

3 Stability

In order to ascertain how the long term-survival of the population depends on the length of the chain, the duplication probability of the stem cells and the death rate of the mature cells we made some simulations in Fig. 1.

The extinction are produced for two different reasons, the more typical is that there is a small number of stem cells for $p < 0.55$, the second one is more interesting, an small increase in the number of stem cells causes big fluctuations in the whole system; see Fig. 2.

A larger chain has the following three effects, small number of stem cells required to keep a population of matures of size M. Fluctuations in stem cells compartment

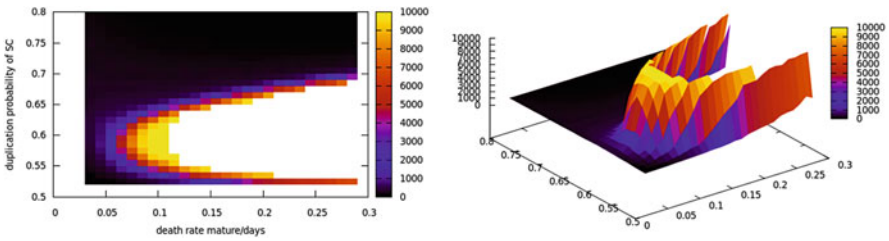

Fig. 1 This plot (two different points of view of it) represents the extinction time of the system depending on the parameters λ_n and p. The length of the differentiation cascade is 5, the x-axis is the death rate of the mature cells, the y-axis is the duplication probability of the stem cells, the z-axis is the days needed to get an extinction, the *white colour* means that more than 10,000 days are needed to get an extinction

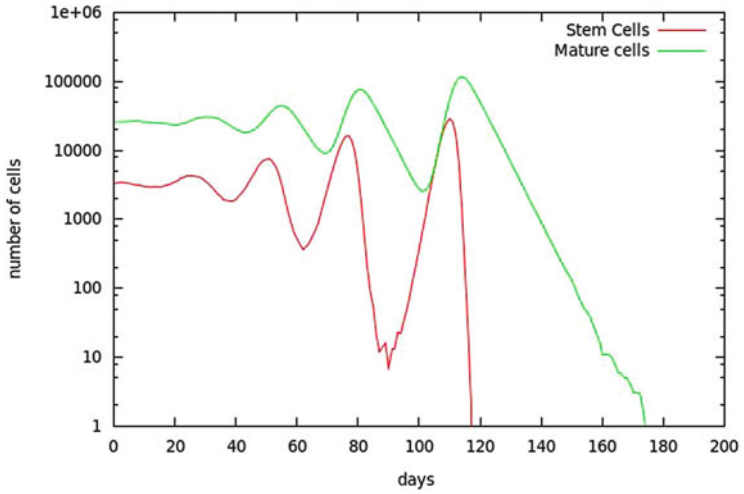

Fig. 2 Gillespie simulation of a system with some values of p and λ_0 that kill in a short time the population

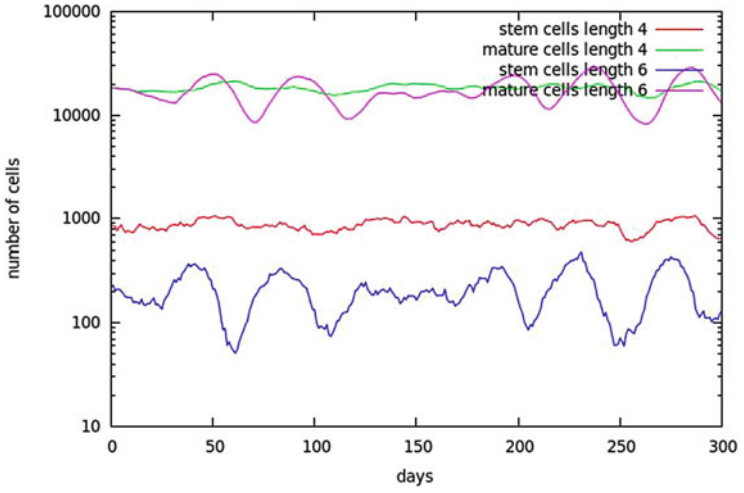

Fig. 3 Two different systems with the same number of mature cells at the meta-stable state, one has a differentiation chain of length 4, the other one 6, we can see that the length 4 system is more stable

has a bigger effect on whole system. If the number of stem cells decreases, more time is required to have a decrease in the signal compartment. This increases the extinction probability; see Fig. 3.

4 Conclusions

We present a new mechanism of extinction in which the delay between the changes in the stem cells compartment and the changes in mature cells compartment contributes to unstabilize the population. The length of the differentiation cascade contributes to protect the tissues against mutations who led to symmetric division.

We have identified a new extinction mechanism in which the coupling between fluctuations that increase the pool stem cells and the delay in stem cell regulation leads to the extinction of the stem cell population and, therefore, to the eventual extinction of the whole. If there is an increase in the number of stem cells due to fluctuations, such fluctuation in the number of stem cells will propagate along and be amplified by the differentiation cascade in an amount which typically scales as 2^L, where L is the length of the cascade. Since the regulation of stem cell proliferation by the fully differentiated cells has a delay of L-time units, the negative feed-back between both populations may lead to extinction of the stem cells and therefore of the whole population.

A larger chain has three different effects. Small number of stem cells required to keep a population of matures of size M. Fluctuations in stem cells compartment has a bigger effect on whole system. If the number of stem cells decreases, more time is required to have a decrease in the signal compartment. This increases the extinction probability.

Biologically, our result seems to indicate that longer chains, which favour extinction, would protect the tissue against mutations leading to symmetric stem cell division. From the perspective of the evolutionary dynamics of cancer, this model leads to a scenario where two mutations are needed for tumour evolution: One disregulating stem cell differentiation (identically to the previous case) and another one disregulating stem cell death.

Free Energy Landscape Analysis of Mesoscopic Model for Finding DNA-Protein Binding Sites

Rafael Tapia-Rojo, Juan José Mazo, Andrés González, M. Luisa Peleato, Maria F. Fillat, and Fernando Falo

1 Introduction

The physical modelization of biomolecules requires a careful choice of the scale of work depending on the problem we wish to study. All-atom simulations allow an accurate description of the system but within small time scales and severe size limitations subject to the available computational power. Coarse-grained models gather groups of atoms in point particles simplifying greatly the system but keeping the essence of the important interactions in the problem of study. At this level, the free energy landscape (FEL) of the system appears as a powerful tool to extract relevant information from a system with a high number of degrees of freedom.

We propose here a coarse-grained model for DNA-protein interaction problem. Transcription from DNA to RNA appears as a complex problem that requires regulation via DNA-protein interaction. Our model considers a particle as a generic protein that diffuses along the DNA chain with an interaction term that is coupled to local openings (bubbles). By applying an algorithm we are able to extract the FEL of the system and identify possible binding sites as those states with lower free energy. We focus mainly on the so called Transcription Starting Site (TSS), where the RNA-polymerase binds before transcription starts.

R. Tapia-Rojo (✉) • J.J. Mazo • A. González • M.L. Peleato • M.F. Fillat • F. Falo
Instituto de Biocomputación y Física de Sistemas Complejos, Universidad de Zaragoza, Zaragoza, Spain
e-mail: rafa.t.rojo@gmail.com; juanjo@unizar.es; andresglez2005@gmail.com; mpeleato@unizar.es; fillat@unizar.es; fff@unizar.es

Á. Corral et al. (eds.), *Extended Abstracts Spring 2013*, Trends in Mathematics 2,
DOI 10.1007/978-3-319-08138-0_15

2 The Model

We base our model on a modified Peyrard–Bishop–Dauxois (PBD) model [1, 4]. PBD model reduces the complexity of DNA to a set of N point particles that represent the base pairs of the chain. The only degrees of freedom are the coordinates $\{y_n\}$ which stand for the distance between each base pair. The total Hamiltonian of the model accounts for two phenomenological interactions, the intra-base and inter-base potentials,

$$\mathcal{H} = \sum_{n=1}^{N} \left[\frac{p_n^2}{2m} + V(y_n) + W(y_n, y_{n-1}) \right],$$

where $p_n = m\, dy_n/dt$ is the linear momentum of the n-th base pair and m is its reduced mass. The potential $W(y_n, y_{n-1})$ describes the inter-base pair or *stacking* interactions and its model by an anharmonic interaction. The intra-base pair potential $V(y_n)$ takes the form of a Morse potential (usual in chemical bonds) with an entropic barrier to account for solvent interaction.

Inspired in the one-dimensional diffusion of DNA-binding proteins, we include now a new degree of freedom to the traditional PBD model, a Brownian particle that slides along the DNA chain [5]. This particle interacts with the DNA through the phenomenological potential

$$V_{\text{int}}(X_p, \{y_n\}) = -\frac{B}{\sqrt{\pi\sigma^2}} \sum_n \tanh(\gamma y_n) e^{-(X_p - na)^2/\sigma^2},$$

which depends on the particle position X_p and the DNA instantaneous configuration $\{y_n\}_{n=1}^{N}$. This potential is just a sum of gaussian wells, each centered at the n-th base (na) and whose amplitude depends on the opening of the base pair. The hyperbolic tangent term just saturates the interaction strength. In this sense, the particle interacts more intensely with open regions of the sequence. In addition, the base pairs are also affected by the particle, so that they are more likely to be opened if the particle is within its range of interaction.

3 Methods

Langevin dynamics simulations: The model is simulated by integrating numerically $N + 1$ Langevin equations (N base pair plus the particle) using an stochastic Runge–Kutta algorithm. Each of the DNA sequences we study is simulated in five different realizations each one covering 40 μs, with a preheating time of 1 μs, reasonable times from a biological perspective. The simulation temperature is $T = 290$ K. We use periodic boundary conditions for the diffusing particle and

fixed boundary conditions for the sequence, adding 10 *CG* base pair clamps of at the end of each sequence to provide "hard-boundaries" and avoid end effects.

Analysis: We aim to find the most important conformational states in the dynamics in order to obtain a biological interpretation. To do so we apply an algorithm that allows us to obtain the Free Energy Landscape (FEL) of the system [3] so that the most relevant states can be identified and quantified. We start applying Principal Component Analysis to the trajectories to reduce greatly the dimensionality of the system but keeping most of the information. Next we translate the five reduced trajectories and the particle trajectory into a Conformational Markov Network (CMN). This coarse-grained picture is constructed by discretizing the conformational space explored by the system in order to define the nodes (microstates) of the network. Next, the links between the nodes are set according to the jumps between the microstates in the trajectories. In this sense, nodes are weighted (P_i), and the links directional and weighted (P_{ij}). In order to define the conformational states of the system, we split the CMN into its basins of attraction, i.e., regions in which the probability fluxes (P_{ij}) converge to a common state (attractor) of the network. To do so we apply the stochastic steepest descent algorithm, developed in [3]. Each basin corresponds to a coarse-grained macrostate of the system. From the basin network we can build FEL of the system represented as a hierarchical tree diagram (dendrogram), by assigning to each node a free energy according to its weight $F_i/kT = \log P_W - \log P_i$, where P_W is the weight of the weightiest node. This magnitude is used as a control parameter, increasing it step by step from the weightiest node, so that new nodes arise, together with their links. Most relevant states can now be identified as those more populated and, in addition, the topology of the network informs us about possible transitions between them.

Study of cyanobacterial genome: In this work, we focus on a concrete genome, analyzing promoters from Anabaena PCC 7120 [2]. Cyanobacteria constitute an interesting model as they show differentiated cells (heterocysts) that need several transcriptional changes to develop. In addition, several well characterized promoters are available so that our computational results can be clearly compared with experimental works.

4 Results

We show now provisional results of some cyanobacteria promoters we have analyzed so far. *TSS finding and base-pair opening*: We analyze promoter sequences comprising between 100 and 200 base-pairs. Figure 1 shows the base-pair opening profile for each promoter sequence with the TSS site highlighted. We find in any case a peak located around the TSS site. This means that, on average, this site is likely to be open, this is, bubbles form with high probability around the TSS.

Promoters with different characteristics have been chosen for the analysis. As Fig. 1 shows, some of the analyzed sequences contain a single TSS while others more than one. Even though in every case all the TSSs can be identified with

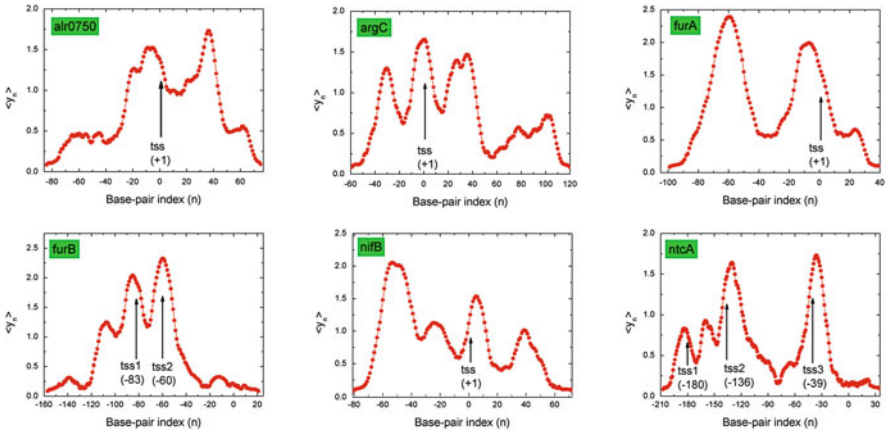

Fig. 1 Mean base-pair position for each of the six analyzed promoters. We can find a peak around the tss in every case meaning that bubbles are likely to be formed around this site

this representation, it is interesting to extract further information from the model. Specifically, different TSSs may show different activity levels depending on the amount of RNA they produce. We refer to this as the strength of each promoter. The relative height of the peaks in Fig. 1 may be a qualitative indicative of this behavior, but a quantitative study motivates the use of the algorithm described in Sect. 3. Another remarkable point in Fig. 1 is the appearance of multiple peaks apart from the ones marked as TSS, revealing the possibility of additional binding sites or just the existence of "false positives". Further discussion can be also done in this point, as the relative strength of the TSS compared to other possible binding sites found in our model can be studied and related with the known biological behavior.

FEL analysis of highlighted promoter: We choose the most interesting promoter we have analyzed so far in order to illustrate the analysis method exposed above. The interest of ntcA promoters lies in the fact that it displays more than one TSS and so it is subject to further biological interpretation. Figure 2 shows the free energy dendrogram for the ntcA promoter, with the set of basins and their accumulated weight corresponding to its TSS sites highlighted. In addition we draw the typical macrostate of the branch.

Promoter ntcA contains three different TSSs. The interpretation of the free energy dendrogram matches with the biological studies of ntcA. TSS3 and TSS1 are just transcribed when there is no nitrogen in the environment. TSS3 is a stronger site, as transcription last for a longer time and the site is still active when the heterocyst is mature. On the other hand, TSS1 is just active transitorily. TSS2 is a constitutive site, so it is always transcribed. This may explain the relative importance found in our analysis.

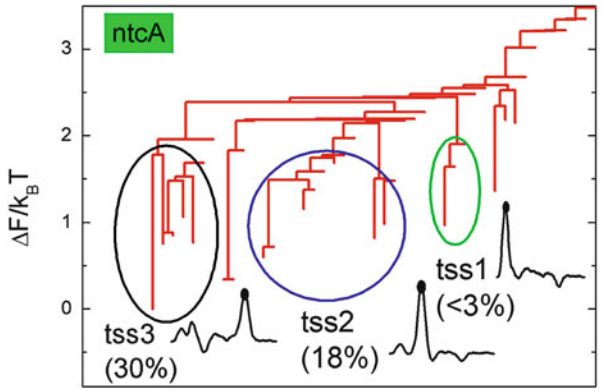

Fig. 2 Free energy dendrogram for ntcA. The TSSs appear as populated branches with relative occupations that inform about the importance of each site

5 Conclusions and Further Work

In this work we use a previously developed mesoscopic model for DNA-protein interaction to analyze the genome of a cyanobacteria organism. The goal is to identify and characterize the TSSs of each of the analyzed promoters. This site is observed to show a larger mean opening due to the formation of bubbles. This behavior is greatly influenced by the dynamics of the generic protein. In order to analyze quantitatively the sequences we apply an algorithm that translates the trajectories onto a complex network so that the free energy dendrogram can be obtained. From this analysis, most relevant sites in the dynamics can be found and related to the biological behavior of each promoter.

This work is to be continued in two main directions. First, further biological interpretation can should be done from the basin networks and the free energy dendrogram. Each of the chosen genes show different regulation features that may be related to the physical parameters found in our analysis. Additionally, more promoters are to be simulated and analyzed in order to complete the work and validate our model and method.

References

1. T. Dauxois, M. Peyrard, A.R. Bishop, Phys. Rev. E **47**, 684 (1993)
2. J. Mitschke, A. Vioque, F. Haas, W.R. Hess, A.M. Muro-Pastor, PNAS **108**, 20130–20135 (2011)
3. D. Prada-Gracia, J. Gómez-Gardenes, P. Echenique, F. Falo, PLoS Comput. Biol. **5**, e1000415 (2009)
4. R. Tapia-Rojo, J.J. Mazo, F. Falo, Phys. Rev. E **82**, 031916 (2010)
5. R. Tapia-Rojo, D. Prada-Gracia, J.J. Mazo, F. Falo, Phys. Rev. E **86**, 021908 (2012)

Are First Order Phase Transitions Possible in Disordered Low-dimensional Non-equilibrium Systems?

Paula Villa and Miguel Ángel Muñoz

1 Introduction

Quenched disorder has a dramatic effect on both the statics and the dynamics of phase transitions [5, 7, 10]. An argument by Imry and Ma explains why symmetries, in low dimensional systems, cannot be spontaneously broken in the presence of quenched random fields [9]. In a nutshell, the argument is as follows. Suppose a discrete symmetry (e.g., Z_2 or up-down) was actually spontaneously broken in a d-dimensional system and imagine a region of linear size L with a majority of random fields opposing the broken-symmetry state. As a direct consequence of the central limit theorem, by reversing the state of such a region the bulk free energy would decrease proportionally to $L^{d/2}$, but this inversion would also lead to an interfacial energy cost proportional to L^{d-1}. Confronting these two opposing contributions for large region-sizes it follows that for $d \leq 2$ the first dominates, making the broken-symmetry state unstable (if the distinct phases are related by a continuous symmetry, soft modes reduce the effect of the boundary conditions to L^{d-2} and the marginal dimension is $d = 4$ [1]). Thus, the energetics of low-dimensional systems is controlled by the random field and this is symmetric, thus preventing symmetries from being spontaneously broken. Instead, in higher dimensional systems, the situation is the opposite, symmetries can be spontaneously broken and phase transitions do exist.

P. Villa (✉)
Departamento de Electromagnetismo y Física de la Materia, Universidad de Granada, Granada, Spain
e-mail: pvilla@ugr.es

M.Á. Muñoz
Instituto Carlos I de Física Teórica y Computacional, Universidad de Granada, Granada, Spain
e-mail: mamunoz@onsager.ugr.es

Á. Corral et al. (eds.), *Extended Abstracts Spring 2013*, Trends in Mathematics 2,
DOI 10.1007/978-3-319-08138-0_16

The Imry–Ma argument (i) is backed by more rigorous renormalization group calculations, which prove that no symmetry-breaking occurs even at the marginal case $d = 2$ (where rough interfaces could potentially break the argument above [1]), (ii) holds for equilibrium systems (where the free energy is well defined), (iii) has been verified in countless examples both experimentally and numerically, and (iv) has been extended to quantum phase transitions [4, 16].

Remarkably, a recent work by Barghathi and Vojta [2], has shown that—in blatant contrast with the equilibrium case—in genuinely non-equilibrium systems including absorbing states [6, 8, 12, 14], for which there is not such a thing as a free energy, second-order phase transitions do survive to the presence of random fields even in one-dimensional cases; see also [13, 15]. The Imry–Ma does not apply to these non-equilibrium systems owing to the presence of absorbing states, and states of broken symmetry can exist in the presence of random fields.

Let us shift the discussion to first-order phase transitions, at which system properties such as the magnetization, energy, density, etc, change abruptly as a control parameter crosses a threshold value, at which two different phases coexist. As shown by Aizenman and Wehr, first-order phase transitions in low-dimensional equilibrium systems are rounded (made less sharp) by disorder and, even more remarkably, the rounding may result in a critical point, i.e., first-order/discontinuous phase transitions become second-order/continuous ones upon introducing (random-field) disorder [1]. A similar conclusion applies to the case of random interactions [1, 3]; indeed, a random distribution of interactions (e.g., bonds) locally favors one of the two phases and thus, it has the same effects as random fields. In close analogy with the argument above for the absence of symmetry-breaking, also in this case, regions (or "islands") of arbitrary size of one of the phases appear in a stable way within the other. Therefore, islands exist within islands on any of the two phases in a nested way, leading always to hybrid states. Hence, two distinct states cannot possibly coexist and first-order transitions are precluded in disordered low-dimensional equilibrium systems.

2 Analysis

In the light of the discussion above on how, shifting to the non-equilibrium realm, some fundamental cornerstones of equilibrium Statistical Mechanics are shattered, one could wonder if first-order phase transitions, and hence, phase coexistence, might be possible in low-dimensional non-equilibrium disordered systems; see Table 1 for a synthetic summary. Aimed at shedding some light on this issue we study non-equilibrium models with absorbing states in the presence of disorder.

More specifically, we study one particular model, similar in spirit to the well-known "contact process" [8, 11, 12, 14], in which two particles are needed to generate an offspring while isolated particles can spontaneously disappear. As a first step, we verify that the pure (or "clean") version of the model exhibits a first-order transition

Table 1 Random fields in low-dimensional disordered systems. Summary of the effects of quenched random fields on the existence of: continuous/second-order (with a concomitant spontaneously symmetry breaking), and discontinuous/first-order (with associated phase coexistence) phase transitions in $d \leq 2$ systems, both in equilibrium and in non-equilibrium cases (these last with one or more absorbing state)

System with random fields $d \leq 2$	2nd order spontaneous symmetry breaking	1st order (phase coexistence)
Equilibrium	NO [9]	NO [1,3,9]
Non-equilibrium (abs. states)	YES [2]	?

separating an active phase from an absorbing one. Then we introduce disorder and scrutinize its effects.

After a careful analysis of such system we observe that the discontinuous transition do not survive to the introduction of disorder and becomes rounded!

3 Discussion

We conjecture that first-order phase transitions cannot appear in low-dimensional disordered systems with an absorbing state. In other words, the Imry–Ma–Aizenman–Wehr–Berker argument for equilibrium systems can be extended to non-equilibrium situations including absorbing states. The underlying reason for this is that, even if the absorbing phase is fluctuation-less and hence is free from the destabilizing effects the Imry–Ma argument relies on, the other phase—that should coexist with it—is active, and hence, intrinsic fluctuations destabilize it as predicted by the Imry–Ma–Aizenman–Wehr–Berker argument, precluding phase coexistence.

Remarkably, in the case studied by Barghathi and Vojta, in which the Imry–Ma is violated (for a second-order phase transition) the two broken-symmetry states are absorbing ones: once the symmetry is broken in any of the two possible ways, the system becomes completely free from fluctuation effects and, consequently, the Imry–Ma argument breaks down. Thus, the only possibility to have first-order phase transitions in low dimensional disordered systems would be to have (in its pure-version counterpart) a discontinuous phase transition from one absorbing state to another, different, absorbing state. We are not aware of any such transition. Therefore, we conclude with a negative answer to the question in the title, at least, for non-equilibrium systems with absorbing states.

References

1. M. Aizenman, J. Wehr, Phys. Rev. Lett. **62**, 2503 (1989)
2. H. Barghathi, T. Vojta, Phys. Rev. Lett. **109**, 170603 (2012)

3. A.N. Berker, Phys. A **194**, 72 (1993)
4. R.L. Greenblatt, M. Aizenman, J.L. Lebowitz, Phys. Rev. Lett. **103**, 197201 (2009)
5. G. Grinstein, A. Luther, Phys. Rev. B **13**, 1329 (1976)
6. G. Grinstein, M.A. Muñoz, in *Fourth Granada Lectures in Computational Physics*, ed. by P.L. Garrido, J. Marro. Volume 493 of Lecture Notes in Physics (Springer, Berlin/Heidelberg, 1997), pp. 223–270
7. A.B. Harris, T.C. Lubensky, Phys. Rev. Lett. **33**, 1540 (1974)
8. M. Henkel, H. Hinrichsen, S. Lübeck, *Non-Equilibrium Phase Transitions*, vol. 1 (Springer, Dordrecht, 2008)
9. Y. Imry, S.K. Ma, Phys. Rev. Lett. **35**, 1399 (1975)
10. Y. Imry, M. Wortis, Phys. Rev. B **19**, 3580 (1979)
11. T.M. Liggett, *Interacting Particle Systems*. Classics in Mathematics (Springer, Berlin/Heidelberg/New York, 2004)
12. J. Marro, R. Dickman, Nonequilibrium Phase Transition in Lattice Models (Cambridge University Press, Cambridge, 1999)
13. N. Masuda, N. Gibert, S. Redner, Phys. Rev. E **82**, 010103 (2010)
14. G. Odor, *Universality in Nonequilibrium Lattice Systems: Theoretical Foundations* (World Scientific, Singapore, 2008)
15. S. Pigolotti, M. Cencini, J. Theor. Biol. **265**, 609 (2010)
16. T. Vojta, Phys. Rev. Lett. **90**, 107202 (2003)

Labquakes: Acoustic Emission During the Compression of Porous Materials

Eduard Vives*, Jordi Baró*, Xavier Illa*, and Antoni Planes*

It has recently been shown [1, 5] that there might be a strong relation between the statistics of the acoustic emission AE detected during the compression of porous materials in the lab and the statistics of real earthquakes. In this extended abstract we discuss details of this comparison and what would be the consequences if the two phenomena turn out to be in the same universality class.

Small samples (with an initial transversal section A of few mm^2 and a height h of few mm) of a porous material are compressed in the vertical direction between two plates by increasing the applied load F at a constant compression rate, i.e., $P(t) = F(t)/A = Rt$. Results are reported for Vycor which is known to have a skeleton of almost pure quartz (SiO_2) and pores of sizes in the nm range. The porosity is of the order of 30–40 %. Preliminary results with other natural porous materials have also been presented [6]. By using AE sensors attached to the compression plates it has been possible to detect the ultrasonic signals (in the range 20 kHz–2 MHz) generated when small portions of the skeleton break. The signals are amplified and treated by well-known avalanche analysis techniques: by means of an imposed threshold one can separate individual events and measure their properties (time of occurrence t_i, energy E_i, amplitude, duration, ...) in a way very similar to what is done in seismology to characterize earthquakes. The study of different specimens compressed at different rates $R = 0.2$, 1.6 and 12.2 kPa/s has rendered three catalogues of data $t_i, E_i, i = 1, \ldots, N$ with sizes $N = 11{,}022$,

*We thank the Ministerio de Economía y Competitividad (Spain) for financial support (MAT2010-15114). We also thank A. Corral for helpful comments.

E. Vives (✉) • J. Baró • X. Illa • A. Planes
Departament d'Estructura i Constituents de la Matèria, Universitat de Barcelona, Barcelona, Catalonia, Spain
e-mail: eduard@ecm.ub.edu; xavier.illa@ub.edu; antoniplanes@ub.edu

Á. Corral et al. (eds.), *Extended Abstracts Spring 2013*, Trends in Mathematics 2,
DOI 10.1007/978-3-319-08138-0_17

28,202 and 2,431 signals respectively. Given the different compression rates R, the full durations of the catalogues are also very different: $\Delta t = 132{,}705$, 18,948 and 2,296 s respectively. The data sets have been analyzed in order to check four different statistical laws that are known to apply to real earthquake data and that are briefly summarized below.

Gutenberg–Richter law. It states that the distribution of energies obeys to the power-law probability density

$$dP(E) = g(E)dE \propto E^{-\epsilon} dE. \tag{1}$$

The exponent was found to be $\epsilon \simeq 1.66 \pm 0.15$ for the major earthquake catalogue.

Modified Omori law. After a big event, called main-shock (MS), one can define the sequence of aftershocks (AS) as those events with an energy smaller than the energy of the MS. The rate of aftershocks (number of AS events per unit time) decays as [7]

$$\dot{N}_{AS}(t) = \frac{K}{(t-c)^p}, \tag{2}$$

where c is a constant, t is the time since the MS, p is an exponent that takes values typically close to 1, and K is defined below. This is the a law that shows the existence of correlations in the occurrence of earthquakes. If the times of occurrences of earthquakes were a Poisson process one would get $p \simeq 0$. In practice, in order to gain statistics, the Omori law can be evaluated not only after the very few big MSs, but by considering as MSs, all those events in a certain energy window $(E, E+\Delta E)$.

Productivity law. This law also refers to the sequence of aftershocks and establishes that the constant K depends on the energy of the MS as [3]

$$K \propto E^{2\alpha/3}, \tag{3}$$

with α in the range $(0.7, 0.9)$. Aftershock activity decays in time, but it is larger the larger the energy of the MS.

Universal scaling law for the waiting times. One decade ago, a different way to study earthquake correlations was proposed, which is independent of the definition of MS and AS (which is, to some extent, controversial). It consists of studying the distribution of waiting times δ between consecutive events. For a given catalogue corresponding to a certain Earth region and time interval $(t_0, t_0 + \Delta t)$, one considers all the events above a certain threshold E and evaluates the sequence of waiting times between them. The distributions of waiting times $dP(\delta) = D(\delta)d\delta$ exhibit a strong dependence with the region, the time period and the threshold E. But, interestingly, these distributions can be scaled into a universal function Φ defined by the following scaling property [2]

$$D(\delta) = \frac{1}{r_E}\Phi(\delta r_E), \tag{4}$$

where r_E is called the average activity rate and is computed as the number of signals above E, divided by the catalogue duration Δt. In other words, all the dependencies with the cutoff E, the region and the specific time interval, are taken into account by the average rate r_E. Corral showed [2] that, if one considers regions and time intervals in which the rate r_E is stationary (it does not change in time subintervals), the function Φ is a gamma function. But, if one considers catalogues obtained for the same time period $t, t + \Delta t$ but mixing waiting times corresponding to regions with very different activity rates the function Φ displays a double power-law behavior,

$$\Phi(x) = \begin{cases} x^{-(1-\nu)} & \text{if } x \ll 1 \\ x^{-(2+\xi)} & \text{if } x \gg 1, \end{cases} \tag{5}$$

where $(1-\nu) \simeq 0.9$ and $(2+\xi) \simeq 2.2$. Heuristic arguments were given in order to show that these two exponents are related to the distribution of earthquake activities in the different regions of the Earth crust.

The above four laws (1)–(4) have been tested in labquakes. Note that in the AE experiments there is no access to the location of the events, so there is no mechanism to separate the catalogues into different regions. Figure 1a shows the analysis of the Gutenberg–Richter behavior of the experimental data. It can be observed that the power-law behavior extends several orders of magnitude. We have also confirmed the stationarity of the histograms by reanalyzing the data after dividing the duration Δt in intervals of 3,000 s. Figure 1b shows the test of both the Omori law and the

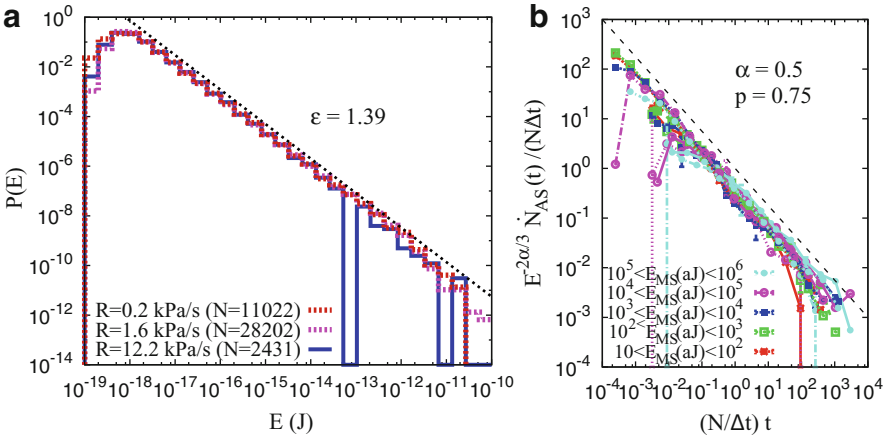

Fig. 1 *Left:* Energy distribution of AE events during the compression of Vycor at three different compression rates. *Right:* Analysis of the AS production after every MS in different energy windows and for different compression rates

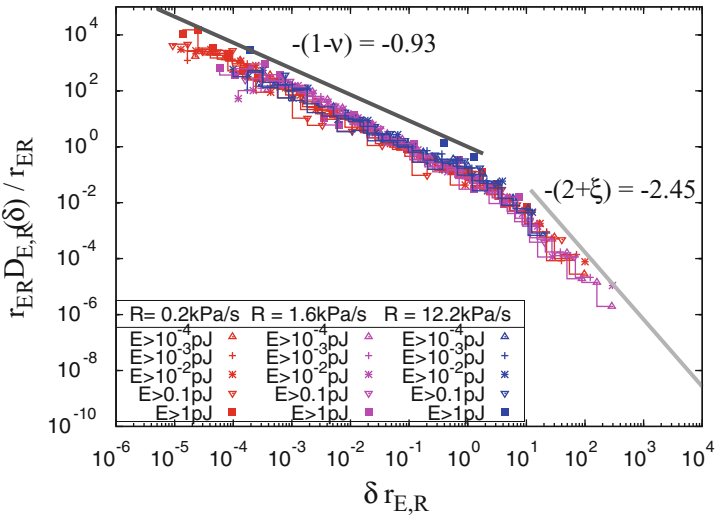

Fig. 2 Universal scaling law for the distribution of earthquakes. The plot shows data corresponding to different compression rates R and different energy thresholds E, scaled by the average activity rate $r_{E,R}$ that depends on the energy threshold and the compression rate

Table 1 Summary of the main exponents characterizing the different power-law behaviours observed in earthquakes and labquakes

		Earthquakes	Labquakes
Gutenberg–Richter	ϵ	1.67 ± 0.15	1.40 ± 0.05
Omori	p	0.9–1.8	0.75
Productivity	α	0.7–0.9	0.5 ± 0.1
Waiting times	$1 - \nu$	0.9	0.93
Scaling law	$2 + \xi$	2.2	2.45

productivity law. Data corresponding to different compression rates R and MS in different energy windows (as indicated) are well overlapped. Note that the temporal scale has been normalized by the average activity rate of every catalogue ($N/\Delta t$) since, for every experiment, there is an unknown factor in the energy measurement that depends on the coupling of the specimen with the compression plates. Figure 2 shows the universal scaling behavior for the distribution of waiting times. As it can be seen, an overlap of all the data corresponding to different compression rates R, and energy thresholds E (as indicated) is also very good.

Table 1 shows the values of the exponents found in the compression experiments and the values found for earthquakes.

The first point to be discussed is the fact that the exponents characterizing the Universal Scaling function behaviour show a good agreement. This result clearly suggests that this scaling extends many orders of magnitude (from the energies of earthquakes in the range of 10^{10}–10^{18} J to the energies of our AE events in the range 10^{-18}–10^{-11} J).

The agreement with earthquake data is even more remarkable since one should take into account that the exponents $1 - \nu$ and $2 + \xi$ for earthquakes are obtained from the scaling of data from catalogues mixing regions with very different activity rates r. In our case we have three catalogues, each of them considered as a unique region, that display strong fluctuations in the activity rate along time. Typically, in the beginning of the compression experiment activity (measured along 1 min intervals) is very low $\sim 10^{-2}$ events/s, but one can find intervals close to big failure events in which the activity reaches 10^2 events/s. This means that the activity in our "regions" is not stationary is not stationary, but spans 4 orders of magnitude. This result reflects the existence of a spatio-temporal symmetry in the distribution of rates.

A second interesting issue to be discussed refers to whether or not the values of the exponents characterizing the three laws (1)–(3) are universal or not. A priory, from the table, one would conclude that some of the values are not in complete agreement. But, one should take into account that the determination of energies for earthquakes is not a straightforward procedure. First, there are different definitions of energy; second different seismometers are used depending on the energy ranges, the different regions on Earth, and also instruments have evolved very much in time (some catalogues in Japan extend for one century). For this reason the exact value of the Gutenberg–Richter ϵ exponent for earthquakes has sometimes been questioned. For instance Kagan has suggested [4] that it could be close to 1.50. Note that, contrarily, the AE signals from labquakes are measured with a single detection setup for all energies and during the whole experiment. Uncertainties in the energy determination and the incompleteness of the catalogues could also justify that the ϵ, p and α exponents are not in full agreement.

References

1. J. Baró et al., Phys. Rev. Lett. **110**, 088702 (2013)
2. A. Corral, Phys. Rev. E **68**, 035102 (2003)
3. A. Helmstetter, Phys. Rev. Lett. **91**, 058501 (2003)
4. Y.Y. Kagan, Tectonophysics **490**, 103 (2010)
5. E.K.H. Salje et al., Philos. Mag. Lett. **91**, 554 (2011)
6. E.K.H. Salje et al., Am. Mineral. **98**, 609–615 (2013)
7. T. Utsu et al., J. Phys. Earth **43**, 1 (1995)

Part II
Emergence, Spread and Control of Infectious Diseases

Editor

Andrei Korobeinikov

Preface

The *Workshop on Emergence, Spread and Control of Infectious Diseases* was held on June 10–11, 2013, at the Centre de Recerca Matemàtica. This interdisciplinary workshop, which was organized in the framework of the Mathematics of Planet Earth 2013 (MPE2013) programme, attracted more than 30 scientists, mathematicians and biologists, affiliated in Spain, Europe and around the world, and proved to be highly successful. The invited lectures were delivered by Dolors Vaqué (Institut de Ciències del Mar, CSIC), Andreas Meyerhans (Universitat Pompeu Fabra), Josep Sardanyés (Institut de Biologia Evolutiva, CSIC-UPF) and Valery Perminov (Tomsk Polytechnical University, Rusia).

The objective of the workshop was to bring together biologists and mathematicians to exchange ideas and, most importantly, challenges arising in biology and epidemiology and where the involvement of mathematical methods and participation of mathematicians can be particularly beneficial. The organizers also hoped that the workshop gave to young researchers an opportunity to present their results and findings and to learn from more experienced colleagues. In the organizers' view, the best possible outcome of the workshop would be forming on-going interdisciplinary collaborations between mathematicians and biologists. This workshop was the first of a series of planned events at CRM on Mathematics in Life Sciences.

We present in this volume six Extended Abstracts coming from a selection of the talks given at the workshop.

The organizers would like to thank all participants and authors, who contributed to the workshop's success. We would also like to thank the CRM for financial support, and the CRM's administrative staff for wonderful organization of this event.

Barcelona, Catalonia, Spain Andrei Korobeinikov

Global Properties of a Core Group Model for Sexually Transmitted Infections

Carles Barril and Andrei Korobeinikov

1 Introduction

We refer to sexually transmitted diseases as the illnesses caused by pathogens which are transmitted mostly via sexual contacts. Although STDs are a very heterogenous set of diseases, there is a common property closely related to their dissemination: the spread of STDs over the population is not homogenous, but it depends on the sexual habits of the population. More precisely, population splits in two groups: those who have a risky sexual behaviour and those who take care during sexual contacts, which is known as the core.

Despite its important role in the epidemic's development, the dynamics of the core haven't been considered in many STDs models and it have been treated as a population group of constant size. Some exceptions are those given in [1]. Our objective in this paper is to study how the social behaviour affects the dynamics of the core.

2 The Core Model

We now are ready to propose a first model. We consider three population groups, A, S and I, representing the non-core individuals, the susceptible core individuals that are not infected, and the infected ones. The total population N is the sum of these three subpopulations, two of which form the sexual network core (S and I). Given the nature of the infectious process, it is reasonable to consider that new infections

C. Barril (✉) • A. Korobeinikov
Centre de Recerca Matemàtica, Barcelona, Catalonia, Spain
e-mail: cbarril@crm.cat; akorobeinikov@crm.cat

Á. Corral et al. (eds.), *Extended Abstracts Spring 2013*, Trends in Mathematics 2,
DOI 10.1007/978-3-319-08138-0_18

occur at a rate proportional to the product of susceptible by infected (SI). According to this model, people in the A compartment cannot become infectious. However, we assume that there is a exchange of people from the A and the S compartments due, for instance, as a result of education, the infection state or the social environment. Although the processes that have a role in this flow can be very complex, as a first approximation we consider that it only depends on the A, S and I variables. As an example, one might think that an increase in the number of the infected may have a dissociative effect on the individuals who are about to enter into the core. In this sense, we will consider a general function that reflects the recruitment of individuals from A to S, or vice versa, and that this *recruitment rate* has the form $r(A, S, I)$. Thus, the system of differential equations that summarizes these relations between the compartments A, S and I is

$$\begin{aligned} \dot{A} &= b - r(A, S, I) - mA \\ \dot{S} &= r(A, S, I) - \beta SI + \alpha I - dS \\ \dot{I} &= \beta SI - \alpha I - cI, \end{aligned} \tag{1}$$

where m, d and c are the per capita mortality rates associated to A, S and I respectively, and α is the recovery rate.

We should be aware that everything can be much more complex and that here we are considering a simplified situation in order to understand some aspects of the STDs dynamics. Therefore, we do not consider processes such as vertical transmission from mother to child, nor the fact that there may be a time lag during which the infected are not infectious (the latency). We neither distinguish between individuals exposed to the pathogen and infected ones. These and other factors have to be addressed separately.

As A, S and I represent individuals, they should be positive. The function r has to satisfy the following two consistency conditions:

$$\begin{aligned} 0 \leq \dot{A}(0, S, I) = b - r(0, S, I) \quad &\Longrightarrow \quad r\,(0, S, I) \leq b, \\ 0 \leq \dot{S}(A, 0, I) = r(A, 0, I) + \alpha I \quad &\Longrightarrow \quad r\,(A, 0, I) \geq -\alpha I. \end{aligned}$$

These two conditions ensure that the first octant is a positive invariant set. From now on, we restrict our analysis to the first octant and the statements related to stability are done considering the restricted topology on this space.

3 General Results of the Model

By means of mathematical analysis tools we have proven a series of properties satisfied by system (1). In order to expose all of them in a condensed manner, we summarize these results in the list below.

1. The set $\triangle = \{(A, S, I) \in \mathbb{R}^3_+ \mid b/\mu_{\max} \leq A + S + I \leq b/\mu_{\min}\}$ is a positively invariant set and a global attractor of the model. Here, $\mu_{\max} = \max\{m, d, c\}$ and $\mu_{\min} = \min\{m, d, c\}$. Biologically, it means that the total population, N, tends to the interval $[b/\mu_{\max}, b/\mu_{\min}]$.
2. In the plane $S = S^* = (\alpha + c)/\beta$ equation $\dot{I} = 0$ holds. If $S < S^*$ then $\dot{I} < 0$, and if $S > S^*$ then $\dot{I} > 0$.
3. If $\mathbf{R}_{00} = b/\mu_{\min} S^* \leq 1$ then a subset of the plane $I = 0$ is a global attractor of the model. That is, the infected individuals tend to disappear in this case.
4. If $\mathbf{R}_0 = b/dS^* \leq 1$, then there are no endemic equilibria (there are no fixed points in $I > 0$).
5. If $r\,(A, S, 0) - dS^* > 0$ for all $A, S \geq 0$, then there is at least one endemic equilibrium in $I > 0$.
6. If $r\,(0, S, 0) - dS^* > 0$, $\partial r/\partial A > 0$ and $\partial r/\partial I < 0$ hold, then there is just one endemic equilibrium.

4 Global Properties of the Model for Particular Recruitment Rates

It seems that a comprehensive study of the general system (1) is a challenging task, as we have observed that there is a strong dependence between the function r and the number of fixed points. For this reason, we focus on two families of recruitment rates:

- $r(A) > 0$ with $\partial r/\partial A > 0$,
- $r(A, S) = k + pA + qAS$, with $k, p, q \geq 0$ and $k < b$.

For these recruitment rates, we proved the following results related to the asymptotic behaviour of theirs orbits.

Theorem 1. *If $r(A) > 0$ with $\partial r/\partial A > 0$, there is a basic reproduction number*

$$\mathbf{R}_0 = \frac{r^*}{dS^*},$$

and the following holds:

1. *If $\mathbf{R}_0 > 1$, then the system has a unique endemic equilibrium which is a global attractor in the first octant's interior* $\mathrm{Int}(\mathbb{R}^3_+)$.
2. *If $\mathbf{R}_0 \leq 1$ then the system has no endemic equilibria and the only fixed point of the model is in the $I = 0$ plane, and it is a global attractor in the first octant $\mathbb{R}^3_+$.*

Theorem 2. *For the case $r(A, S) = k + pA + qAS$, with $k, p, q \geq 0$ and $k < b$, there is a basic reproduction number*

$$\mathbf{R}_0 = \frac{mk + p\,(b - dS^*)}{mdS^*} + q\frac{(b - dS^*)}{md},$$

and the following holds:

1. *If* $\mathbf{R}_0 > 1$ *then the system has a unique endemic equilibrium, which is a global attractor in the first octant's interior* $\mathrm{Int}(\mathbb{R}^3_+)$.
2. *If* $\mathbf{R}_0 \leq 1$ *then the system has no endemic equilibria and the only fixed point of the model is over the* $I = 0$ *plane. The question about if this equilibrium is a global attractor of the first octant* $\mathbb{R}^3_+$ *remains open.*

Both proofs are based on the Lyapunov's Second Method and La Salle's Invariance Principle [3] and use the Volterra type Lyapunov Function (cf. [2, 4]). Under hypothesis of Theorem 1, the system (1) becomes uncoupled, and to proof the global stability of the endemic fixed point (A^*, S^*, I^*) for $R_0 > 1$ we have used the Lyapunov function

$$V(S, I) = S - S^*\ln S + B(I - I^*\ln I),$$

where $B = c/(\alpha + c)$. Under the hypotheses of Theorem 2, for $R_0 > 1$ we have used the Lyapunov function

$$V\,(A, S, I) = A - A^*\ln A + B\left(S - S^*\ln S\right) + D\left(I - I^*\ln I\right),$$

where $B = pA^*S^*/(qA^* + pA^*S^*)$ and $D = cB/(\alpha + c)$.

References

1. K.P. Hadeler, C. Castillo-Chávez, A core group model for disease transmission. Math. Biosci. **128**(1), 41–55 (1995)
2. A. Korobeinikov, Lyapunov functions and global properties for SEIR and SEIS epidemic models. Math. Med. Biol. **21**(2), 75–83 (2004)
3. J. LaSalle, Some extensions of Liapunov's second method. IRE Trans. Circuit Theory **7**(4), 520–527 (1960)
4. A.V. Melnik, A. Korobeinikov, Lyapunov functions and global stability for SIR and SEIR models with age-dependent susceptibility. Math. Biosci. Eng. **10**(2), 369–378 (2013)

Incorporating Landscape Heterogeneities in the Spread of an Epidemic in Wildlife

Luca Gerardo-Giorda, Joshua Keller, and Alessandro Veneziani

1 Introduction

One of the main difficulties in the modeling and numerical simulation of the spread of an infectious disease in wildlife resides in properly taking into account the heterogeneities of the landscape. Forests, plains and mountains present different levels of hospitality, while large interstates, lakes and major waterways can provide strong natural barriers to the epidemic spread. A canonical approach has been to discretize both population and geography into geopolitical units and consider the movement of individuals from unit to unit [4]. This approach, however, does not well represent the biological realities of animal movement, since animals do not move at the scale of geopolitical units. We combine a standard SEI epidemiological model with a diffusion process to account for movement as a continuous process across a continuous region [1]. This results in a system of parabolic reaction-diffusion equations with nonlinear reaction term. Landscape heterogeneities are accounted for by including in the computational domain the significant geographical features of the area. We discretize the resulting model in time by an IMEX scheme and in space by finite elements. To show the effectiveness of the method, we present numerical simulation for rabies epidemics among raccoons in New York State.

L. Gerardo-Giorda (✉)
Basque Center for Applied Mathematics, Bilbao, Spain
e-mail: lgerardo@bcamath.org

J. Keller
Department of Biostatistics, University of Washington, Seattle, WA, USA
e-mail: kellerjp@uw.edu

A. Veneziani
Department of Mathematics and Computer Science, Emory University, Atlanta, GA, USA
e-mail: ale@mathcs.emory.edu

Á. Corral et al. (eds.), *Extended Abstracts Spring 2013*, Trends in Mathematics 2,
DOI 10.1007/978-3-319-08138-0_19

2 Continuous Model for Movement

Let $x \in \Omega \subset \mathbb{R}^2$. The SEI model subdivides the population individuals at time t into Susceptibles $S(t)$, Exposed $E(t)$, and Infectious $I(t)$. We consider as unknown the vector $\mathbf{u}(x,t) = [s(x,t), e(x,t), i(x,t)]^T$ of their densities in location x at time t. Thus,

$$S(t) = \int_\Omega s(x,t)\,dx, \quad E(t) = \int_\Omega e(x,t)\,dx, \quad \text{and} \quad I(t) = \int_\Omega i(x,t)\,dx.$$

In more general cases, a fourth group of Recovered individuals could be considered (SEIR models), but in our case study this class is empty, as rabies is lethal for raccoons. However, the extension of the following arguments to SEIR models is straightforward.

We model the spread of an epidemic in Ω by a vector generalization of the normalized Fischer's equation, a nonlinear system of reaction-diffusion equations of parabolic type

$$\partial_t \mathbf{u} - \operatorname{div}(\boldsymbol{\nu}\nabla\mathbf{u}) = (\mathrm{A} - \mathrm{B}(\mathbf{u}))\,\mathbf{u} \quad \text{in } \Omega \times [0,T], \tag{1}$$

where

$$\boldsymbol{\nu} = \begin{pmatrix} \nu_s & 0 & 0 \\ 0 & \nu_e & 0 \\ 0 & 0 & \nu_i \end{pmatrix}, \quad \mathrm{A} = \begin{pmatrix} \alpha & \alpha & 0 \\ 0 & -\sigma & 0 \\ 0 & \sigma & -\phi \end{pmatrix}, \quad \mathrm{B}(\mathbf{u}) = \begin{pmatrix} -\mu_0 n & -\beta s & 0 \\ \beta i & -\mu_0 n & 0 \\ 0 & 0 & -\mu_0 n \end{pmatrix},$$

$n = s + e + i$ being the total population, α the reproduction rate, β the infectiveness of a contact between a susceptible and an infectious individual, $1/\sigma$ the latency period, and $1/\phi$ the life expectancy of a rabid animal. We assume a density dependent natural mortality rate $\mu_0 n$. System (1) is completed by a suitable initial value $\mathbf{u}^0$, and suitable boundary conditions on $\partial\Omega$. In general homogeneous Neumann boundary conditions are used to model an isolated environment, but other boundary conditions can be considered as well: an homogeneous Dirichlet boundary condition would model an hostile environment, while a Robin boundary condition would model a migratory dynamics.

3 Modeling Landscape Heterogeneities

We consider here two kinds of geographical heterogeneity in the region of interest, that are modeled in two different ways. *Localized heterogeneities*, such as the presence of major waterways and roads, locally drive the movement of the wild animals. *Extended heterogeneities* are particular features significantly affecting the

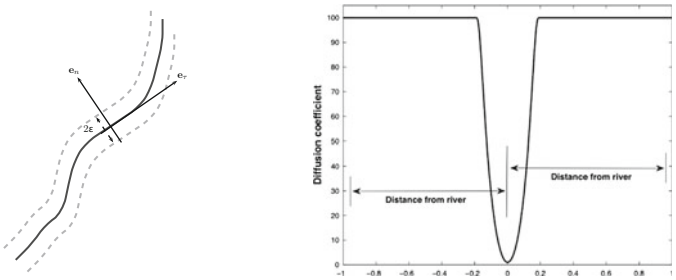

Fig. 1 *Left:* $(\mathbf{e}_\tau, \mathbf{e}_n)$ reference frame along the river. *Right:* diffusion coefficient in the normal direction to the river, with $\nu_H = 100$, $\nu_L = 1$, and $\epsilon = 0.2$ (Figures reproduced from [1], with permission)

dynamics of the infection in a whole region. This is the case, for instance, of lakes, forests and mountains.

The effect of localized heterogeneities on the population dynamics are included by locally modifying the diffusivity tensors. In each point of the river we identify a local frame of reference $(\mathbf{e}_\tau, \mathbf{e}_n)$; see Fig. 1 (left). In a neighborhood Σ of width 2ε of the river the diffusivity is gradually decreased, from the regular value ν_H to a lower value ν_L, as plotted in Fig. 1 (right). By denoting with $\hat{y}$ is the distance from the river along $\mathbf{e}_n$, the compartmental diffusion tensor $\boldsymbol{\nu}_k$ $(k = s, e, i)$ is first computed in the $(\mathbf{e}_\tau, \mathbf{e}_n)$ reference frame, then referred to the Cartesian global frame of reference, by means of a rotation matrix R aligning the local frame of reference to the global one

$$\boldsymbol{\nu}_k = \mathrm{R}\hat{\boldsymbol{\nu}}_k\mathrm{R}^T, \qquad \hat{\boldsymbol{\nu}}_k = \begin{pmatrix} \nu_H & 0 \\ 0 & \nu_H - (\nu_H - \nu_L)\exp\left(1 - \dfrac{\epsilon^2}{\epsilon^2 - \hat{y}^2}\right) \end{pmatrix}. \tag{2}$$

Strong heterogeneities between different areas naturally induce a partition of the computational domain into homogeneous subregions. To take into account different levels of hospitality, we act on both the carrying capacity of the region, and the diffusion coefficients. For instance, in a unhospital area, we both lower the carrying capacity to reduce the presence of animals at the disease-free equilibrium, and the diffusion coefficient to avoid massive migration towards such area.

4 Finite Dimensional Approximation

Let Δt be a time step and let $t^n = n\Delta t$. System (1) is advanced in time by mixed implicit/explicit (IMEX) finite differences, where the nonlinear term is treated explicitly, while the principal part of the operator is treated implicitly. Space

discretization is based on finite elements (for an introduction to the method see e.g., [3]), since the latter are particularly suitable for complex geometries as real geographic regions can be. On a regular triangular mesh of the domain Ω with N nodes, the unknown is the vector

$$\mathbf{U}^n = \left[[\mathbf{s}_l(t^n)]_{l=1,\dots,N} \ , \ [\mathbf{e}_l(t^n)]_{l=1,\dots,N} \ , \ [\mathbf{i}_l(t^n)]_{l=1,\dots,N} \right]$$

of the nodal values at time t^n. At each time step, we solve the algebraic system

$$(\mathcal{M} + \Delta t \mathcal{A})\mathbf{U}^n = \Delta t \mathcal{F}(\mathbf{U}^{n-1}) + \mathcal{M}\mathbf{U}^{n-1}, \tag{3}$$

where $\mathcal{M}$ and $\mathcal{A}$ are block-diagonal

$$\mathcal{M} = \begin{pmatrix} M & 0 & 0 \\ 0 & M & 0 \\ 0 & 0 & M \end{pmatrix}, \quad \mathcal{A} = \begin{pmatrix} A_s & 0 & 0 \\ 0 & A_e & 0 \\ 0 & 0 & A_i \end{pmatrix},$$

and where M and A_k ($k = s, e, i$) are the classical finite elements mass and stiffness matrices, and where $\mathcal{F}(\mathbf{U}^{n-1})$ is obtained from the right hand side of (1); see [1] for details.

5 Numerical Simulation

For illustrative purpose we apply the method to the spread of a fictitious epidemic of raccoon rabies in the state of New York. A simulation of the actual spread of rabies among raccoons in the area (1990–1996) can be found in [1], where the proposed method proves its effectiveness in qualitatively capturing the early dynamics of the epidemic.

A geographically detailed computational domain of the area of interest can be reconstructed from satellite images or recovered from other similar sources (GIS data, for instance), and suitably triangulated. The strongly heterogeneous regions are then identified directly on the mesh, while the localized heterogeneous effects are included by forcing mesh points in the areas of interest, such as major waterways and highways. We include in the geography the Hudson and Mohawk rivers as barriers, and the mountains in the northern part of the state as a reduced hospitality region.

The coefficients of the model used in the simulation refer to raccoon rabies. The epidemiological parameters (α, β, σ, ϕ) are drawn from literature, while the mortality term μ_0 is estimated indirectly to produce a disease-free equilibrium corresponding to the mean of reported densities for raccoons in the eastern US. We initiate an epidemic cluster in the vicinity of Oneonta (Otsego County), and we plot in Fig. 2 the difference between the infectious density computed with the inclusion

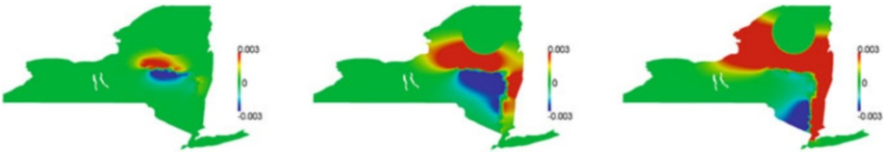

Fig. 2 Effect of the presence of rivers and the reduced capacity region on the infectious density after 12, 24, and 36 months (Figures reproduced from [1], with permission)

of the rivers and the one obtained without the presence of rivers at different times. The barrier effect is clearly appreciable.

The algebraic system (3) does not present any significant difficulty from the numerical standpoint. Its $3N \times 3N$ matrix is symmetric, and the solution at each time step can be computed by a Conjugate Gradient (CG, [3]) method, for which standard, very effective preconditioners are available.

6 Conclusion

The proposed space-continuous model features a double advantage. Geographic details are easily incorporated, and, at the same time, the overall computational cost is very competitive. As a matter of fact, the proposed model requires the tuning of a smaller number of parameters with respect to SEI models based on geopolitical units commonly used in the domain [4]. So far, the diffusion coefficients have been tuned empirically. To improve the knowledge of the model parameters, an estimation procedure of Bayesian type, based on the available observed data, is currently under investigation [2].

References

1. J. Keller, L. Gerardo-Giorda, A. Veneziani, Numerical simulation of a susceptible-exposed-infectious space-continuous model for the spread of rabies in raccoons across a realistic landscape. J. Biol. Dyn. **7**(Suppl 1), 31–46 (2013)
2. G. Puggioni, L. Gerardo-Giorda, L.A. Waller, L.A. Real, Hierarchical models for parameter estimation of SEIR models with application to raccoon rabies spread (In preparation)
3. A. Quarteroni, A. Valli, *Numerical Approximation of Partial Differential Equations* (Springer, Berlin, 1994)
4. L.A. Real, J.E. Childs, Spatial-temporal dynamics of rabies in ecological communities, in *Disease Ecology: Community Structure and Pathogen Dynamics*, ed. by S.K. Collinge, A.C. Ray (Oxford University Press, Oxford/New York, 2006), pp. 168–185

The Phenomenon of Apparent Disappearance in the Marine Bacteriophage Dynamics

Andrei Korobeinikov* **and Vladimir Sobolev****

1 Introduction

In marine microbial biosystems, high magnitude variations in abundance and an unstable dynamics, such as planktonic blooms alternating with extended periods of low abundances, are quite common. In many cases, such blooms are immediate consequences of seasonal variations in temperature, light and other conditions. However, variations in abundance, which are not directly associated with seasonal forcing, are also common; Anderson and May [1] provided numerous examples of observations, where irregular explosions in abundance of clearly non-seasonal nature.

To explain this phenomenon, a number of hypotheses was suggested. In particular, Wommack et al. [13] suggested that the observed dramatic changes in the abundance of a single phage genotype is a consequence of infection by the phage of a blooming bacterial strain ("killing the winner population" concept). A certain drawback of this conjecture is that these authors, as well as Thingstad and Lignell [10] earlier, assumed that a external forcing (such as the influx of a particular limiting nutrient, which create favorable conditions for growth of this

*Supported by the Ministry of Science and Innovation of Spain via Ramón y Cajal Fellowship RYC-2011-08061.

**Partly supported by RFBR grants 13-01-97002 and 12-08-00069.

A. Korobeinikov (✉)
Centre de Recerca Matemàtica, Barcelona, Catalonia, Spain
e-mail: akorobeinikov@crm.cat

V. Sobolev
Samara State Airspace University, Samara, Russia
e-mail: hsablem@gmail.com

Á. Corral et al. (eds.), *Extended Abstracts Spring 2013*, Trends in Mathematics 2,
DOI 10.1007/978-3-319-08138-0_20

particular species) triggered the bloom of this single bacterial species. Nevertheless, the hypothesis that for aquatic bacteria and phages, the observed high magnitude variations in abundance can be a result of phage parasitism on this particular bacterial species, is appealing. This concept was further developed by Hoffmann et al. [6], who suggested that the interaction of a couple "target bacteria-phage" is sufficient for the arising of high-magnitude self-sustained oscillations in abundance of both species, and that no external factor is needed. Unfortunately, this idea was to some extend handicapped by shortcomings of a mathematical model, which assumes the unlimited Malthusian growth of bacteria, and, as a result, is structurally unstable and its outcome crucially depends on the initial conditions. A few years ago V. Sobolev proposed a hypothesis that in predator-prey type models the phenomenon of apparent disappearance does not require seasonal forcing and can be explained with the existence of so-called canard trajectories; see [5, 7] and references therein.

To explain high magnitude irregularities in abundance in a seemingly regular system and the phenomenon of apparent disappearance, we considered a simple autonomous model of bacteria-phage interaction, which assumes neither seasonal or periodic forcing, nor external factors of another nature. Despite its simplicity, this model is capable to produce a result which explains the phenomenon.

2 Bacteriophages

Bacteriophages are small viruses which infect and kill bacteria, and which were discovered independently by Frederick Twort in 1915 and by Félix d'Herelle in 1917. Phages are one of the most widespread and diverse entities in the biosphere. The richest sources of phages, as well as other viruses, is oceans, where about ten million phages per milliliter found in sea water; this figure grows up to $9{\cdot}10^8$ virions per milliliter found in microbial mats at the surface [12]. As much as 70 % of marine bacteria may be infected by phages [8, 12], and it is currently believed that a contribution of viral lysis in controlling marine bacterial abundance is comparable with protist grazing [3, 11].

Bacteriophages are mostly specific for target bacteria, thus forming stable phage-bacteria pairs. There is no direct interaction between these pairs, or, where there is some interaction, it is negligibly weak. (However, there is indirect interaction between pairs, because bacteria of different pairs can compete for the same resource; for simplicity, we disregard this factor.) We assume that the dynamics of these pairs are identical in the sense that for all pairs it is governed by the same principles and depends on the same factors, while the current states of these pairs are independent and randomly distributed.

By their mode of reproduction, phage can be divided into two major types. The first type, the so-called lytic phages, are highly virulent type. The phage of this type begin reproduction immediately after infecting a bacterium, and after a short time lyse the host bacterium, releasing new free phages. Phages of the second type, which are known as the non-lytic, or temperate phages, are either integrating their

genetic material into the chromosomal DNA of the host, or establishing themselves as plasmids. These endogenous phages are then copied with every cell division. They do not kill the host cell, until it starts to show signs of stress. At this stage the endogenous phages become active and start their reproductive cycle, resulting in the lysis of the host cell.

3 The Model

We consider the phages with a lytic reproduction cycle. To describe the interaction of a pair lytic phage-bacteria, we employ a mathematical model with a free-living infective stage of phage. The model is comprised of three populations, namely susceptible bacteria, infected bacteria and free phage, of concentrations $x(t)$, $y(t)$ and $v(t)$, respectively, and postulates that the free-living virus infect the susceptible hosts, that after an instance of infection the infected host moves into the infected class where remains until death, and that the infected hosts produce the free phage. We assume that the proliferation of bacteria is limited by the carrying capacity of environment K, that only uninfected bacteria are able to reproduce, and that all the offspring are susceptible. The infective incidence occur according to the law of mass action, and that the other functional responses are linear. Under these assumptions, the model is

$$\begin{aligned} \dot{x} &= ax\,(1-(x+y)/K) - \alpha xv, \\ \dot{y} &= \alpha xv - dy, \\ \dot{v} &= \sigma y - mv. \end{aligned} \tag{1}$$

Here, a is the per capita bacteria reproduction rate, K is the currying capacity, and $1/d$ and $1/m$ are average life spans of the infected bacteria and the free phage, respectively.

The origin $E_0 = (0,0,0)$ is an equilibrium state of the model, and it is always a saddle point with two negative and one positive eigenvalues. The system also has a phage-free equilibrium state $E_K = (K,0,0)$. A type of this equilibrium, as well as the system general global properties, depends on the basic reproduction number $R_0 = \sigma\alpha K/md$; the phage-free equilibrium E_K is asymptotically stable if $R_0 \leq 1$, and is unstable (a saddle point) if $R_0 > 1$. The system can also have a positive equilibrium state E^* with coordinates $x^* = md/\alpha\sigma$, $y^* = am(R_0-1)/\alpha\sigma(R_0+a/d)$, $v^* = \sigma y^*/m$; $R_0 > 1$ is necessary and sufficient for the existence of equilibrium E^*. Further in this paper we assume that $R_0 > 1$ holds, and hence E^* exists.

A remarkable property of this model is that it admits a supercritical Andronov–Hopf bifurcation: a decrease of a, d or m, or, alternatively, an increase of α, σ and carrying capacity K, eventually leads to the loss of stability of the equilibrium state E^* and to the appearance of a stable limit cycle. In some aspects,

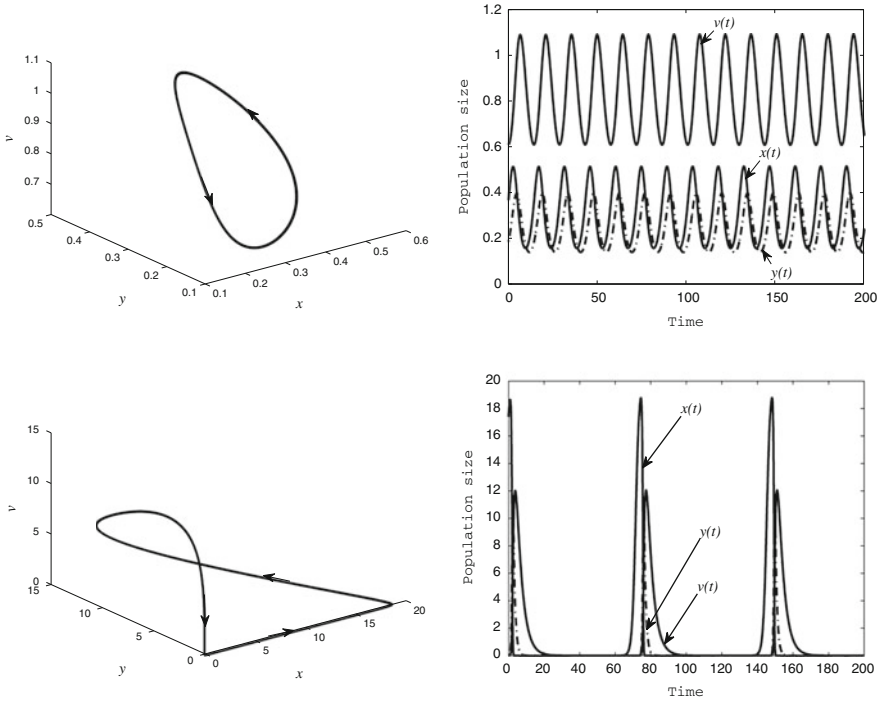

Fig. 1 Appearance and expansion of a limit cycle, and arising of apparent disappearance; here $a = 1.0, \alpha = 1.0, d = 1.0, \sigma = 1.0$ and $m = 0.3$; $K = 3.33$ in the *upper figures*, and $K = 20$ in the *lower ones*

this phenomenon is similar to the effect of enrichment [9]; the principal difference with the effect of enrichment is that a nonlinearity of the incidence rate with respect to the prey population $x(t)$ is essential for the latter, whereas for model (1) the bifurcation occurs even for the bilinear incidence rate (Fig. 1).

Values of a, d, m, α and σ are specific for a particular phage-bacteria pair and remain nearly constant, whereas the carrying capacity K can vary to a large extend. Moreover, it is commonly believed that food is not a limiting factor for bacterial growth [2, 4, 12, 13]; these consideration makes K the most important parameter for the page-bacteria system dynamics and indicates that significant changes of this dynamics are possible in response to variations of environmental conditions. With an increase of K, the size of the limit cycle grows, and the cycle is squeezed to the yv-plane. As a result, it comes into the vicinity of the origin, where all three populations and their rates of changes are very low. The larger K becomes, the closer it comes to and the longer remains in the vicinity of the origin. This implies that the system dynamics changes to large extends in response to variations (for instance, seasonal) of K. This also implies that this system can exhibit the dynamics with long periods of low abundance ("apparent disappearance"), alternating with comparatively short

periods of high abundance. Figures illustrate appearance and development of the limit cycle, and the apparent disappearance phenomenon.

We have to mention that alternations of abundance, when fast explosions of a population followed by equally fast declines, as well as the phenomenon of apparent disappearance, are not uncommon in the population dynamics in general, including terrestrial ecosystems and host-parasite systems. It is likely that in many other cases, where the phenomenon of apparent disappearance cannot be explained by seasonal or external forcing, the mechanism behind this dynamics is the same as, or similar to that described. An essential element of this dynamics is the existence of a stable limit cycle, which passes near a saddle type equilibrium point.

References

1. R.M. Anderson, R.M. May, The population dynamics of microparasites and their invertebrate hosts. Philos. Trans. R. Soc. Lond. Ser. B **291**, 451–524 (1981)
2. F. Azam, Microbial control of oceanic carbon flux: the plot thickens. Science **280**, 694–696 (1998)
3. G. Bratbak, M. Heldal, T.F. Thingstad, B. Riemann, O. Haslund, Incorporation of viruses into the budget of microbial C-transfer. A first approach. Mar. Ecol. Prog. Ser. **83**, 273–280 (1992)
4. W.C. Chin, M.V. Orellana, P. Verdugo, Spontaneous assembly of marine dissolved organic matter into polymer gels. Nature **391**, 568–572 (1998)
5. V. Gol'dshtein, A. Zinoviev, V. Sobolev, E. Shchepakina, Criterion for thermal explosion with reactant consumption in dusty gas. Proc. R. Soc. Lond. A **452**, 2103–2119 (1996)
6. K.H. Hoffmann, B. Rodriguez-Brito, M. Breitbart, D. Bangor, F. Angly, B. Felts, J. Nulton, F. Rohwer, P. Salamon, Power law rank-abundance models for marine phage communities. FEMS Microbiol. Lett. **273**, 224–228 (2007)
7. M. Mortell, R. O'Malley, A. Pokrovskii, V. Sobolev, *Singular Perturbations and Hysteresis* (SIAM, Philadelphia, 2005)
8. L. Prescott, *Microbiology* (Wm.C. Brown Publishers, Dubuque, 1993)
9. M.L. Rosenzweig, Paradox of enrichment: destabilization of explotation ecosystems in ecological time. Sience **171**, 385–387 (1971)
10. T.F. Thingstad, R. Lignell, Theoretical models for the control of bacterial growth rate, abundance, diversity and carbon demand. Aquat. Microb. Ecol. **13**, 19–27 (1997)
11. M.G. Weinbauer, M.G. Höfle, Significance of viral lysis and flagellate grazing as factors controlling bacterioplankton production in an eutrophic lake. Appl. Environ. Microbiol. **64**(2), 431–438 (1998)
12. K.E. Wommack, R.R. Colwell, Virioplankton: viruses in aquatic ecosystems. Microbiol. Mol. Biol. Rev. **64**(1), 69–114 (2000)
13. K.E. Wommack, J. Ravel, R.T. Hill, R.R. Colwell, Hybridization analysis of Chesapeake bay virioplankton. Appl. Env. Microbiol. **65**, 241–250 (1999)

Viral RNA Replication Modes: Evolutionary and Dynamical Implications

Josep Sardanyés

1 Introduction

RNA viruses are obligate parasites infecting bacteria, fungi, plants and animals. Upon infection, RNA viruses replicate within the host cells generating a highly heterogeneous population of viral genomes named quasi-species [4]. Generally, the viral replicase copies the initially infecting positive-sense or genomic strand, producing the negative or antigenomic one. How these templates are then processed for further replication has been a subject of research, and different replication modes (RMs) have been proposed. For instance, if the produced negative template is mainly used as a template for the production of the whole progeny of genomic strands, the linear stamping machine replication (SMR) mode is at play. On the contrary, if both genomic and antigenomic strands are copied with the same efficiency, geometric replication (GR) takes place.

The RM has important evolutionary and dynamical consequences in RNA viruses since it will involve different rates at which mutations accumulate thus affecting the statistical properties of the quasi-species [9]. Roughly, the distribution of mutations per genome within an infected cell for SMR is expected to be Poisson because mutants do not replicat [5]. Consequently, the fraction of mutation-free genomes produced is given by the Poisson null class $e^{-\mu L}$, being μ the per-site mutation rate and L the genome length. However, if all produced strands are used as templates, thus following GR, the distribution of mutant genomes conforms to the Luria–Delbrück distribution [3]. Here, the fraction of mutation-free genomes produced would depend on the number of replication rounds experienced, τ, according to

J. Sardanyés (✉)
ICREA-Complex Systems Lab, Universitat Pompeu Fabra, Barcelona, Catalonia, Spain

Institut de Biologia Evolutiva CSIC, Barcelona, Catalonia, Spain
e-mail: josep.sardanes@upf.edu

Á. Corral et al. (eds.), *Extended Abstracts Spring 2013*, Trends in Mathematics 2,
DOI 10.1007/978-3-319-08138-0_21

$e^{-\tau\mu L}$. Therefore, it is straightforward to see that GR will produce f more mutant genomes than SMR according to the equation $f = (1 - e^{-\tau\mu L})/(1 - e^{-\mu L})$. If only a fraction of the genomic strand progeny replicates, then the RM will be a mixture of SMR and GR that deviates from the Poisson expectation as much as the GR contribution.

Experimental data support different RMs for different viruses. For instance, bacteriophage T2 is thought to replicate mostly by GR because the number of mutants per infected cell fails to fit a Poisson distribution [5]. However, phage ϕX174 data fit well the Poisson distribution, suggesting a SMR model [2]. Within these two extremes, phage $\phi 6$ slightly deviated from the Poisson expectation, an observation interpreted as a result of a mixed model in which some progeny of positive strands was also able to replicate [1].

In this article I review recent advances in the dynamics of the RM for positive-sense single stranded RNA viruses. Then, previous results on a mathematical model describing the amplification dynamics of viral genomes with asymmetries due to different RMs are extended. Specifically, it is proved that the interior equilibrium of the phase plane is globally and asymptotically stable.

2 Viral Replication Modes: Recent Advances

The dynamics of viral RNA amplification was recently quantified for Turnip mosaic virus, and a simple mathematical model was used to fit the experimental data and infer the RM [6]. The same mathematical model was investigated considering natural infections and the fixed points and stability properties of the model were studied analytically and numerically [8]. The next Section extends the results presented in [8].

2.1 Dynamical Evolution Equations

The mathematical model describing the within-cell amplification dynamics of both positive- and negative-sense strands investigated by Sardanyés and coauthors in [8], is given by the next system of differential equations, $\dot{\mathbf{x}} = f(\mathbf{x})$, where $\mathbf{x} = (p, m)$ and

$$\frac{dp}{dt} = rm\left(1 - \frac{p+m}{K}\right) - \delta p, \qquad \frac{dm}{dt} = \alpha rp\left(1 - \frac{p+m}{K}\right) - \delta m. \tag{1}$$

The state variables p and m denote, respectively, the concentration of plus (positive) and minus (negative) viral RNA genomes. Parameter r is the replication rate, K corresponds to the cellular carrying capacity and δ is the genomes degradation rate.

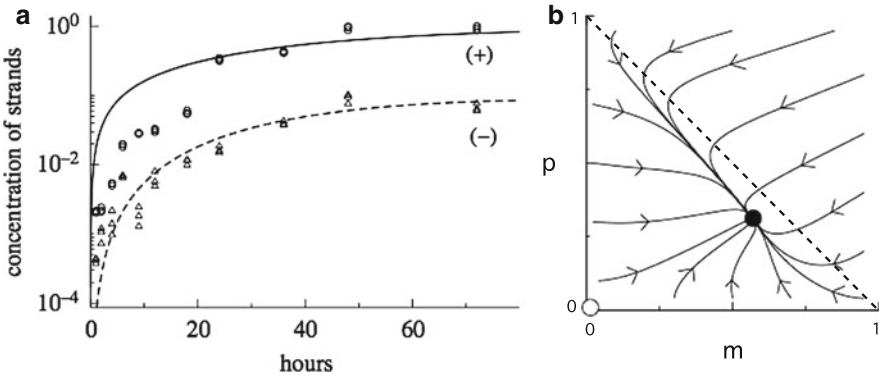

Fig. 1 (**a**) Dynamics of RNA genomes for Turnip mosaic virus. The *dots* and the *triangles* correspond to experimental data for positive and negative strands, respectively. The *solid* and the *dashed lines* are the simulated dynamics using the mathematical model; see [6] for further details. (**b**) Phase portrait for Eqs. (1): the *black circle* is the fixed point involving coexistence of viral genomes. The *open circle* is an unstable equilibrium. The *dashed line* is the boundary $p + m = K = 1$. The *arrows* indicate the direction of the flow

The variables span the two-dimensional phase space $\Gamma := \{p, m \in \mathbb{R}^+ : 0 \leq p + m \leq K = 1\}$.

Previous research on Eqs. (1) computed local stability of the interior fixed point, given by $P^* = (p^*, m^*)$, which involves coexistence of both viral genomes polarities; see the phase portrait in Fig. 1b and [8]. Let us now extend the previous results by analyzing if such a fixed point is globally stable. We claim that Γ is positively invariant. For that we analyze the direction of the vector field on the borders of Γ. On $(0, m)$ the vector field is $\dot{p} = rm(1 - m/K)$ and $\dot{m} = -\delta m$. On $(p, 0)$ the vector field is $\dot{p} = -\delta p$ and $\dot{m} = \alpha r p(1 - p/K)$. Furthermore, on $(p, K - p)$ the vector field is $\dot{p} = -\delta p$ and $\dot{m} = -\delta(K - p)$. Finally, we need to analyze the vector field on the corners of Γ, i.e., $(K, 0)$ and $(0, K)$. On the point $(K, 0)$, the vector field is $\dot{p} = -\delta p$ and $\dot{m} = 0$. Since the second component of the vector field is 0, we do not have enough information to state that solutions will enter into Γ. Then, we analyze how an initial condition will evolve in time near the point $(K, 0)$. To do so we use a local analysis of the behavior of a given initial condition around that point by using a Taylor expansion. On the point $(K, 0)$, the solution is

$$\begin{aligned} \varphi(t) &= \varphi(0) + \dot{\varphi}(0)t + \frac{1}{2}\ddot{\varphi}(0)t^2 + \cdots \\ &= (K, 0) + (-\delta K, 0)t + \frac{1}{2}\left(\delta^2 K, -\alpha r(1 - 2K)\delta K\right)t^2 + \cdots, \end{aligned} \tag{2}$$

since the border in Γ is given by $K = 1$. It turns out that the second-order term of the Taylor expansion is

$$(\delta^2 K, -\alpha r(1 - 2K)\delta K)|_{K=1} = (\delta^2, \alpha r \delta),$$

with $\delta^2 > 0$ and $\alpha r \delta > 0$. The previous calculations indicate that initial conditions near this point will enter into Γ. Analogously, the same behavior is found for point $(0, K)$ (results not shown). Hence, all previous calculations show that trajectories will enter into Q_1 from the three borders of Γ given by $(0, m)$, $(p, 0)$, and $(p, K-p)$. By Poincaré–Bendixson theorem, the ω-limit set of any initial condition on Γ is not void and it is contained in Γ. By Dulac's criterion we will now prove that the interior equilibrium is not a periodic orbit. For an autonomous planar vector field, Dulac's criterion states: let $\dot{\mathbf{x}} = f(\mathbf{x})$ be a continuously differentiable vector field defined on a simply connected subset Ω of the plane, i.e., $\Omega \subset \mathbb{R}^2$. If there exists a continuously differentiable, real-valued function $g(\mathbf{x})$ such that $\nabla \cdot (g(\mathbf{x}) f(\mathbf{x}))$ has constant sign throughout Ω, then there exist no closed orbits lying entirely in Ω. Now we apply Dulac's criterion to our system, with $g = 1$ so,

$$\nabla \cdot f(\mathbf{x}) = \frac{\partial}{\partial p}\dot{p} + \frac{\partial}{\partial m}\dot{m}$$

is defined in our system as

$$\nabla \cdot f(\mathbf{x}) = \frac{\partial}{\partial p}\big(rm(1-m-p)-\delta p\big) + \frac{\partial}{\partial m}\big(\alpha r p(1-m-p)-\delta m\big) = -r(m+\alpha p)-2\delta.$$

Note that since $r, m, \alpha, p, \delta > 0$, the signum of $\nabla \cdot f(\mathbf{x})$ is constant (i.e., $\nabla \cdot f(\mathbf{x}) < 0$) and, since the domain $\Omega = \Gamma$ is simply connected and g and f satisfy the required smoothness conditions, we can conclude that there are no closed orbits in Γ.

Since we have a unique fixed point in Γ, and we discarded the existence of a periodic orbit, according to the Poincaré–Bendixson then it must be the ω-limit set of every initial condition and hence P^* is globally asymptotically stable in Γ.

3 Conclusions and Prospectives

The dynamics of mutation accumulation in viral pathogens is a key evolutionary parameter that still remains poorly understood. Such a subject has been addressed experimentally [1, 2, 5] and both computationally and theoretically [6–9]. Despite these previous investigations, several theoretical questions concerning the dynamics and the evolutionary consequences of different RMs still remain open. For instance:

(i) What are the impacts of stochasticity in the dynamics of positive and negative strands in natural infections in terms of dynamical robustness?
(ii) What are the expected deterministic dynamics in spatially-extended models of asymmetric replication? Do different RMs generate deterministically-driven spatial self-structuring?

(iii) What is the interplay between epistasis and stochasticity or space in terms of dynamical robustness?

Question (i) may be addressed by extending the model here presented to stochastic differential equations (e.g., Fokker–Planck equations). Question (ii) could be tackled with partial differential equations, and question (iii) should consider both previous theoretical approaches also incorporating mutant classes and different nonlinear interactions among mutations.

Acknowledgements I especially thank Ernest Fontich for useful suggestions and Silvia Rubio for English corrections. I also thank Santiago F. Elena, Fernando Martínez and Jose Antonio Daròs for sharing this research subject. This work was funded by the Botín Foundation and by grant NSF PHY05-51164.

References

1. L. Chao, C.U. Rang, L.E. Wong, Distribution of spontaneous mutants and inferences about the replication mode of the RNA bacteriophage $\varphi 6$. J. Virol. **76**, 3276–3281 (2002)
2. D. Denhardt, R.B. Silver, An analysis of the clone size distribution of 1X174 mutants and recombinants. Virology **30**, 10–19 (1966)
3. A. Dewanji, E.G. Luebeck, S.H. Moolgavkar, A generalized Luria–Delbrück model. Math. Biosci. **197**, 140–152 (2005)
4. E. Domingo, C. Biebricher, M. Eigen, J.J. Holland, *Quasispecies and RNA Virus Evolution: Principles and Consequences* (Landes Bioscience, Austin) (2001)
5. S.E. Luria, The frequency distribution of spontaneous bacteriophage mutants as evidence for the exponential rate of phage production. Cold Spring Harbor Symp. Quant. Biol. **16**, 463–470 (1951)
6. F. Martínez, J. Sardanyés, J.A. Daròs, S.F. Elena, Dynamics of a plant RNA virus intracellular accumulation: stamping machine versus geometric replication. Genetics **188**, 637–646 (2011)
7. J. Sardanyés, S.F. Elena, Quasispecies spatial models for RNA viruses with different replication modes and infection strategies. PLoS ONE **6**(9), e24884 (2011)
8. J. Sardanyés, F. Martínez, J.A. Daròs, S.F. Elena, Dynamics of alternative modes of RNA replication for positive-sense RNA viruses. J. R. Soc. Interface **9**, 768–776 (2012)
9. J. Sardanyés, R.V. Solé, S.F. Elena, Replication mode and landscape topology differentially affect RNA virus mutational load and robustness. J. Virol. **83**, 12579–12589 (2009)

System Order Reduction Methods with Application to a Bacteriophages Dynamics Model

Vladimir Sobolev* **and Andrei Korobeinikov****

1 Introduction

The theory and applications of singularly perturbed systems of differential equations, traditionally connected with the problems of fluid dynamics and nonlinear mechanics, has been developed intensively and the methods are applied actively to the solution of a wide range of problems from other areas of natural science. This can be explained by the fact that such singularly perturbed systems appear naturally in the process of modelling various processes, that are characterized by slow and fast motions simultaneously. In many cases it is necessary to consider the behaviour of the system as a whole and not of separate trajectories, and to investigate the system by means of a qualitative analysis. This is what is done in this talk. In the present talk asymptotic and geometrical techniques of analysis are combined for the investigation of singularly perturbed systems. The essence of this approach consists in separating out the slow motions of the system under investigation. Then the order of the differential system decreases, but the reduced system, of lesser order, inherits the essential elements of the qualitative behaviour of the original system in the corresponding domain when the slow integral manifold is attracting.

*Partly supported by RFBR grants 13-01-97002 and 12-08-00069.

**Supported by the Ministry of Science and Innovation of Spain via Ramón y Cajal Fellowship RYC-2011-0806.

V. Sobolev (✉)
Samara State Airspace University, Samara, Russia
e-mail: hsablem@gmail.com

A. Korobeinikov
Centre de Recerca Matemàtica, Barcelona, Catalonia, Spain
e-mail: akorobeinikov@crm.cat

Á. Corral et al. (eds.), *Extended Abstracts Spring 2013*, Trends in Mathematics 2,
DOI 10.1007/978-3-319-08138-0_22

The construction of simplified models is achieved and these simpler models reflect the behaviour of the original models to a high order of accuracy. A mathematical justification of this method can be given by means of the theory of integral manifolds for singularly perturbed systems Note that the pioneering papers were published during the period 1957–1970 by K. Zadiraka [4], V. Fodchuk and Y. Baris, who followed on the work of N. Bogolyubov and Y. Mitropolsky. The existence of slow integral manifolds, stable, unstable and conditionally stable, occur in these papers.

2 Singularly Perturbed System

Consider the system of ordinary differential equations

$$\dot{x} = f(t, x, y, \varepsilon), \tag{1}$$

$$\varepsilon \dot{y} = g(t, x, y, \varepsilon), \tag{2}$$

with $x \in R^m$, $y \in R^n$, $t \in R$. Such systems are called *singularly perturbed systems*, since when $\varepsilon = 0$ the ability to specify an arbitrary initial condition for $y(t)$ is lost. The usual approach to the qualitative study of (1) is to consider first *the limiting system* ($\varepsilon = 0$)

$$\frac{dx}{dt} = f(t, x, y, 0), \tag{3}$$

$$0 = g(t, x, y, 0), \tag{4}$$

and then to draw conclusions about the qualitative behavior of the full system (1), (2) for a sufficiently small ε. For many applied problems, the use of the limiting system instead of the full equations gives acceptable results. However, in some cases the approximation (3), (4) is too crude. We use more exact method for the qualitative asymptotic analysis of singularly perturbed ordinary differential equations. The method relies on the theory of integral manifolds, which essentially replaces the original system by another system on an integral manifold whose dimension is equal to that of the slow subsystem.

Recall that a smooth surface S in $R \times R^m \times R^n$ is called an integral manifold of the system (1), (2) if any integral curve of the system that has at least one point in common with S lies entirely on S. Formally, if $(t_0, x(t_0), y(t_0)) \in S$, then the integral curve $(t, x(t, \varepsilon), y(t, \varepsilon))$ lies entirely on S. The only slow integral manifolds of system (1), (2) discussed here are those of dimension m (the dimension of the slow variable x) that can be represented as graphs of vector-valued functions $y = h(x, t, \varepsilon)$. Moreover, we consider here the attractive integral manifolds, only. It is important that any trajectory of (1), (2) can be represented as a trajectory on the

attractive slow integral manifold plus an asymptotically negligible terms. The flow on the slow integral manifold is described by the equation

$$\dot{x} = f(t, x, h(t, x, \varepsilon), \varepsilon). \tag{5}$$

2.1 Asymptotic Expansions

When the method of integral manifolds is being used to solve a specific problem, then a central question is the calculation of the function $h(x, t, \varepsilon)$ in terms of the manifold described. An exact calculation is generally impossible, and various approximations are necessary. One possibility is the asymptotic expansion of $h(x, t, \varepsilon)$ in integer powers of the small parameter

$$h(t, x, \varepsilon) = h_0(t, x) + \varepsilon h_1(t, x) + \cdots + \varepsilon^k h_k(t, x) + \cdots \tag{6}$$

Substituting this formal expansion into the invariance equation

$$\varepsilon \frac{\partial h(t, x, \varepsilon)}{\partial t} + \varepsilon \frac{\partial h(t, x, \varepsilon)}{\partial x} f(t, x, h(t, x, \varepsilon), \varepsilon) = g(t, x, h(t, x, \varepsilon), \varepsilon), \tag{7}$$

we obtain the relationship

$$\varepsilon \sum_{k\geq 0} \varepsilon^k \frac{\partial h_k}{\partial t} + \varepsilon \sum_{k\geq 0} \varepsilon^k \frac{\partial h_k}{\partial t} f(t, x, \sum_{k\geq 0} \varepsilon^k h_k, \varepsilon) = g(t, x, \sum_{k\geq 0} \varepsilon^k h_k, \varepsilon). \tag{8}$$

We use the formal asymptotic representations

$$f(t, x, \sum_{k\geq 0} \varepsilon^k h_k, \varepsilon) = \sum_{k\geq 0} \varepsilon^k f^{(k)}(t, x, h_0, \ldots, h_k), \tag{9}$$

$$g(t, x, \sum_{k\geq 0} \varepsilon^k h_k, \varepsilon) = B(t, x) \sum_{k\geq 1} \varepsilon^k h_k + \sum_{k\geq 1} \varepsilon^k g^{(k)}(t, x, h_0, \ldots, h_{k-1}), \tag{10}$$

where the matrix $g_y(t, x, h_0(t, x), 0) = B(t, x)$, and $g(t, x, h_0(t, x), 0) = 0$.

Substituting these formal expansions into the invariance equation

$$\begin{aligned}
&\varepsilon \frac{\partial \phi}{\partial t} + \varepsilon^2 \frac{\partial h_1}{\partial t} + \cdots + \varepsilon^k \frac{\partial h_{k-1}}{\partial t} + \cdots \\
&\quad + \left(\varepsilon \frac{\partial \phi}{\partial x} + \varepsilon^2 \frac{\partial h_1}{\partial x} + \cdots + \varepsilon^k \frac{\partial h_{k-1}}{\partial x} + \cdots \right) (f_0(x, \phi, t) + \varepsilon f_1(x, \phi, h_1, t) + \cdots \\
&\quad + \varepsilon^k f_k(x, \phi, \ldots, h_k, t) + \cdots) = B(x, t)(\varepsilon h_1 + \varepsilon^2 h_2 + \cdots + \varepsilon^k h_k) + \cdots \\
&\quad + \varepsilon g_1(x, \phi, t) + \varepsilon^2 g_2(x, \phi, h_1, t) + \cdots + \varepsilon^k g_k(x, \phi, \ldots, h_{k-1}, t) + \cdots,
\end{aligned}$$

and equating powers of ε, we obtain

$$\frac{\partial \phi}{\partial t} + \frac{\partial \phi}{\partial x} f_0(x, \phi, t) = Bh_1 + g_1,$$

$$\frac{\partial h_1}{\partial t} + \frac{\partial \phi}{\partial x} f_1 + \frac{\partial h_1}{\partial x} f_0 = Bh_2 + g_2, \ldots$$

$$\frac{\partial h_{k-1}}{\partial t} + \sum_{0 \le p \le k-1} \frac{\partial h_p}{\partial x} f_{k-1-p} = Bh_k + g_k, \quad k = 2, 3, \ldots,$$

and then

$$h_1 = B^{-1} \left[\frac{\partial \phi}{\partial t} + \frac{\partial \phi}{\partial x} f_0(x, \phi, t) - g_1 \right], \tag{11}$$

$$h_2 = B^{-1} \left[\frac{\partial h_1}{\partial t} + \frac{\partial \phi}{\partial x} f_1 + \frac{\partial h_1}{\partial x} f_0 - g_2 \right]. \tag{12}$$

In general

$$h_k = B^{-1} \left[\frac{\partial h_{k-1}}{\partial t} + \sum_{0 \le p \le k-1} \frac{\partial h_p}{\partial x} f_{k-1-p} - g_k \right], \quad k = 2, 3, \ldots \tag{13}$$

We recall that $\phi(x, t)$ is determined by $g(x, \phi(x, t), t, 0) = 0$. Now we can calculate an approximation to $h(x, t, \varepsilon)$. Asymptotic expansions of slow integral manifolds were first used in [3]. A a more detailed description of the method can be found in the book [1].

3 Bacteriophages Interaction Model

Consider the model of host-microparasite interaction with a free-living infective stage of a parasite [2]

$$\begin{aligned} \dot{x} &= ax - bx(x + y) - \alpha x v, \\ \dot{y} &= \alpha x v - dy, \\ \dot{v} &= \sigma y - mv. \end{aligned} \tag{14}$$

The system can have a positive equilibrium state E^* with coordinates

$$x^* = md/\alpha\sigma, \quad y^* = \frac{am}{\alpha\sigma} \frac{R_0 - 1}{R_0 + a/d}, \quad v^* = \sigma y^*/m.$$

The condition $R_0 > 1$ is necessary and sufficient for the existence of this equilibrium state. We assume $R_0 > 1$ and, hence there is a unique positive equilibrium state E^*.

The limiting system is

$$\begin{aligned} \dot{x} &= ax - bx(x+y) - \alpha xv, \\ \dot{y} &= \alpha xv - dy, \\ 0 &= \sigma y - mv, \end{aligned} \tag{15}$$

or

$$\begin{aligned} \dot{x} &= ax - bx(x+y) - \alpha x\sigma y/m, \\ \dot{y} &= \alpha x\sigma y/m - dy. \end{aligned} \tag{16}$$

The last system can have a positive equilibrium state $\bar{E}^*$ with coordinates

$$x^* = md/\alpha\sigma, \quad y^* = \frac{am}{\alpha\sigma}\frac{R_0 - 1}{R_0 + a/d}.$$

This equilibrium state $\bar{E}^*$ is asymptotically stable whereas the corresponding equilibrium state E^* of the full system is unstable! Moreover, the full system possesses the limit cycle [2].

This apparent contradiction is easily removed if instead of the limiting system we consider the first-order approximation of the system on the integral manifold $v = \sigma y/m - \varepsilon\sigma(\sigma\beta x/m - d)y/m^2$:

$$\begin{aligned} \dot{x} &= ax - bx(x+y) - \frac{\alpha x\sigma y}{m} + \varepsilon\frac{\beta x\sigma}{m^2}\Big(\frac{\sigma\beta x}{m} - d\Big)y, \\ \dot{y} &= \Big(\frac{\alpha x\sigma y}{m} - dy\Big)\Big(1 - \varepsilon\frac{\beta x\sigma}{m^2}\Big). \end{aligned} \tag{17}$$

This system possesses the periodic solution!

References

1. R.E. O'Malley, A. Pokrovskii, V.A. Sobolev (eds)., *Singular Perturbation and Hysteresis* (SIAM, Philadelphia, 2005)
2. V. Sobolev, A. Korobeinikov, The phenomenon of apparent disappearance in the marine bacteriophages dynamics, in *Extended Abstracts Spring 2013*, ed. by Á. Corral, A. Deluca, F. Font-Clos, P. Guerrero, A. Korobeinikov, F. Massucci (Springer, New York, 2014)
3. V.V. Strygin, V.A. Sobolev, Effect of geometric and kinetic parameters and energy dissipation on orientation stability of satellites with double spin. Cosm. Res. **14**(3), 331–335 (1976)
4. K.V. Zadiraka, On a non-local integral manifold of a singularly perturbed differential system. Ukrain. Mat. Ž. **17**(1), 47–63 (1965). Translated in AMS Trans. Ser. **2**(89), 29–49 (1970)

Viruses and Their Role in the Ocean: Bacteriophages and Bacteria Interactions

Dolors Vaqué, Elisabet Laia Sà, Elena Lara, and Silvia G. Acinas

1 Introduction

Aquatic microorganisms are responsible for a variety of biogeochemical cycles that fuel our planet [5, 6]. In particular, viruses that could infect all marine organisms (from bacteria to whales) play a key role in marine systems [7]. Virus are the most abundant biological particles, ca. 10^7 ml^{-1} in surface waters Suttle 2007 and a large proportion are bacteriophages which together with protists are the main source of microbial mortality (viral shunt) returning dissolved nutrients and organic matter from lysed bacteria to the water column [3, 14] and contributing to the recycling production of the systems; see Fig. 1. Viruses are mostly considered as killers, releasing from 20 to 300 virus particles per host-cell [2,17]. However they can insert part of their genome in the chromosome of the prokaryotic host or in the chloroplast, mitochondrial or nuclear genetic systems in the eukaryotic algae host.

The inserted viral genome conforms the lysogenic temperate virus (prophage [9]) that is maintained silent, until an environmental factor triggers the temperate virus to become lytic (a process termed induction) which introduce changes in the virus infection life-strategy and implications in the biogeochemical cycles in the Ocean. Thus, virus acts as manipulating the microbial metabolism, and are the highest reservoir of genetic diversity (horizontal gene transfer) of the Oceans [4, 11]. Each infection has the potential to introduce new genetic information into an organism or progeny virus, thereby driving the evolution of both host and viral assemblages [11]. The most common phages in the Ocean are double stranded DNA and belongs to the families of Podoviridae, with short and no contractile tail, Myoviridae with long and contractile tail, and Siphoviridae with curled and no contractile tail; see

D. Vaqué (✉) • E.L. Sà • E. Lara • S.G. Acinas
Institut de Ciències del Mar (CSIC), Barcelona, Catalonia, Spain
e-mail: dolors@icm.csic.es

Á. Corral et al. (eds.), *Extended Abstracts Spring 2013*, Trends in Mathematics 2,
DOI 10.1007/978-3-319-08138-0_23

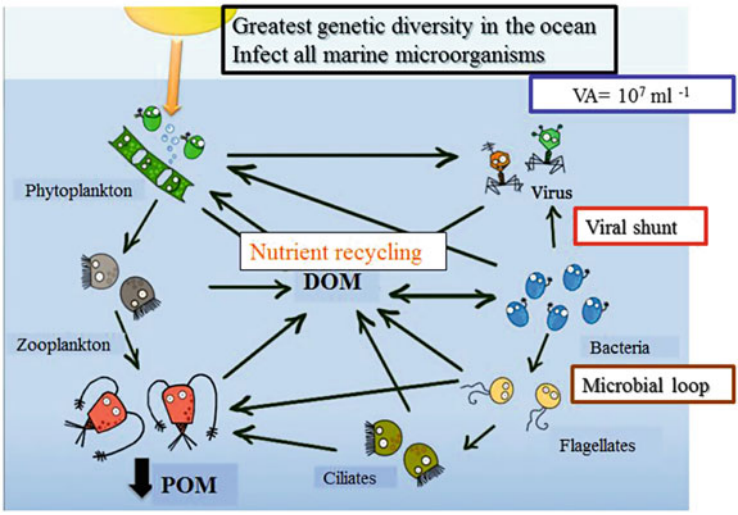

Fig. 1 Diagram showing the importance of virus as key players in the marine food-web (Drawing by Clara Ruiz-González)

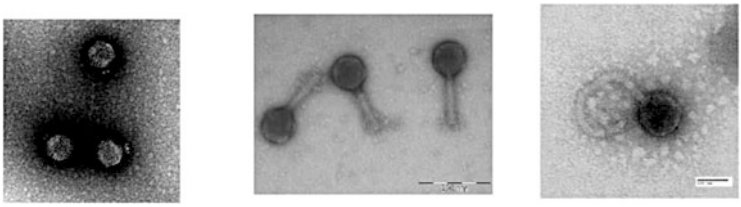

Fig. 2 Families of bacteriophages. *Left*: Podoviridae (Picture by S. Casjens and E. Lenk, reproduced with permission of the American Society for Microbiology). *Middle*: Myoviridae (Picture by E. Lara). *Right*: Siphoviridae (Picture by E. Lara)

Fig. 2. However, there are more and more evidences showing the presence of RNA bacteriophages in the water column [10].

2 Marine Bacteriophages Dynamics

Bacteriophages disappear from the water and lose their infectivity due to its adsorption to particles produce at the same time the disappearance of virus (and perhaps losses of infectivity, because cannot find a host) the UV radiation suppose losses of infectivity due to damage in the genetic material, without producing any morphological change of the virions under the microscope. However, some virus can be re-activated,restoring their DNA using the machinery of the host cell [15]. Other processes like the ingestion of viruses by nano-flagellates are not

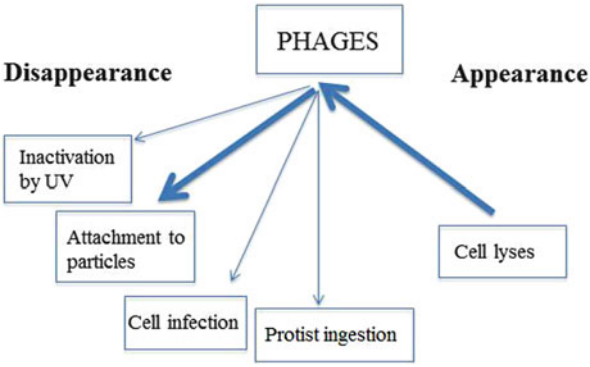

Fig. 3 Diagram showing the disappearance or inactivation and appearance of phages in aquatic systems, and the importance of each one of them according to Suttle and Chen (1992)

really quantitatively important as a loss factor [1]. Finally, once viruses get the cell-host, after replication the rate of phage appearance is quite similar to their disappearance; see Fig. 3. Then, the abundances of total phages in the ocean remain quite stable [12].

3 Host-Phage Interactions

Virus infection on bacteria seems to be favored by host density and it is assume that they are host specific. Thus the "Kill the Winner" hypothesis [13, 16] predicts that the most abundant and active bacterial population is controlled by phage lyses, which would allow the co-existence of less competitive populations and even sustain bacterial diversity. But, it is not clear if this hypothesis is relevant for natural and complex systems.

Further, this view assumes that virus-host relationship is specific but some studies showed that marine phages could have broad host ranges [8]. In our lab we have isolated 18 phages infecting 7 highly similar strains of Pseudoalteromonas spp., which allowed us to increase the knowledge of the richness of the Pseudoalteromonas spp. phages characterizing them and comparing the whole-genome fingerprint with host range richness within an ecological context. The host range analysis also let us to address a better understanding of the microdiversity within specific phylogenetic groups of marine bacteria. Our results demonstrate a high diversity of bacteriophage infecting phylogenetically identical bacteria based in the 16S rRNA and variability in the specificity of infection. Understanding the dynamics of phages in natural environment is crucial to predict the impact on bacterial dynamics and diversity in microbial communities.

References

1. Y. Bettarel, T. Sime-Ngando, M. Bouvy, R. Arfi, C. Amblard, Low consumption of virus-sized particles by heterotrophic nanoflagellates in two lakes of the French Massif Central. AQuat. Microb. Ecol. **39**, 205–209 (2005)
2. J.A. Boras, M.M. Sala, F. Baltar, J. Aristegui, C.M. Duarte, D. Vaqué, Effect of viruses and protists on bacteria in eddies of the canary current region (subtropical northeast Atlantic). Limnol. Oceanogr. **55**, 885–898 (2010)
3. J.A. Boras, M.M. Sala, E. Vázquez-Domínguez, M.G. Weinbauer, D. Vaqué, Annual changes of bacterial mortality due to viruses and protists in an oligotrophic coastal environment (NW Mediterranean). Environ. Microbiol. **11**, 1181–1193 (2009)
4. M. Breitbart, L.R. Thompson, C.S. Suttle, M.B. Sullivan, Exploring the vast diversity of marine viruses. Oceanography **20**, 353–362 (2007)
5. C.P.D. Brussaard, S.W. Wilhelm, F. Thingstad, M.G. Weinbauer, G. Bratbak, M. Heldal, S.A. Kimmance, M. Middelboe, K. Nagasaki, J.H. Paul, D.C. Schroeder, C.A. Suttle, D. Vaqué, K. E. Wommack, Global-scale processes with a nanoscale drive: the role of marine viruses. ISME J. **2**, 575–578 (2008)
6. P.G. Falkowski, T. Fenchel, E.F. Delong, The microbial engines that drive earth's biogeochemical cycles. Science **320**(5879), 1034–1039 (2008)
7. J.A. Fuhrman, Marine viruses and their biogeochemical and ecological effects. Nature **399**, 541–548 (1999)
8. K. Holmfeldt, M. Middelboe, O. Nybroe, L. Riemann, Large variabilities in host strain susceptibility and phage host range govern interactions between lytic marine phages and their Flavobacterium hosts. Appl. Environ. Microb. **73**, 6730–6739 (2007)
9. S.C. Jiang, J.H. Paul, Significance of lysogeny in the marine environments: studies with isolates and a model for viral production. Microb. Ecol. **35**, 235–243 (1998)
10. G.F. Steward, A.I. Culley, J.A. Mueller, E.M. Wood-Charlson, M. Belcaid, G. Poisson, Are we missing half of the viruses in the Ocean? ISME J. **7**, 672–679 (2012)
11. C.A. Suttle, Marine viruses major players in the global ecosystem. Nat. Rev. Microbiol. **5**, 801–812 (2007)
12. C.A. Suttle, F. Chen, Mechanisms and rates of decay of marine viruses in seawater. Appl. Environ. Microbiol. **58**, 3721–3729 (1992)
13. T.F. Thingstad, R. Lignell, Theoretical models for the control of bacterial growth rate, abundance, diversity and carbon demand. Aquat. Microb. Ecol. **13**, 19–27 (1997)
14. M.G. Weinbauer, Ecology of prokaryotic viruses. FEMS Microb. Rev. **28**, 127–181 (2004)
15. M.G. Weinbauer, S.W. Wilhelm, C.A. Suttle, R.D. Garza, Photoreactivation compensates for UV damage and restores infectivity to natural virus communities. Appl. Environ. Microbiol. **63**, 2200–2205 (1997)
16. C. Winter, T. Bouvier, M.G. Weinbauer, T.F. Thinsgtad, Trade-off between competition and defense specialists among unicellular plankton organisms: the 'killing the winner' hypothesis revisited. Microbiol. Mol. Biol. Rev. **74**, 42–57 (2000)
17. K.E. Wommack, R.R. Colwell, Virioplankton: viruses in aquatic ecosystems. Microbiol. Mol. Biol. Rev. **64**, 69–114 (2000)